This is a non-peer reviewed preprint submitted to EarthArXiv.
This manuscript was submitted to Geophysical Journal International for peer review on 12 April 2022.

Geophys. J. Int. () , 1–33

A unified numerical model for two-phase porous, mush and suspension flow dynamics in magmatic systems

Ying-Qi Wong[1] and Tobias Keller[1]
[1] *Department of Earth Sciences, ETH Zürich, Zürich, Switzerland. Email: ying.wong@erdw.ethz.ch*

12 April 2022

SUMMARY
Multi-disciplinary evidence increasingly suggests that crustal magmatic systems exist as crystal-rich mush bodies with smaller, ephemeral regions of crystal-poor magma. However, most process-based models of magmatic systems describe magma flowing as if it were a single-phase fluid, as two-phase porous flows at low melt fractions or two-phase suspension flows at high melt fraction. These existing models are not tailored to study the dynamics of mush flows at intermediate phase fractions, leaving a significant gap in bridging trans-crustal magma processing from source to surface, in particular for estimating how fast magmatic systems can assemble sufficient melt to fuel large eruptions. To address this knowledge gap and unify two-phase magma flow models, we develop a two-dimensional system-scale numerical model of the fluid mechanics of an n-phase system at all phase proportions, based on a recent theoretical model for multi-phase reactive transport. We apply this model to a two-phase, solid-liquid system using transport coefficients calibrated to theory and experiments on mixtures of olivine-rich rock and basaltic melt. Scaling analysis of the governing equations reveals an inherent length scale for phase segregation and compaction, analogous to the compaction length in porous flow models, and shows that phase segregation and mixture flow arise as complementary components of the same underlying physics. The model replicates known one-dimensional end-member phenomena in two-phase mixtures, including rank-ordered porosity wavetrains in the porous flow regime, and shock/rarefaction concentration waves in the suspension flow regime. In magma bodies confined by impermeable rock, contrasting segregation-compaction lengths at low versus high melt fractions produce asymmetrical compaction and decompaction layers at the bottom and top of the domain respectively. Two-dimensional simulations substantiate the scaling analysis: systems smaller or close to the segregation-compaction length are dominated by phase segregation, whereas much larger systems are dominated by mixture convection driven by lateral perturbations in phase proportions. In the mush regime, the large variation of segregation-compaction lengths with modest changes in phase proportion promotes fast segregation to form localised melt-rich bands on the time scale of months to years. Results demonstrate how magmatic systems progress through porous to mush to suspension flow with increasing melt accumulation and explain how crystal-rich, melt-poor systems form smaller, ephemeral, crystal-poor, melt-rich regions. Both the inherent length scale and resulting time scale of phase segregation in the mush regime are compatible with the formation of stacked sill structures in mafic systems and the efficient melt assembly for large eruptions in silicic systems.

Key words: Physics of magma and magma bodies; Magma chamber processes; Numerical modelling; Mechanics, theory, and modelling

1 INTRODUCTION

Mounting evidence suggests that large trans-crustal magmatic systems spend most of their lifetimes as crystal-rich mush bodies from which smaller batches of crystal-poor magma can emerge and source eruptions (Cashman & Giordano, 2014; Edmonds et al., 2019, and references therein). In the volcanic record, observations of both crystal-rich and crystal-poor erupted material reflect the textural variability expected in the subsurface system (Lipman et al., 1997; Brown et al., 1998; Hildreth & Fierstein, 2000; Schmitt et al., 2003). As crystals pass through different pressure-temperature or even compositional regions, they grow with slightly altered chemistry and at different rates to form crystal zoning. These crystal zoning patterns often imply extended storage at near-solidus conditions, and sometimes record an influx of hot, crystal-poor magma shortly before eruption (Bachmann et al., 2002; Cooper & Kent, 2014; Wolff et al., 2015). Among crystals from the same magmatic system, the diversity of pre-eruptive

storage conditions suggests that crystals grew in chemically distinct melts, which requires melt-rich regions to remain isolated until shortly before eruption, assembling on times scales of years to decades (Berlo et al., 2007; Smith et al., 2009; Druitt et al., 2012; Cashman & Blundy, 2013; Kilgour et al., 2013; Wotzlaw et al., 2015). This precludes a single melt-rich magma body that can mix easily (Cashman et al., 2017). Furthermore, geophysical observations from seismic tomography and magnetotelluric surveys have yet to find extensive melt-rich zones under volcanoes. Typical estimates of melt fraction span $10 - 40\%$ (e.g., Chu et al., 2010; Paulatto et al., 2019; Bai et al., 2020; Cordell et al., 2020), where these values represent averages over a large volume in the crust. Taken together, these observations suggest that melt-rich zones in magmatic systems are spatially limited, ephemeral features situated within larger, longer-lived, crystal-rich mush bodies.

Magmas are multi-phase mixtures containing solid crystals, liquid melt and exsolved gases of different chemical compositions. Volatiles may be dissolved in the silicate melt phase or exist as a separate, compressible, low-viscosity, supercritical fluid to gas phase, depending on pressure and temperature. Anticipating contrasting physical processes for melt-poor and melt-rich systems, magmas are often classified into partially molten rock at low melt fractions and magmatic suspensions at high melt fractions, while crystal-rich to melt-rich mushes exist at intermediate melt fractions (e.g., Sparks et al., 2019). A magma body with low to intermediate melt fractions will be too viscous to erupt as a whole from the crust. For eruptions to occur, enough of the lower viscosity melt phase has to accumulate to mobilise the magma and eventually break through overlying wall rock and ascend rapidly to erupt at the surface (Bachmann & Bergantz, 2008; Sparks et al., 2019). Estimates of the melt extraction rate from mush systems obtained by extrapolating from existing porous flow models to the mush regime are typically too slow to match timing constraints from petrology, raising the question of how crustal magmatic systems can assemble sufficient melt within geologically short times to fuel large eruptions (Bachmann & Bergantz, 2004; Bachmann & Huber, 2019).

To determine the mechanics and time scales of processes involved in trans-crustal magma systems from source to surface, we require a unified model framework that spans the phase proportions from partially molten rock at low melt fractions to magmatic suspensions at high melt fractions. However, existing models for flow in a magmatic system are generally limited to single-phase flow or endmember porous and suspension flow regimes in two-phase, solid-liquid systems. Single-phase flow models assume that magma moves as a homogeneous fluid, implying that phase segregation is negligible and that collective flow of the mixture dominates the dynamics. Multiple phases have been included in such models to track the spatial and temporal variations in phase fraction and their associated material properties (e.g. density, viscosity), but no differential motion between phases is accounted for. These models have been used to study the role of phase changes such as crystallisation or volatile exsolution in driving convection (e.g. Brandeis & Jaupart, 1986; Longo et al., 2006), the time taken to trigger eruptions following mafic magma recharge into a silicic reservoir (Snyder, 2000), as well as the efficiency of convective mixing in homogenizing magma reservoirs on the system scale (Huber et al., 2009).

To model the differential transport of phases relative to one another, the velocity field of each phase must be resolved. Numerous studies have developed theories for two-phase, solid-liquid flow limited to either solid-rich or liquid-rich endmember regimes. Models of two-phase flow in the solid-rich regime are largely based on the porous flow and compaction model of McKenzie (1984), which was developed for melt extraction at low liquid fractions ($\sim 0.1 - 10\%$) in the mantle. In this model, the ascent of the buoyant liquid phase by pervasive porous flow is accommodated by viscous compaction of the denser, stiffer, but permeable rock matrix. The compaction model is only valid up to the disaggregation threshold of the matrix, where solid grains start losing contact with one another and can no longer transmit substantial stresses (Rudge, 2018). Compaction occurs on a characteristic length scale called the compaction length, which depends on the matrix permeability and the shear viscosities of the matrix and pore liquid. For typical mantle conditions, the compaction length is on the order of hundreds of meters to kilometers (Katz, 2022). Information about liquid-rich perturbations can propagate faster than the liquid velocity during compaction (Spiegelman, 1993a). Under specific material conditions, these perturbations may evolve as solitary waves, which are shape-preserving waves that travel at a constant speed proportional to their amplitude (Scott & Stevenson, 1984; Barcilon & Richter, 1986; Stevenson & Scott, 1991). Liquid-rich instabilities or melt bands may develop if the matrix is strongly weakened by the presence of liquid, and the orientation of these localised bands can be controlled by the stress orientation in the matrix or a shear-weakening matrix rheology (Stevenson, 1989; Holtzman et al., 2003; Katz et al., 2006). If the thermodynamics of phase-change is included, some reactions can enhance matrix permeability and form reactive melt channels by the reactive infiltration instability (Aharonov et al., 1995; Kelemen et al., 1995; Spiegelman et al., 2001; Rudge et al., 2011; Weatherley & Katz, 2012; Keller & Katz, 2016; Rees Jones et al., 2018). Porous flow from compacting partially molten rock or crystal-rich mush is likely too inefficient to produce sufficient amounts of eruptible melt in the upper crust (Bachmann & Bergantz, 2004; Bachmann & Huber, 2019). Nevertheless, microstructural evidence from grain orientation and deformation in cumulates have sometimes (Philpotts & Philpotts, 2005; Zieg & Marsh, 2012; Bertolett et al., 2019) but not always (Holness et al., 2017) indicated viscous compaction as an important process.

In the liquid-rich endmember regime, magma is modelled as a particulate suspension. Solid particles (silicate crystals) settle out of the liquid phase by Stokes settling (e.g. Sparks et al., 1984; Martin & Nokes, 1988; Dufek & Bachmann, 2010). The particle settling speed is thought to be proportional to the density contrast between the phases and the square of the particle size, but inversely proportional to the liquid viscosity. As the solid fraction increases, the settling speed decreases due to more pronounced backflow, potentially producing correlated particle settling (Zahn et al., 1997; Mucha et al., 2004) and particle concentration waves (Manga, 1996; Drew & Passman, 1999) on length scales much larger than an individual crystal. In low-Reynolds number suspensions, particle-driven convection tends to be substantially faster than the settling speed of individual particles (Martin & Nokes, 1988; Culha et al., 2020). Even so, typical settling rates in magmatic systems are too slow to generate large melt-rich magma volumes (Bachmann & Bergantz, 2004; Bachmann & Huber, 2019). The suspension flow approximation fails when the particle density becomes too high, as particles collide and become packed together.

A few studies have investigated the dynamics at intermediate phase fractions by extending either the porous flow model beyond the disaggregation threshold ($\sim 20 - 40\%$ liquid fraction) or the Stokes settling model beyond the close packing limit ($\sim 30 - 60\%$ liquid fraction). Bercovici et al. (2001) derived phase-symmetrical equations including surface tension terms valid for general two-phase, solid-liquid systems but limited their analysis to the solid-rich regime, essentially recovering the compaction model. To ex-

plain compositional gaps in volcanic products, Dufek & Bachmann (2010) applied the Navier-Stokes equation with a drag term to simulate hindered settling of crystals below the close packing limit and Darcy flow of melt above the packing limit, although the latter does not appear to contribute significantly to the model outcome. However, it is not clear if these extensions are valid on the interval between the disagreggation and close packing limits, where we expect crustal magma mush bodies to lie. More recently, Keller & Suckale (2019) and Oliveira et al. (2018) derived conservation equations for multi-phase, multi-component reactive transport using the volume and ensemble averaging methods respectively. Keller & Suckale (2019) further derived effective transport coefficients as emerging consistently from the pure-phase properties, phase fractions and assumptions regarding the connectivity of microscopic phase constituents in the mixture. This approach enables the transport coefficients, and consequently the model, to be theoretically well-defined as well as practically applicable across the phase space.

In this study, we apply the theory from Keller & Suckale (2019) to investigate the dynamics of two-phase flow across the porous, mush, and suspension flow regimes. The goal is to understand the mechanisms for efficient transport and, subsequently, accumulation of melt in magmatic systems. We present a MATLAB software package to numerically model the mechanical (i.e., isothermal, isochemical, non-reactive) evolution of n-phase systems. While crustal magmatic systems are mostly silicic in composition, we first apply the model calibration for a olivine-rich rock and a basaltic melt due to the greater availability of experimental constraints on these mixtures. We use the results to discuss melt accumulation rates in silicic systems most pertinent to large and hazardous volcanic eruptions. Since this model is applicable to the whole phase fraction space, we recover the well-known limits of porous liquid percolation and viscous compaction in solid-dominated mixtures, as well as Stokes settling from particulate suspensions in liquid-dominated mixtures (Sections 4.2.1, 4.2.2). Moreover, this new numerical model self-consistently extends to the mush flow regime at intermediate liquid fractions.

An important concept in this study is that an inherent length scale for phase segregation and compaction emerges from the governing equations. This length scale, called the segregation-compaction length (after Keller & Suckale, 2019), is a generalisation of the compaction length from McKenzie (1984). Depending on the ratio of this inherent length scale to the characteristic size of the modelled system, the mixture will be dominated either by phase segregation (i.e., Darcy percolation and viscous compaction, Stokes settling) or by collective mixture flow of both phases. Thus, phase segregation and mixture flow emerge as complementary components of the same physics. In Section 2.2, we demonstrate by scaling analysis how the segregation-compaction length emerges from the governing equations. In Section 4.1, we test the emergent characteristic speed and pressure scales against a set of idealised numerical simulations across all flow regimes. In the remainder of the study, we demonstrate the role of the segregation-compaction length in the regimes of porous, mush, and suspension flows. In one-dimensional (1D) column models with rigid and impermeable boundaries, phase segregation produces asymmetric boundary layers (Section 4.2.3): the less dense liquid forms a narrow decompaction boundary layer at the top of the domain while the denser solids form a wide compaction boundary layer at the bottom. We then show how system scale relative to the segregation-compaction length affects emergent dynamics in two-dimensional (2D) models (Section 4.3). In particular, shear deformation in mushy systems can localise melt into stress-aligned melt-rich shear bands. Melt segregation rates in the mush regime match well with petrologically-derived rates and are sufficient to accumulate large volumes of melt within years in mafic systems and centuries in silicic systems, potentially explaining how large-volume eruptions can be fueled by trans-crustal magmatic systems.

2 CONTINUUM MODEL

2.1 Governing equations

The model applies the mechanical equations (no thermo-chemical evolution, no reactions) from the framework of Keller & Suckale (2019), where a detailed derivation can be found. Here we present a condensed summary of the governing equations. The model describes a system containing n material phases, with each phase $i = 1, ..., n$ represented by its continuum-scale phase volume fraction ϕ^i, pressure P^i and velocity $\mathbf{v}^i$ (all variables and parameters vary in space and time, unless noted otherwise). The mechanical evolution of the system is described by the conservation of mass and momentum for each phase i,

$$\frac{1}{\rho^i}\frac{D^i_\phi \rho^i}{Dt} = -\nabla \cdot \mathbf{q}^i_\phi - \Gamma^i_\phi \,, \tag{1a}$$

$$\rho^i \frac{D^i_\phi \mathbf{v}^i}{Dt} = -\nabla \cdot \underline{\mathbf{q}}^i_v - \mathbf{\Gamma}^i_v - \mathbf{Q}^i_v \,, \tag{1b}$$

where $D^i_\phi(\cdot)/Dt$ is the material derivative that describes the change in the partial quantity of phase i per unit time in the moving reference frame of the phase volume flux,

$$\frac{D^i_\phi(\cdot)}{Dt} = \phi^i \frac{\partial(\cdot)}{\partial t} + \mathbf{q}_\phi \cdot \nabla(\cdot) \,. \tag{2}$$

Equations (1) express that the conserved quantities change in time due to the divergence of intra-phase fluxes $\mathbf{q}^i$ driven by spatial gradients of the relevant thermodynamic variables within each phase, inter-phase transfers $\mathbf{\Gamma}^i$ driven by phase deviations in thermodynamic variables, and any external sources $\mathbf{Q}^i$. By definition, transfers must sum to zero across all phases, i.e. $\sum_i \mathbf{\Gamma}^i = 0$. For mass balance (1a), the phase density ρ^i changes with time to balance volume flux $\mathbf{q}^i_\phi$ and volume transfer from other phases $\Gamma^i_\phi \equiv \partial\phi^i/\partial t$. We assume that the aggregate is saturated: any decrease in the phase fraction ϕ^i within a control volume must be compensated by an increase in other phase fractions such that $\sum_i \phi^i = 1$ holds. There are no external sources of mass. Momentum balance (1b) takes a similar form to mass balance. Changes in $\mathbf{v}^i$ result from momentum flux $\underline{\mathbf{q}}^i_v$, momentum transfer from other phases $\mathbf{\Gamma}^i_v$ and an external source $\mathbf{Q}^i_v$ of momentum.

The time derivatives for ρ^i and $\mathbf{v}^i$ are included in (1) for generality; however, for the remainder of this study they will be neglected. We approximate the phase materials to be incompressible ($D^i_\phi \rho^i/Dt \approx 0$). Since typical magma viscosities are high, Reynolds numbers in magmatic systems are usually much less than unity, rendering the inertial term in the momentum balance equation negligible ($D^i_\phi \mathbf{v}^i/Dt \approx 0$). These assumptions reduce the governing equations to their steady-state form, where volume fluxes balance volume transfers, while momentum fluxes balance momentum transfers and the momentum source, which is the gravitational body force. Only through the time-dependence of phase fractions $\Gamma^i_\phi \equiv \partial\phi^i/\partial t$ does the solution evolve with time.

Keller & Suckale (2019) derived constitutive relations to describe the fluxes and transfers based on the thermodynamic constraints of energy conservation and non-negative entropy produc-

tion, and sources based on external knowledge of the model environment. Additional conditions such as frame-invariance and isotropic material response constrained the choice of constitutive relations. We state these constitutive relations in Appendix A1 and refer the reader to Keller & Suckale (2019) for the detailed derivation, but we highlight a few key concepts here for clarity. First, the fluxes and transfers are controlled by phenomenological material response coefficients (K^i_ϕ, K^i_v for fluxes, C^i_ϕ, C^i_v for transfers) which depend on the diffusive properties of pure-phase materials weighted by their phase fraction and phase connectivity within the mixture. This framework of coefficient closures is one of the novel aspects of the model, because it relates effective transport properties to a common phenomenological description of how the phases are organised in the mixture at the local scale of microscopic phase constituents such as crystals and liquid films (Appendix A2).

Second, the model framework introduces a reference pressure P^* and reference velocity $\mathbf{v}^*$. The reference pressure is obtained from the average of phase pressures weighted by the volume transfer coefficients C^i_ϕ. The reference velocity is obtained from the average of velocities weighted by the momentum transfer coefficients C^i_v. The reference fields can be conceived as the target for mechanical phase equilibration by transfers in the mixture, given a particular configuration of phase fields and their coefficients. The phase that is most abundant and has the highest transport coefficient (i.e., equilibrates the fastest) dominates the reference field. The other phases equilibrate towards this reference field, albeit at slower rates. Deviation of each phase field from the reference field, indicated by the notation $\Delta P^{i*} = P^i - P^*$, $\Delta \mathbf{v}^{i*} = \mathbf{v}^i - \mathbf{v}^*$, drive transfers between phases, such that these phase deviations represent the mechanical disequilibrium between the phases in the mixture.

Substituting the flux, transfer and source constitutive relations into (1), we obtain the governing equations as

$$\nabla \cdot [-K^i_\phi \Delta(\nabla P)^{i*} + \phi^i \mathbf{v}^i] + [C^i_\phi \Delta P^{i*} - \mathbf{v}^* \cdot \nabla \phi^i] = 0 \,, \tag{3a}$$

$$\nabla \cdot [-K^i_v \underline{\mathbf{D}}^i + \phi^i P^i \underline{\mathbf{I}}] + [C^i_v \Delta \mathbf{v}^{i*} - P^* \nabla \phi^i] - \phi^i \rho^i \mathbf{g} = 0 \,, \tag{3b}$$

where $\underline{\mathbf{D}}^i$ is the deviatoric part of the symmetrical velocity gradient tensor (i.e., the deviatoric strain rate), $\underline{\mathbf{I}}$ is the identity matrix, and $\mathbf{g}$ is the gravitational acceleration. Alongside the governing equations, we have an additional equation that relates the volume transfer to the time evolution of phase fractions,

$$\Gamma^i_\phi \equiv \frac{\partial \phi^i}{\partial t} = C^i_\phi \Delta P^{i*} - \mathbf{v}^* \cdot \nabla \phi^i \,. \tag{4}$$

2.2 Inherent scales in the governing equations

To identify natural scales of velocity and pressure, we perform a scaling analysis on the governing equations (3). We first rearrange (3) to express phase-wise mass and momentum balance in terms of compaction pressure P^i_Δ and segregation velocity $\mathbf{v}^i_\Delta$,

$$\begin{aligned} P^i_\Delta &= \phi^i (P^i - P^*) \\ &= -\frac{{\phi^i}^2}{C^i_\phi} \left[\nabla \cdot \mathbf{v}^* + \frac{1}{\phi^i} \nabla \cdot \mathbf{v}^i_\Delta - \frac{1}{\phi^i} \nabla \cdot K^i_\phi \Delta(\nabla P)^{i*} \right] \,, \end{aligned} \tag{5a}$$

$$\begin{aligned} \mathbf{v}^i_\Delta &= \phi^i (\mathbf{v}^i - \mathbf{v}^*) \\ &= -\frac{{\phi^i}^2}{C^i_v} \left[\nabla p^* + \frac{1}{\phi^i} \nabla P^i_\Delta - \frac{1}{\phi^i} \nabla \cdot K^i_v \underline{\mathbf{D}}^i - \Delta \rho^i \mathbf{g} \right] \,. \end{aligned} \tag{5b}$$

In each equation, we have separated terms arising from the reference fields (with asterisk superscripts) and from the phase segregation fields (with Δ subscripts). The compaction pressure P^i_Δ depends on the divergences of the reference and segregation velocity fields, as well as the divergence of deviations in phase pressure gradient $\Delta(\nabla P)^{i*} = (\nabla P)^i - (\nabla P)^*$, which drives the diffusion of phase volume fractions. The segregation velocity $\mathbf{v}^i_\Delta$ depends on the gradients of reference and compaction pressure, the divergence of deviatoric stress, and the buoyancy force. We have reduced the full pressure gradient ∇P^* to its dynamic part $\nabla p^* = \nabla P^* - \langle \bar{\rho} \rangle g$ by removing the mean lithostatic pressure gradient, where $\langle \bar{\rho} \rangle$ is the spatial average of the mixture density $\bar{\rho} = \sum_i \phi^i \rho^i$ over the model domain and is a scalar. Segregation is then driven by phase density contrasts, $\Delta \rho^i = \rho^i - \langle \bar{\rho} \rangle$.

Mixture flow dynamics of the two-phase mixture can be described by summing (5) over all the phases, which reduce to the governing equations for single-phase flow,

$$\nabla \cdot \bar{\mathbf{v}} = \nabla \cdot \mathbf{v}^* + \sum_i \nabla \cdot \mathbf{v}^i_\Delta = 0 \,, \tag{6a}$$

$$\nabla \bar{p} = \nabla p^* + \sum_i \nabla P^i_\Delta = \nabla \cdot \bar{K}_v \bar{\mathbf{D}} + \Delta \bar{\rho} \mathbf{g} \,, \tag{6b}$$

where $\bar{\mathbf{v}} = \sum_i \phi^i \mathbf{v}^i$ is the mixture velocity and $\bar{p} = \sum_i \phi^i p^i$ is the mixture pressure, again reduced by the mean lithostatic pressure gradient. Phase fraction perturbations give rise to variations in mixture density across the domain, hence the buoyancy force driving mixture flow is proportional to $\Delta \bar{\rho} = \sum_i \phi^i \Delta \rho^i = \bar{\rho} - \langle \bar{\rho} \rangle$. For the momentum diffusion term in (6b) we have assumed that $\sum_i K^i_v \underline{\mathbf{D}}^i \approx \bar{K}_v \bar{\mathbf{D}}$, where $\bar{K}_v = \sum_i K^i_v$ is the mixture momentum flux coefficient, and $\bar{\mathbf{D}}$ the deviatoric strain rate tensor calculated using the mixture velocity, $\bar{\mathbf{v}}$, which is reasonable if assuming that one phase is much stiffer and dominates the mixture velocity, as discussed in the next paragraph.

To compare the relative contributions of phase segregation and compaction, as well as mixture flow, to overall flow dynamics, we derive the characteristic scales of segregation velocity $\mathbf{v}^i_\Delta$ and mixture velocity $\bar{\mathbf{v}}$, as well as of compaction pressure P^i_Δ and mixture pressure $\bar{p}$. We first substitute (6) into (5) to replace the reference fields $\mathbf{v}^*, p^*$ with the mixture fields $\bar{\mathbf{v}}, \bar{p}$. We consider the dynamics in a two-phase system where one phase has a much higher mobility for segregation (denoted $i = j$, i.e. liquid phase in solid-liquid mixture), while the other phase has a much higher resistance to compaction (denoted $i = k$, i.e. solid phase). In such systems, phase j is the most compliant while phase k is the most competent ($K^j_v \ll K^k_v$), causing phase j to dominate the reference pressure such that $P^j_\Delta \approx 0$, while causing phase k to dominate the reference velocity such that $\mathbf{v}^k_\Delta \approx 0$. These considerations allow us to drop $P^j_\Delta, \mathbf{v}^k_\Delta$ from the following equations. Further neglecting diffusion terms assuming K^k_ϕ, K^j_v are small, we obtain

$$P^k_\Delta = -\frac{{\phi^k}^2}{C^k_\phi} \left[\nabla \cdot \bar{\mathbf{v}} - \nabla \cdot \mathbf{v}^j_\Delta \right] \,, \tag{7a}$$

$$\mathbf{v}^j_\Delta = -\frac{{\phi^j}^2}{C^j_v} \left[\nabla \bar{p} - \nabla P^k_\Delta - \Delta \rho^j \mathbf{g} \right] \,. \tag{7b}$$

We have preserved the divergence of the mixture velocity in (7a) to highlight the symmetry in the equations, however this term is equal to zero for incompressible pure phase materials to conserve mixture mass (6a). The resulting equations explicitly demonstrate that the segregation velocity of phase j is complemented by the compaction pressure of phase k. Performing the same substitution for the phase

fraction evolution (4) and replacing the compaction pressure term using (7a), we write,

$$\frac{\partial \phi^k}{\partial t} = -\phi^k \left[\nabla \cdot \bar{\mathbf{v}} - \nabla \cdot \mathbf{v}_\Delta^j\right] - (\bar{\mathbf{v}} - \mathbf{v}_\Delta^j) \cdot \nabla \phi^k \,. \tag{8}$$

With the equations suitably recast, we non-dimensionalise the problem by introducing characteristic physical scales for the variables, denoted with subscript 0,

$$\begin{aligned}
&\bar{\mathbf{v}} \sim \bar{u}_0, \quad \mathbf{v}_\Delta^j \sim u_0^j, \quad \bar{p} \sim \bar{p}_0, \quad p_\Delta^k \sim p_0^k, \\
&\phi^j \sim \phi_0^j, \quad \phi^k \sim \phi_0^k, \quad t \sim t_0, \quad \nabla \sim 1/\ell_0, \\
&\Delta\rho^j \sim \Delta\rho_0^j, \quad \Delta\bar{\rho} \sim \Delta\bar{\rho}_0, \quad \mathbf{g} \sim g_0, \\
&\bar{K}_v \sim \bar{K}_{v,0}, \quad C_v^j \sim C_{v,0}^j, \quad C_\phi^k \sim C_{\phi,0}^k \,,
\end{aligned} \tag{9}$$

such that any variable $\mathbf{a}$ can be decomposed into its characteristic scale a_0 and a dimensionless variable $\mathbf{a}'$, i.e. $\mathbf{a} = a_0\mathbf{a}'$. Substituting these scales into equations (4), (6) and (7) and dropping all primes, we obtain

$$\left[\frac{\bar{u}_0}{\ell_0}\right] \nabla \cdot \bar{\mathbf{v}} = 0 \,, \tag{10a}$$

$$\left[\frac{\bar{p}_0}{\Delta\bar{\rho}_0 g_0 \ell_0}\right] \nabla \bar{p} = \left[\frac{\bar{K}_{v,0}\bar{u}_0}{\Delta\bar{\rho}_0 g_0 \ell_0^2}\right] \nabla \cdot \bar{K}_v \bar{\mathbf{D}} + \Delta\bar{\rho}\hat{\mathbf{z}} \,, \tag{10b}$$

$$\left[p_0^k\right] P_\Delta^k = -\left[\frac{{\phi_0^k}^2}{C_{\phi,0}^k}\frac{u_0^j}{\ell_0}\right] \frac{{\phi^k}^2}{C_\phi^k} \left(\left[\frac{\bar{u}_0}{u_0^j}\right] \nabla \cdot \bar{\mathbf{v}} - \nabla \cdot \mathbf{v}_\Delta^j\right) \,, \tag{10c}$$

$$\begin{aligned}
\left[u_0^j\right] \mathbf{v}_\Delta^j = &-\left[\frac{{\phi_0^j}^2}{C_{v,0}^j}\Delta\rho_0^j g_0\right] \frac{{\phi^j}^2}{C_v^j} \times \\
&\left(\left[\frac{\bar{p}_0}{\Delta\rho_0^j g_0 \ell_0}\right] \nabla \bar{p} - \left[\frac{p_0^k}{\Delta\rho_0^j g_0 \ell_0}\right] \nabla P_\Delta^k - \Delta\rho^j \hat{\mathbf{z}}\right) \,,
\end{aligned} \tag{10d}$$

$$\begin{aligned}
\left[\frac{\ell_0}{u_0^j t_0}\right] \frac{\partial \phi^k}{\partial t} = &-\phi^k \left(\left[\frac{\bar{u}_0}{u_0^j}\right] \nabla \cdot \bar{\mathbf{v}} - \nabla \cdot \mathbf{v}_\Delta^j\right) \\
&- \left(\left[\frac{\bar{u}_0}{u_0^j}\right] \bar{\mathbf{v}} - \mathbf{v}_\Delta^j\right) \cdot \nabla \phi^k \,.
\end{aligned} \tag{10e}$$

In the above equations, the terms in square brackets contain the groups of dimensional scales for each term. Equation (10a) does not yield any meaningful scaling relationships. We have divided (10b) by its buoyancy scale so that the source term is of order unity. Assuming that all three terms are of similar magnitude, we identify natural scales for $\bar{p}_0, \bar{u}_0$ to cancel all scales from (10b),

$$\bar{p}_0 \equiv \Delta\bar{\rho}_0 g_0 \ell_0 \,, \tag{11a}$$

$$\bar{u}_0 \equiv \frac{\Delta\bar{\rho}_0 g_0 \ell_0^2}{\bar{K}_{v,0}} \,. \tag{11b}$$

These characteristic scales match the scales obtained from single-phase incompressible Stokes flow driven by a buoyancy force of magnitude $\Delta\bar{\rho}_0 g_0$ and resisted by the effective mixture viscosity $\bar{K}_{v,0}$.

We first skip (10c) and identify a natural speed scale for segregation in (10d) using buoyancy as the dominant term, such that u_0^j and the leading scale on the right-hand side cancel out,

$$u_0^j \equiv \frac{{\phi_0^j}^2}{C_{v,0}^j}\Delta\rho_0^j g_0. \tag{12}$$

The contribution of the mixture pressure and compaction pressure gradients in (10d) depends on the magnitude of their characteristic scales. The scale for the mixture pressure gradient forms a dimensionless group,

$$\mathrm{B} \equiv \frac{\bar{p}_0}{\Delta\rho_0^j g_0 \ell_0} = \frac{\Delta\bar{\rho}_0 g_0 \ell_0}{\Delta\rho_0^j g_0 \ell_0} = \frac{\Delta\bar{\rho}_0}{\Delta\rho_0^j} \,, \tag{13}$$

which reduces to the ratio between the buoyancy forces driving mixture flow and phase segregation. To find a suitable scale for the compaction pressure gradient term, we first recast the compaction pressure scale p_0^k as a combination of the phase density deviation, gravity and an as yet undefined length scale, following the typical expression of the compaction pressure scale in McKenzie (1984); Katz (2022),

$$p_0^k \equiv \Delta\rho_0^j g_0 \delta_0^{jk} \,. \tag{14}$$

Considering that compaction of phase k is coupled to segregation of phase j (10c), the appropriate driving density contrast here is the deviation of phase j from the mixture density, while the inherent length scale δ_0^{jk} should contain information about both phases, hence the superscript contains both phase indices. The choice of (14) reduces the scale for the compaction pressure gradient in (10d) to a ratio of length scales,

$$\mathrm{R} \equiv \frac{p_0^k}{\Delta\rho_0^j g_0 \ell_0} = \frac{\Delta\rho_0^j g_0 \delta_0^{jk}}{\Delta\rho_0^j g_0 \ell_0} = \frac{\delta_0^{jk}}{\ell_0}. \tag{15}$$

We now substitute the segregation velocity scale to the leading scale on the right-hand side of (10c) and find,

$$\frac{{\phi_0^k}^2}{C_{\phi,0}^k}\frac{u_0^j}{\ell_0} = \left(\frac{{\phi_0^k}^2}{C_{\phi,0}^k}\frac{{\phi_0^j}^2}{C_{v,0}^j}\right) \frac{\Delta\rho_0^j g_0}{\ell_0} \,. \tag{16}$$

Considering that the entire term has units of pressure, the group in parentheses on the right will have units of length squared. We identify it as the square of the inherent length scale δ_0^{jk} so that the term on the right-hand side reduces to $p_0^k \mathrm{R}$. We refer to this length scale as the segregation-compaction length (Keller & Suckale, 2019) that describes the segregation of phase j accommodated by compaction of phase k,

$$\delta_0^{jk} = \sqrt{\frac{{\phi_0^j}^2}{C_{v,0}^j}\frac{{\phi_0^k}^2}{C_{\phi,0}^k}} \,. \tag{17}$$

The segregation-compaction length generalises the compaction length emerging from two-phase porous flow and compaction models (McKenzie, 1984) by extending it to the whole range of phase fractions. Comparing the form of (5) with the equations of the compaction model, the ratio ${\phi_0^j}^2/C_{v,0}^j$ is equivalent to the matrix permeability divided by the pore liquid viscosity, while ${\phi_0^k}^2/C_{\phi,0}^k$ is equivalent to the compaction viscosity.

Applying the derived scales to the ratio of speed scales in (10c) and (10e) by substituting the segregation-compaction length yields,

$$\frac{\bar{u}_0}{u_0^j} = \frac{\Delta\bar{\rho}_0}{\Delta\rho_0^j}\frac{\ell_0^2 C_{v,0}^j}{\bar{K}_{v,0}{\phi_0^j}^2} = \frac{\Delta\bar{\rho}_0}{\Delta\rho_0^j}\frac{\ell_0^2}{{\delta_0^{jk}}^2}\frac{{\phi_0^k}^2}{C_\phi^k \bar{K}_{v,0}} = \frac{\mathrm{BH}}{\mathrm{R}^2} \,, \tag{18}$$

where H is the ratio of the compaction viscosity of the stiffer phase to the shear viscosity of the mixture,

$$\mathrm{H} = \frac{{\phi_0^k}^2}{C_\phi^k \bar{K}_{v,0}} \,. \tag{19}$$

Finally, the phase fraction evolution equation (10e) shows a characteristic time scale,

$$t_0 \equiv \frac{\ell_0}{u_0^j}\,, \tag{20}$$

which can be interpreted as the time taken for the segregating liquid to flow through a domain of length ℓ_0. With these dependent scales defined, the non-dimensional governing equations are,

$$\nabla\cdot\bar{\mathbf{v}} = 0\,, \tag{21a}$$
$$\nabla\bar{p} = \nabla\cdot\bar{K}_v\bar{\mathbf{D}} + \Delta\bar{\rho}\hat{\mathbf{z}}\,, \tag{21b}$$
$$P_\Delta^k = -\mathrm{R}\,\frac{{\phi^k}^2}{C_\phi^k}\left(\frac{\mathrm{BH}}{\mathrm{R}^2}\nabla\cdot\bar{\mathbf{v}} - \nabla\cdot\mathbf{v}_\Delta^j\right)\,, \tag{21c}$$
$$\mathbf{v}_\Delta^j = -\frac{{\phi^j}^2}{C_v^j}\left(\mathrm{B}\,\nabla\bar{p} - \mathrm{R}\,\nabla P_\Delta^k - \Delta\rho^j\hat{\mathbf{z}}\right)\,, \tag{21d}$$
$$\frac{\partial\phi^k}{\partial t} = -\phi^k\left(\frac{\mathrm{BH}}{\mathrm{R}^2}\nabla\cdot\bar{\mathbf{v}} - \nabla\cdot\mathbf{v}_\Delta^j\right) - \left(\frac{\mathrm{BH}}{\mathrm{R}^2}\bar{\mathbf{v}} - \mathbf{v}_\Delta^j\right)\cdot\nabla\phi^k\,. \tag{21e}$$

The non-dimensional governing equations show three dimensionless ratios that control the multi-phase dynamics in the model. The length scale ratio R, however, plays the dominant role. The buoyancy ratio B scales with the characteristic magnitude of phase fraction perturbations, which are generally much smaller than unity, thus $\mathrm{B} \ll 1$. This renders the mixture pressure gradient term in (22d) negligible. The compaction to shear viscosity ratio H depends on the choice of effective material closures. Previous studies on the two-phase compaction model pose the compaction viscosity as the shear viscosity divided by porosity (McKenzie, 1984; Bercovici et al., 2001), equivalent to $\mathrm{H} \sim 1/\phi_0^j$. Applying this form to the ratio of velocity scales would bring $\mathrm{BH} \sim 1$, implying that their effect would be secondary to the length scale ratio R.

Under the assumptions that $\nabla\cdot\bar{\mathbf{v}} = 0$ and $\mathrm{B} \ll 1$, the governing equations reduce to,

$$\nabla\cdot\bar{\mathbf{v}} = 0\,, \tag{22a}$$
$$\nabla\bar{p} = \nabla\cdot\bar{K}_v\bar{\mathbf{D}} + \Delta\bar{\rho}\hat{\mathbf{z}}\,, \tag{22b}$$
$$P_\Delta^k = \frac{{\phi^k}^2}{C_\phi^k}\,\mathrm{R}\,\nabla\cdot\mathbf{v}_\Delta^j\,, \tag{22c}$$
$$\mathbf{v}_\Delta^j = \frac{{\phi^j}^2}{C_v^j}\left(\mathrm{R}\,\nabla P_\Delta^k + \Delta\rho^j\hat{\mathbf{z}}\right)\,, \tag{22d}$$
$$\frac{\partial\phi^k}{\partial t} = \nabla\cdot\phi^k\mathbf{v}_\Delta^j - \frac{\mathrm{BH}}{\mathrm{R}^2}\,\bar{\mathbf{v}}\cdot\nabla\phi^k\,. \tag{22e}$$

The reduced governing equations present as two sets of equations coupled by the dependence of material coefficients on evolving phase fractions. Equations (22a)–(22b) are identical to the single-phase Stokes equations driven by phase density contrasts and resisted by an effective mixture viscosity. Together they solve for the flow of the mixture, while (22c)–(22e) together solve for the evolution of phase fractions as a result of coupled phase segregation and compaction, and advection on the mixture velocity.

The segregation-compaction length δ_0^{jk} emerges naturally from the phase fractions and transport coefficients, while the system length scale ℓ_0 is externally imposed (e.g., reservoir length, dike width, etc.). When both length scales are comparable ($\mathrm{R} \sim 1$), the compaction of phase k contributes to driving segregation of phase j, and vice versa. However, if the system length scale is much larger ($\mathrm{R} \ll 1$), compaction pressures will be negligible and phase segregation reduces to purely vertical, buoyancy-driven flow. In this limit of small R, the governing equations can be further reduced to

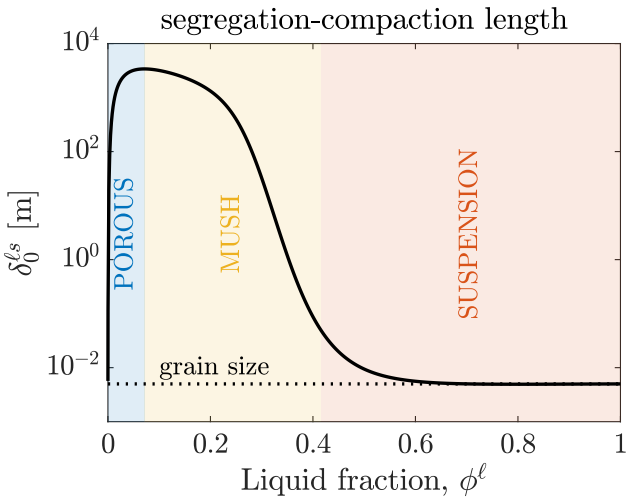

Figure 1. Segregation-compaction length $\delta_0^{\ell s}$ that describes liquid segregation and solid compaction for the calibrated two-phase system, adapted from Figure 6 of Keller & Suckale (2019).

the zero-segregation-compaction-length (ZSCL) limit,

$$\nabla\cdot\bar{\mathbf{v}} = 0\,, \tag{23a}$$
$$\nabla\bar{p} = \nabla\cdot\bar{K}_v\bar{\mathbf{D}} + \Delta\bar{\rho}\hat{\mathbf{z}}\,, \tag{23b}$$
$$\mathbf{v}_\Delta^j = \frac{{\phi^j}^2}{C_v^j}\Delta\rho^j\hat{\mathbf{z}}\,, \tag{23c}$$
$$\frac{\partial\phi^k}{\partial t} = \nabla\cdot\phi^k\mathbf{v}_\Delta^j - \frac{\mathrm{BH}}{\mathrm{R}^2}\,\bar{\mathbf{v}}\cdot\nabla\phi^k\,, \tag{23d}$$

where we have dropped terms of order R as well as the divergence of the mixture velocity which vanishes for incompressible phase materials. We note that phase fractions will evolve by advection on the mixture velocity, a term that scales as $1/\mathrm{R}^2$ (22e). On impermeable boundaries, however, the divergence of phase segregation velocities will also be significant. Hence, mechanical compaction can occur in this model but it is no longer associated with phase pressure differences or a finite inherent length scale.

Even though the analysis in this section was motivated by a two-phase problem, the scaling analysis and the definition of the segregation-compaction length apply to any pair of phases j, k within a general n-phase system as long as they exhibit a strong contrast in phase viscosity. In this study, the relevant segregation-compaction length relates to the segregation of the liquid accommodated by the compaction of the solid. To calculate this length over all phase fractions, we follow Keller & Suckale (2019) and apply transfer coefficients calibrated to a mixture of olivine crystals and basaltic melt (Figure 1, Figure A1, Table A1). The calibration ensures that coefficients reduce to pure-phase properties at the solid-rich and liquid-rich limits, that the low wetting angle of basaltic melt on olivine crystals yields a low percolation threshold (here found to be at $\phi^\ell = 0.0007$) and that the solid matrix disaggregates at $\phi^\ell \sim 0.3$ (detail in Appendix A2.1). The shape of the resulting curve can be used to designate flow regime boundaries, and gives a lower bound on the length scale where we expect mixture flow to emerge. For crustal magmatic systems, a calibration relating to silicic compositions dominated by plagioclase crystals and dacitic to rhyolitic melt would be more directly relevant. We proceed with the original calibration, however, due to the more abundant experimental and theoretical constraints available from studies

of partially molten mantle materials. We examine the applicability of the results to silicic systems in the discussion.

At low liquid fractions ($\phi^\ell < 0.07$), the segregation-compaction length increases sharply with liquid fraction from < 1 m around the percolation threshold until it reaches a maximum of 3.4 km. We refer to this as the *porous flow regime*. This increasing trend is consistent with the compaction model (McKenzie, 1984), where increasing liquid fraction enhances permeability, and allows more rapid liquid percolation. At intermediate liquid fractions ($\phi^\ell = 0.07 - 0.42$), the segregation-compaction length contracts first gradually and then more steeply with liquid fraction. We refer to this as the *mush flow regime*. With increasing liquid fraction, solid grain boundaries gradually become wetted by melt leading to the disaggregation of the contiguous solid matrix around the disagreggation threshold of $\phi^\ell = 0.3$. Contraction of the inherent length scale suggests that localisation of liquid segregation and mixture flow will be a prominent feature in this regime. The fact that the inherent length scale operates on the same range in both the mush and porous flow regimes suggests that models for both should employ the governing equations in the limit of finite R (22), unless a domain size much larger than the largest δ_0^{jk} is considered, in which case the ZSCL limit (23) may be appropriate.

Increasing the liquid fraction further still ($\phi^\ell > 0.42$) causes the segregation-compaction length to decrease to the solid grain size, where it remains approximately constant for the remaining phase space. We designate this the *suspension flow regime*. We define the regime transition from mush to suspension flow where the segregation-compaction length is ten times the grain size. Solids, which are no longer in contact with one another, can only sustain pressures distinct from the suspending liquid to a maximum length scale of one grain size. Therefore, phase pressure differences on the magmatic system scale will be negligible and the governing equations reduce to the ZSCL limit (23). In this regime, the suspended solid phase can be considered more mobile for segregation so that $\mathbf{v}_\Delta^j = \mathbf{v}_\Delta^s$, the segregation speed of particle settling.

3 NUMERICAL IMPLEMENTATION

While the reduced forms of the governing equations arising from dimensional analysis are instructive and may be used to model the system in pertinent limits, the numerical model employed in the remainder of this study will solve the original dimensional governing equations (3)–(4). In two dimensions, the governing equations comprise two momentum balance equations (1b) in the two spatial directions, one mass balance equation (1a), and an additional equation for the time evolution of phase fractions $\partial\phi^i/\partial t$ for each phase $i = 1, 2, ..., n$. These $4 \times n$ equations are solved on a two-dimensional (2D), square, equidimensional domain of size $D \times D$ for the solution variables of horizontal velocity u^i, vertical velocity w^i, dynamic pressure p^i (reduced by lithostatic pressure) and phase fraction ϕ^i fields for each phase i in space (x, z) and time t, summarised in the solution vector $y^i(x, z, t) = [u^i, w^i, p^i, \phi^i](x, z, t)$. The origin of the coordinate system is in the centre of the domain such that $x, z \in [-D/2, D/2]$.

3.1 Boundary and initial conditions

The numerical model implementation provides a choice between closed and periodic boundary conditions. For closed boundary conditions, phase velocities and volume fluxes normal to each boundary, as well as shear stresses parallel to each boundary, are set to zero,

$$\mathbf{v}^i\left(x = \pm\frac{D}{2},\ z = \pm\frac{D}{2},\ t\right) \cdot \mathbf{n} = 0\,, \tag{24a}$$

$$\mathbf{q}_\phi^i\left(x = \pm\frac{D}{2},\ z = \pm\frac{D}{2},\ t\right) \cdot \mathbf{n} = 0\,, \tag{24b}$$

$$q_{v,xz}^i\left(x = \pm\frac{D}{2},\ z = \pm\frac{D}{2},\ t\right) \quad = 0\,, \tag{24c}$$

with $\mathbf{n}$ the unit vector normal to the boundary. This choice of boundary conditions simulates a magmatic domain with impermeable, shear stress-free boundaries. Buoyancy-driven phase segregation is obstructed by horizontal boundaries, leading to the formation of boundary layers along the top and base of the domain.

For periodic boundary conditions, all solution variables on boundaries are set such that the solution periodically repeats itself in both horizontal and vertical directions

$$y^i\left(x = -\frac{D}{2},\ z,\ t\right) = y^i\left(x = \frac{D}{2},\ z,\ t\right)\,, \tag{25a}$$

$$y^i\left(x,\ z = -\frac{D}{2},\ t\right) = y^i\left(x,\ z = \frac{D}{2},\ t\right)\,. \tag{25b}$$

These boundary conditions are used to simulate flow in a part of a larger magma reservoir and avoids obstruction of flow and build-up of de-/compaction layers along boundaries. To avoid spurious solution drift due to accumulated numerical errors, we subtract the mean of the solution update after each solve.

As we assume non-inertial flow with incompressible phase materials, phase fractions are the only time-dependent solution variable for which initial conditions are required. We specify uniform background phase fractions superposed with smooth random perturbations of a set amplitude and smoothness, and/or a two-dimensional Gaussian perturbation of a set size and amplitude at the centre of the domain. Other specific functional forms of phase fraction perturbations can be specified as used for the 1D column models in Sections 4.2.1 and 4.2.2.

3.2 Numerical discretisation

The governing equations are discretised using finite differences on a staggered grid of $N \times N$ square and equidimensional cells of discrete step size h. Scalar degrees of freedom p^i, ϕ^i are located at cell centres, whereas vector components u^i, w^i are located on vertical and horizontal cell faces respectively (e.g., Gerya, 2019). Fluxes are calculated using central differencing, whereby horizontal vector flux components come to be located on vertical cell faces, and vertical components on horizontal faces, where the respective velocity components are also located. Normal ($xx-$, $zz-$) components of the deviatoric strain rate tensor are located on cell centres, while its shear ($xz-$) components are located on cell corners. All coefficients are calculated on cell centres. Where any p^i, ϕ^i, or coefficients are required at cell faces or corners, they are evaluated there by arithmetic averaging from adjacent cell centres.

As an alternative to the standard 2D equidimensional mode, the model can also be run in a pseudo-1D mode. This mode is automatically selected if the specified initial condition on phase fraction does not contain horizontal variations. The 2D-equations are solved on a grid of N points in the vertical direction, and two points in the horizontal direction. The horizontal momentum balance equation is still solved but horizontal velocity and flux components remain zero (within computational accuracy). This mode is applied

for 1D column models in Section 4.2. If the specified initial condition includes variations in the horizontal direction, the equations are solved on the full 2D, $N \times N$ grid.

To sufficiently resolve both phase segregation and mixture flow requires appropriate choices of cell and domain size. Tests show that at least one cell is needed to resolve each segregation-compaction length in the suspension flow regime, and at least five cells for the porous and mush flow regime (Appendix D). On the other hand, the domain must be at least 10 times the segregation-compaction length to enable de-/compaction boundary layers to develop, as noted in compaction models which show that compaction pressures decay and segregation speeds grow exponentially away from closed boundaries or perturbations to phase fraction with the segregation-compaction length as the e-fold length (e.g. Katz, 2022, Chapter 6). The domain must be still larger, at least 30 times the segregation-compaction length for phase fraction perturbations to induce mixture flow comparable to the phase segregation speed, as will be shown in Section 4.1.

To ensure that the domain size is chosen appropriately, the numerical model first evaluates δ_0^{jk} given the selected background phase proportions and material properties, before setting the domain size as a user-defined multiple of the largest δ_0^{jk} in the system. The user should also choose a sufficient number of grid points N to ensure that δ_0^{jk} is well resolved on the numerical grid. Insufficient numerical resolution will adversely affect the quality of the solution as well as solver convergence.

In the liquid-rich regime, the segregation-compaction length is at the grain scale, therefore requiring a cell size of the same order or smaller than the grain size. This may appear to violate the continuum assumption, where it is typically assumed that a numerical cell corresponds to a control volume containing a large number of local-scale phase constituents, the behaviour of which is described by volume averaging at the continuum scale (Keller & Suckale, 2019). However, an alternative approach to continuum mixture theory instead interprets continuum phase fields in terms of ensemble averaging (Drew & Passman, 1999; Oliveira et al., 2018). While the governing equations remain the same, the ensemble averaging interpretation understand each point on a continuum field as representing the average of many physically possible realisations of local-scale phase topology and phase interactions. For example in the suspension regime, a point with a small, finite solid fraction does not represent the volume average of many particles within a representative volume element. Instead, this point should be interpreted as the ensemble average of many realisations of which only a few realisations have a particle occupying that location instead of the carrier liquid. We discuss the implications of this interpretation in Section 5.3.

The time derivative in the phase fraction equation is discretised by the second-order, semi-implicit Crank-Nicolson scheme using central finite differencing in time. For stable numerical integration in time, the time step size is limited by either the Courant-Friedrich-Lewy (CFL) criterion on the volume flux, or by limiting volume transfer to a 0.5% change in phase fraction,

$$\Delta t \leq \frac{\mathrm{CFL}}{\frac{1}{h/2}(\max|\mathbf{q}_\phi^i|) + 0.005(\max|\Gamma_\phi^i|)} \,. \tag{26}$$

The selected time step size is a specified fraction CFL of the harmonic sum of the volume flux and transfer limits.

3.3 Non-linear iterative solver

The governing equations are non-linear because constitutive relations comprise non-linear combinations of solution variables while coefficient closures are non-linear functions of phase fractions. To solve the governing equations at each time step, we apply Polyak's heavy ball method (Polyak, 1964), a pseudo-transient iterative strategy that has been applied to large numerical problems in geoscience including the two-phase compaction model (e.g. Räss et al., 2019; Wang et al., 2021) due to its efficient scaling properties. Iterative methods of this kind scale better with increasing numerical resolution than direct matrix solvers. For an n-phase model with $N \times N$ grid cells, iterative methods only require $\mathcal{O}(n \times N \times N)$ operations, while direct methods require $\mathcal{O}((n \times N \times N)^3)$ operations. Although not attempted here, pseudo-transient iterative methods require mostly local numerical operations and hence are amenable to efficient parallelisation (e.g., Räss et al., 2019).

In the pseudo-transient method, the governing equations are put into a form of a pseudo-time-dependent equation, where the rate of change of the solution variable is the residual of the original equation. This pseudo-time-dependent equation is then integrated with explicit pseudo-time stepping until a steady-state is reached, where the rate of change (i.e., the residual) approaches zero and hence the solution to the governing equations is found. Applying this method to our model, the solution variables at the kth iteration, y_k^i, are updated using the residual at the current iteration, R_k^i and the solution guess from the previous iteration, y_{k-1}^i,

$$y_{k+1}^i = y_k^i - \alpha\,\Delta\tau\,R_k^i + \beta(y_k^i - y_{k-1}^i)\,, \tag{27}$$

where $0 < \alpha < 1$ is the iterative step size control, and $0 < \beta < 1$ acts as a damping parameter. This damping parameter further reduces the order of operations below power one, such that doubling the grid resolution requires fewer than double the number of iterations (Appendix D). Larger α, β can increase the speed of convergence, however smaller values (in particular for β) result in more robust convergence. $\Delta\tau$ is the stable pseudo-time step size. In a purely linear system of equations $Ay = b$ where A is diagonally dominant, $\Delta\tau$ is equal to the inverse of the diagonal entries of A. In our non-linear system of governing equations, a combination of flux and transfer coefficients approximate the diagonal entries of A to derive $\Delta\tau$,

$$\Delta\tau_{\mathbf{v}}^i < \left[\frac{K_v^i}{(h/2)^2} + (1-\omega_{C_v}^i)C_v^i\right]^{-1}\,, \tag{28a}$$

$$\Delta\tau_P^i < \left[\frac{K_\phi^i}{(h/2)^2} + (1-\omega_{C_\phi}^i)C_\phi^i\right]^{-1}\,, \tag{28b}$$

$$\Delta\tau_\phi^i = \frac{1}{16}\Delta t\,, \tag{28c}$$

where $\Delta\tau_{\mathbf{v}}$ applies to the two velocity components, $\Delta\tau_P$ applies to pressure and $\Delta\tau_\phi$ applies to phase fraction. $\omega_{C_v}^i$ and $\omega_{C_\phi}^i$ are the weights used in averaging phase-wise fields to obtain reference velocity and pressure, respectively. Since the phase fraction equation simply relates $\partial\phi^i/\partial t$ to Γ_ϕ^i, we choose for $\Delta\tau_\phi^i$ an arbitrary fraction $< 1/2$ of the stable (physical) time step Δt. Testing different fractions did not affect solution convergence, because the velocity-pressure solution mainly controls convergence. The convergence is stopped when the L2 norm of R_k^i normalised by the norm of the solution vector decreases below a specified absolute or relative convergence tolerance. The algorithm also allows for a convergence criterion by maximum number of iterations, but this should be used with caution for purposes of efficient testing only.

To reduce computational time, we only update the flux and

transfer coefficients after a set number of iterations. This is because phase fractions do not vary greatly between iterations, but the updating of coefficients requires a number of power operations which are relatively computationally expensive. The convergence of the iterative algorithm was verified using the Method of Manufactured Solutions and shows second-order convergence with spatial resolution as expected for the staggered-grid central differencing scheme used to discretise the governing equations (Appendix C).

3.4 Numerical stabilisation

The large contrast in pure-phase solid and liquid viscosities typical for magmatic systems (here 16 orders of magnitude) can cause flux and transfer coefficients to take on vastly different magnitudes with modest changes in phase proportions. For example, around the solid disaggregation threshold ($\phi^\ell = 0.3$), the solid transport coefficients vary by three orders of magnitude over a 0.05 change in phase fractions (Figure A1). Such large coefficient contrasts can lead to numerical round-off errors and poor iterative convergence.

To stabilise the iterative scheme, we introduce two limiting controls: one to limit contrasts in permission functions within each phase across the domain, `thtlim`, and a second to limit contrasts of flux/transfer coefficients between phases in each grid cell `cfflim` (detailed in Appendix B). The limiters are designed so that their effect vanishes when set to large values (e.g. 10^{16}). However, when set to smaller values (e.g. $10^4 - 10^6$), they bring phase segregation speeds in the system to within that value of the fastest segregation speed. For example, in the porous flow regime, setting `cfflim` to 10^4 brings the solid segregation speed scale u_0^s to within 10^4 of the liquid segregation speed scale u_0^ℓ. Nevertheless, the solid segregation speed remains negligible on the time scale of the simulation, which resolves the more rapid liquid segregation. `thtlim` has the same effect applied to speed scale variations within one phase across the domain.

In endmember suspension and porous flows for two-phase mixtures, tests show that both limiters can be set to large values without affecting convergence. However, around the solid disaggregation threshold, we find by experimentation that `thtlim` needs to be reduced to 100 to achieve good convergence over longer simulations. We confirm that simulations using this small `thtlim` have consistent flow features with simulations using larger values ($\geq 10^4$), but enable the simulations to run for longer times without diverging to handle the more pronounced localisation over time. `thtlim` crucially controls the range of the solid phase effective shear viscosity K_v^s, which changes by orders of magnitude at the disaggregation threshold.

We interpret the choice of 100 to be governed by grid resolution: given that the segregation-compaction length is inversely proportional to the square root of the transfer coefficients, setting the limiters to 100 limits the contraction of the segregation-compaction length with increasing liquid fraction to 10. Since we use around $5-10$ cells per segregation-compaction length at the beginning of the simulation, a limiter of 100 prevents the segregation-compaction length from going too far below the grid resolution in regions with growing liquid fraction. Increasing the number of grid cells should allow larger coefficient contrasts; however, in practice we cannot increase the number of grid cells by orders of magnitude while maintaining reasonable computation times.

4 RESULTS

In this section, we test the numerical model at different initial phase fractions to characterise the flow regimes arising from a two-phase solid-liquid mixture. We use three model setups to highlight flow features with increasing dimensional complexity. First, we extract the characteristic magnitude of velocity and pressure fields given input phase fractions across the phase space to compare with the scaling relations derived in Section 2.2. Subsequently we employ 1D column models to demonstrate idealised endmember behaviours and the formation of boundary layers in confined magmatic systems. Finally, we use 2D simulations to demonstrate the interplay between phase segregation and mixture flow and the role of flow localisation across the three regimes. We emphasise that simulations from the porous to mush and suspension flow regimes are achieved with the same numerical model by adjusting inputs such as the initial condition on phase fractions and domain size.

4.1 Characteristic scales for velocity and pressure from numerical simulations

In the first test, we compare the characteristic magnitudes of the velocity and pressure fields from the numerical simulations with the analytical scales derived in Section 2.2. We initialise a series of simulations on a 2D square domain of size D at uniform background liquid fraction ϕ_0^ℓ but with a liquid-rich Gaussian perturbation of amplitude $\Delta\phi_0^\ell = 0.01$ and standard deviation $\sigma_0 = D/10$ in the centre. Periodic boundary conditions are applied for all variables on all boundaries, and both numerical stabilisation limiters are set to the computational limit of 10^{16}. Since the relative contribution of phase segregation and mixture flow depends on system size, we run simulations at two domain sizes: $D = 10\delta_0^{\ell s}$ and $D = 100\delta_0^{\ell s}$. Since liquid is the less dense phase, the liquid-rich perturbation can drive the upward branch of a convective flow cell, which is compensated by the downward flow of the background mixture. At the same time, liquid also segregates upwards from the solid phase due to buoyancy.

The analytical velocity and pressure scales are calculated using the relations from Section 2.2 assuming $\ell_0 = \sigma_0$, the standard deviation of the imposed Gaussian. Hence, the two sets of simulations correspond to $R = 1$ and $R = 0.1$, respectively. The density scales used in the following are,

$$\Delta\rho_0^i = \rho_0^i - \bar{\rho}_0 \,, \tag{29a}$$

$$\Delta\bar{\rho}_0 = \Delta\phi_0^\ell \cdot (\rho_0^s - \rho_0^\ell) \,, \tag{29b}$$

where $\bar{\rho}_0$ is the mixture density at the background phase fraction. The density contrast driving mixture flow, $\Delta\bar{\rho}_0$, is proportional to the density difference between the peak of the Gaussian perturbation and the background.

Figure 2 compares characteristic scales obtained from numerical simulations to those derived from scaling analysis. To obtain the scales from the numerical simulations, we extract the maximum values of the segregation velocity u_0^i, compaction pressure p_0^i and mixture pressure $\bar{p}_0$. Since convection is best characterised by a closed loop of upwelling and downwelling, we take the difference between the maximum and minimum mixture velocity as the characteristic mixture flow speed scale $\bar{u}_0$. We find good correspondence between the numerical and analytical values, indicating that the scaling analysis succeeded in extracting scales which properly characterise the dynamics across the three flow regimes.

The scale of the mixture flow speed (Fig. 2a) is an increasing function of liquid fraction as mixture viscosity $\bar{K}_{v,0}$ decreases by

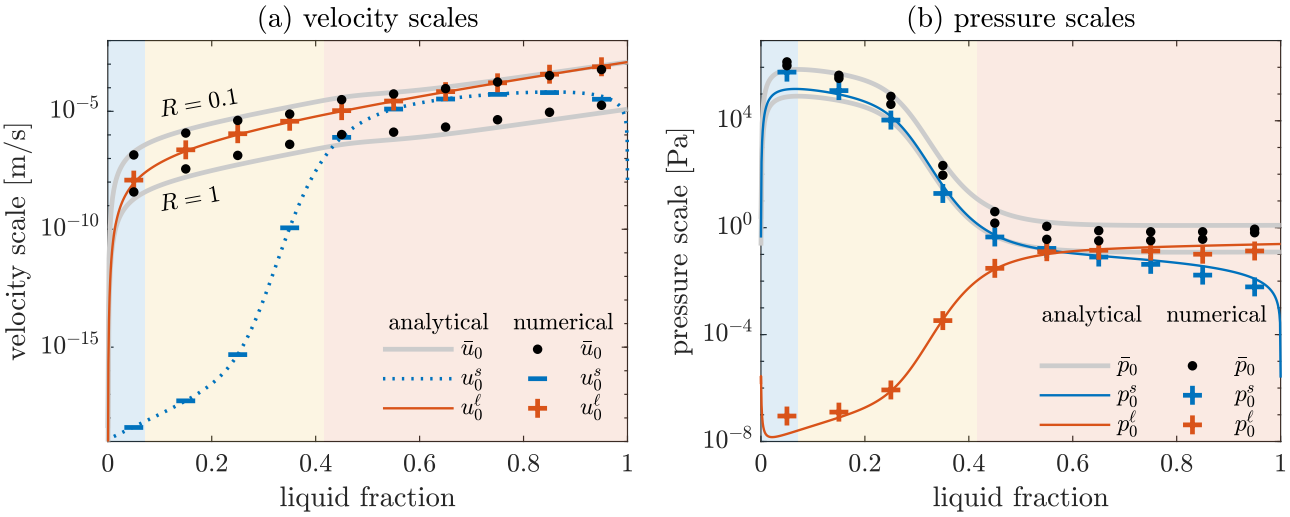

Figure 2. (a) Velocity and (b) pressure scales for simple simulations with a central liquid-rich Gaussian perturbation. In each plot, the numerical model results are shown by the discrete points (crosses for positive values, bars for negative values of the solid segregation velocity, dots for the mixture fields), compared against the theoretical relations shown by the lines (solid for positive values, dotted for negative values). For the mixture fields, trends for $R = 0.1, 1$ are shown. Background colours show the flow regimes as in Figure 1.

orders of magnitude, overwhelming the effects of variations in ℓ_0. In the porous flow regime, the solid segregation speed is negligible relative to that of the liquid phase. The solid phase is much more competent than the liquid, hence the velocity deviation from the solid phase to the reference velocity is approximately zero (here, $< 10^{-18}$ m/s). Across the mush regime, the solid segregation speed increases steeply. The solid phase is mobilised considerably, although its segregation speed still remains less than the other speeds in the system. In the suspension flow regime, both liquid and solid segregation velocities are similar in magnitude but opposite in sign.

Domain size impacts the relative contribution of phase segregation and mixture flow. In the porous and mush flow regimes, at $D = 10\delta_0^{\ell s}$ (R = 1), the mixture speed scale is about one orders of magnitude below the liquid segregation speed. In contrast, at $D = 100\delta_0^{\ell s}$ (R = 0.1), the mixture speed scale is at most one order of magnitude greater but approaches the liquid segregation speed scale with increasing liquid fraction. This suggests that at the smaller domain size, liquid segregation is the dominant process and limited mixture flow will occur, while at the larger domain size, mixture flow becomes appreciable.

The mixture pressure scale (Figure 2b) largely follows the variation of the segregation-compaction length (Figure 1) because the characteristic system length is taken as a constant multiple of the segregation-compaction length for each simulation. In the porous flow regime, $\bar{p}_0$ increases to a maximum on the order of MPa, then decreases across the mush flow regime, as the solid disaggregates and no longer sustains substantial stresses. Since liquid pressure dominates the mixture pressure in the porous flow regime, the liquid compaction pressure scale is small here. As expected from the compaction model, the solid compaction pressure scale $P_\Delta^s = \phi^s(p^s - p^*) \approx \phi^s(p^s - p^\ell)$ is large and proportional to the pressure difference between the phases, although the sign is opposite to the convention in McKenzie (1984). In the suspension flow regime, the mixture pressure decreases to a small value (∼Pa). Both compaction pressures are small because pressure differences can only be sustained over the length scale of the solid grain size.

The agreement between analytical scaling relations and numerical results shows that the scaling analysis identified the salient physical scales of the problem across the three flow regimes. It further emphasises the relationship between the domain size and the emergent physical length scale. Models with $R \geq 1$ show phase segregation dominating over mixture flow. In additional simulations (not shown here), we confirmed that models with smaller domain size (R $>$ 1) show dynamics fully dominated by phase segregation with hardly any mixture flow established. On the other hand, models with $R \sim 0.1$ allow both phase segregation and mixture flow to assume speeds within the same order of magnitude. We were not able to achieve models at R $\ll$ 0.1 because they require very high numerical resolution ($>$ 5 grid cells per $\delta_0^{\ell s}$ required).

4.2 1D column models

We analyse a series of 1D column models to demonstrate that our model reproduces important features of the porous and suspension flow regimes known from previous endmember models. We then examine boundary layer formation in systems confined by impermeable boundaries across the three flow regimes. The models are initialised on a pseudo-1D domain with phase fraction perturbations in the vertical direction only. As a result, vertical fluxes develop while horizontal fluxes remain zero, thus 1D column models are ideal for studying buoyancy-driven phase segregation.

4.2.1 *Liquid segregation in the porous flow regime: Porosity waves*

Numerous studies have examined the development of porosity waves from porous flow through a deformable matrix based on the compaction model (McKenzie, 1984; Katz, 2022). Ahead of liquid-rich perturbations, buoyancy-driven liquid overpressure will cause viscous decompaction of the matrix and hence an increase in liquid fraction. At the trailing end of the perturbation, the opposite process occurs: the matrix compacts and liquid is expelled. This

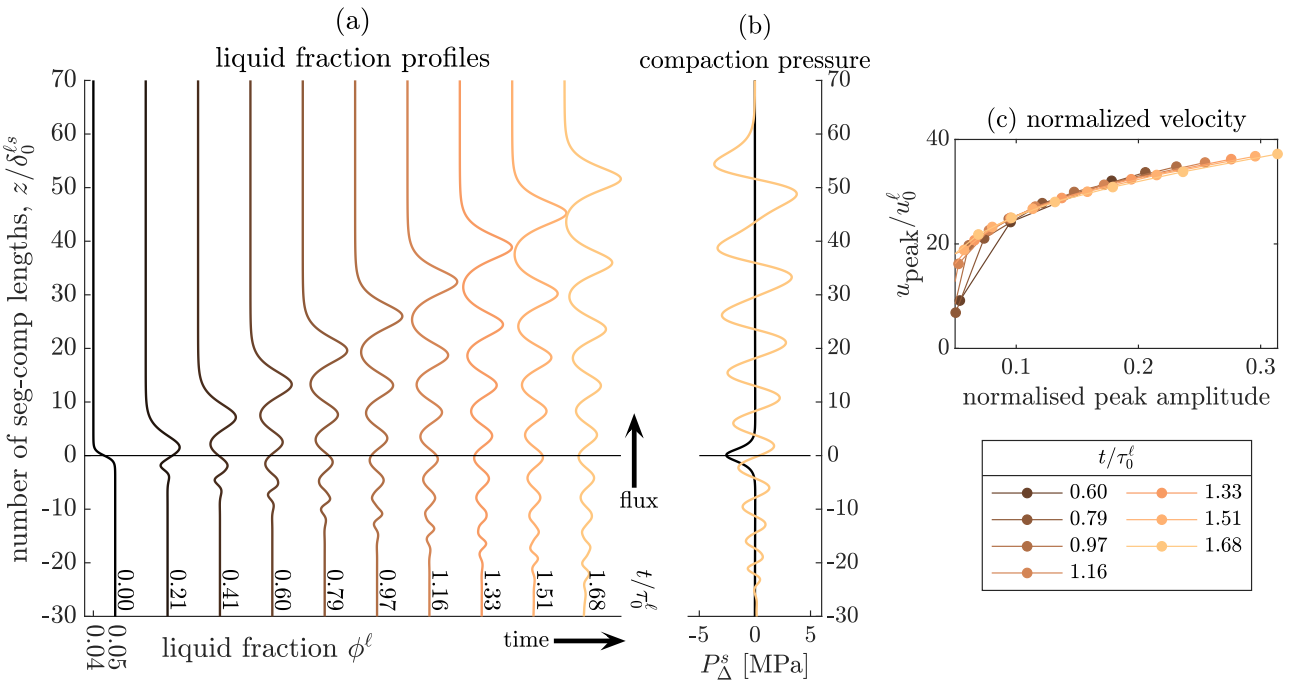

Figure 3. Evolution of (a) liquid fraction ϕ^ℓ, plotted by time normalised by the liquid percolation timescale τ_0 for a 1D permeability barrier test. (b) Compaction pressures $P_\Delta^s \approx \phi^s(p^s - p^\ell)$ of the first and last time step. (c) Normalised velocity of porosity wave peaks against normalised amplitude given by $(\phi^\ell - 0.05)/0.05$.

gives rise to porosity waves that propagate against gravity faster than the speed of liquid percolation through the pore space (Barcilon & Richter, 1986; Scott & Stevenson, 1986).

We test the emergence of porosity waves from our numerical model using a 1D permeability barrier test, where a step down to lower liquid fraction is imposed in the direction of liquid percolation (leftmost profile in Figure 3a). The permeability barrier is smoothed for numerical stability. Liquid ascends through the solid matrix due to buoyancy, hence the prevailing flux direction is upward. As the liquid encounters a region of lower liquid fraction, permeability drops and the liquid flux decreases. The solid compaction pressure, $P_\Delta^s \approx \phi^s(p^s - p^\ell)$, is initially negative at the barrier because the liquid is at a higher pressure than the solid (Figure 3b). The liquid decompacts (i.e., volumetrically expands) the solid matrix, causing an accumulation of liquid at the barrier (second profile in Figure 3a). However, this drains the zone immediately below, leading to matrix compaction and a decrease in liquid fraction there. This forms a new permeability barrier, where liquid accumulates and drains the region immediately below. Successive cycles of decompaction ahead and compaction behind emergent permeability barriers cause a train of porosity waves to develop, similar to those shown in Spiegelman (1993b) and Katz (2022). The wavetrain is rank-ordered: the wave with the largest amplitude leads successive waves of diminishing amplitude. The porosity wavetrain mostly propagates upwards but new trailing waves also migrate downwards as shown by the porosity perturbations below the coordinate origin at later times. We normalise simulation time by the percolation time scale, $\tau_0^\ell = \delta_0^{\ell s}/u_0^\ell$, where u_0^ℓ is given by (12). At the simulation end time of $t/\tau_0^\ell = 1.68$, the leading wave has advanced $52\delta_0^{\ell s}$. The leading wave has thus traveled, on average, $52/1.68 = 31$ times faster than the liquid, which moves at u_0^ℓ.

Analytical solutions to the compaction equations under idealised conditions permit solitary wave solutions, which are shape-preserving waves that propagate at a constant speed proportional to their amplitude (Scott & Stevenson, 1984; Barcilon & Richter, 1986; Stevenson & Scott, 1991). Our model gives rise to porosity waves but these are not strictly solitary waves, because solitary wave solutions require simple log-linear dependence of compaction viscosity, matrix shear viscosity and matrix permeability on liquid fraction, as well as constant liquid viscosity. The permission functions in the present model do not conform to such idealised material properties. Nevertheless, the shape of the leading wave strongly resembles analytical solutions, and the general relationship of higher wave speeds for larger wave amplitudes still holds (Figure 3c). We normalise peak amplitudes by 0.05, the background liquid fraction below the permeability barrier, and wave speeds by u_0^ℓ, the liquid segregation speed scale. At each time step, the rightmost point represents the leading wave, which has the largest peak amplitude and propagates at highest speed. Going leftwards, each subsequent wave is of lower peak amplitude and speed. At later times, waves grow in amplitude and develop a positive, non-linear amplitude-speed relationship that remains consistent through further time steps. Some small amplitude waves at early time fall below this amplitude-speed relationship, which we interpret as incipient, poorly-developed waves that eventually grow to follow the expected trend. In higher dimensional simulations, we expect rank-ordered porosity wavetrains that tend towards spherical geometries similar to solitary waves in idealised 2D and 3D models (e.g. Scott & Stevenson, 1986; Simpson & Spiegelman, 2011).

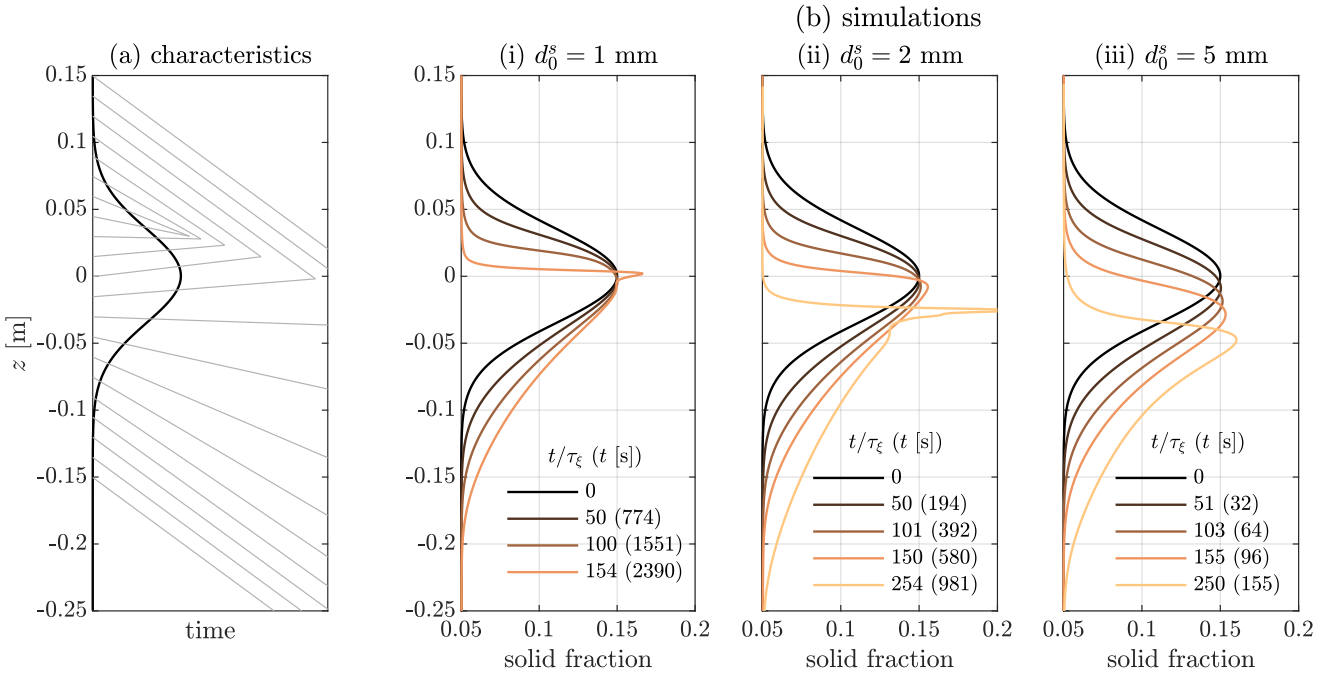

Figure 4. Evolution of a solid-rich layer in 1D models in the suspension flow regime. (a) Characteristics (thin gray lines) for the input Gaussian solid fraction profile (thick black line), showing a shock forming on the positive z side of the peak and a rarefaction forming on the negative z side. (b) Profiles of solid fraction for grain sizes $[1, 2, 5]$ mm from numerical solutions initialised by a background solid fraction of 0.05 and a Gaussian perturbation of amplitude 0.1. Profiles are adjusted by the background flux ν_0. Snapshots shown are at approximately the same normalised time t/τ_ξ using the background characteristic timescale, with time in seconds shown in parentheses.

4.2.2 *Solid segregation in the suspension flow regime: Concentration waves*

In the suspension flow regime, particle concentration waves develop if the solid segregation speed decreases with increasing solid fraction (Manga, 1996; Drew & Passman, 1999). This behaviour is expected from hindered Stokes settling, where the segregation speed decreases with a power law of solid fraction. Physically, backflow between particles dampens the settling speed of nearby particles, an effect that intensifies when particles are closer to one another. Our coefficient model is calibrated to a hindered Stokes settling model with a hindering factor of $(1 - \phi^s)^5$ (Keller & Suckale, 2019). Shock-rarefaction waves should form, where particle concentration increases in the direction of particle settling and leads to a particle "traffic jam" with a sharp tail developing into a shock over time but a widening front or rarefaction where particles can more freely settle into the lower concentration region below.

We test the numerical model in this regime by examining the evolution of a solid-rich layer against a uniform background solid fraction of $\phi^s = 0.05$. We first describe the behaviour by analysing the characteristics of the 1D governing equations (following Drew & Passman (1999) Section 22.3), then show a set of 1D numerical simulations that recover the expected behaviour. Assuming that (a) the solid and liquid phases are equilibrated in pressure as predicted by the scaling analysis, (b) the reference pressure and velocity are equally weighted by each phase (Figure A1) and (c) the momentum flux coefficient K_v^i is negligible, which is appropriate for liquid-dominated systems, we can simplify the governing equations (3) and express the phase velocity difference as

$$v^s - v^\ell = \frac{2\phi^\ell \phi^s (\rho^s - \rho^\ell) g}{C_v^s} \,. \tag{30}$$

Here we define $g = -9.81$ m/s^2, consistent with the equations in Section 2. Given a denser solid phase, $v^s - v^\ell < 0$, such that the solid phase settles downwards relative to the liquid. Equation (30) is consistent with the scaling relationship for the segregation velocity (12) taking the density scale as the deviation from mixture density. Substituting the velocity difference into the mixture mass balance (6a), we obtain the velocity of the solid phase,

$$v^s = \nu_0 + \frac{2\phi^{\ell^2} \phi^s (\rho^s - \rho^\ell) g}{C_v^s} \,, \tag{31}$$

where $\nu_0 = \phi^s v^s + \phi^\ell v^\ell$ is the volumetric flux obtained by integrating the mixture mass balance equation and is a constant. Given input values for viscosity, grain size and connectivity parameters A, B, C, the solid velocity v^s is purely a function of solid fraction. Thus, we can express the solid mass balance equation as

$$\frac{\partial \phi^s}{\partial t} + \left(v^s + \phi^s \frac{dv^s}{d\phi^s} \right) \frac{\partial \phi^s}{\partial z} = \frac{\partial}{\partial z} \left[K_\phi^s \left\{ \left(\frac{\partial p}{\partial z} \right)^s - \left(\frac{\partial p}{\partial z} \right)^\ell \right\} \right] . \tag{32}$$

The terms in parentheses on the left hand side form the characteristics of the solution, along which ϕ^s is a constant. Since v^s depends only on the solid fraction, the characteristic is constant for a given ϕ^s. For the material properties in this study (Table A1), the characteristics have negative values at $\phi^s = 0^+$ and increase with solid fraction, becoming positive and reaching a maximum at $\phi^s = 0.27$. We focus our analysis to solid fractions below this maximum value to stay well within the suspension flow regime. Applying the characteristics conceptually to a 1D Gaussian perturbation of higher solid fraction shows the evolution of the solid fraction profile over time (Figure 4a). Since the characteristics become less steep with increasing solid fraction, the characteristics

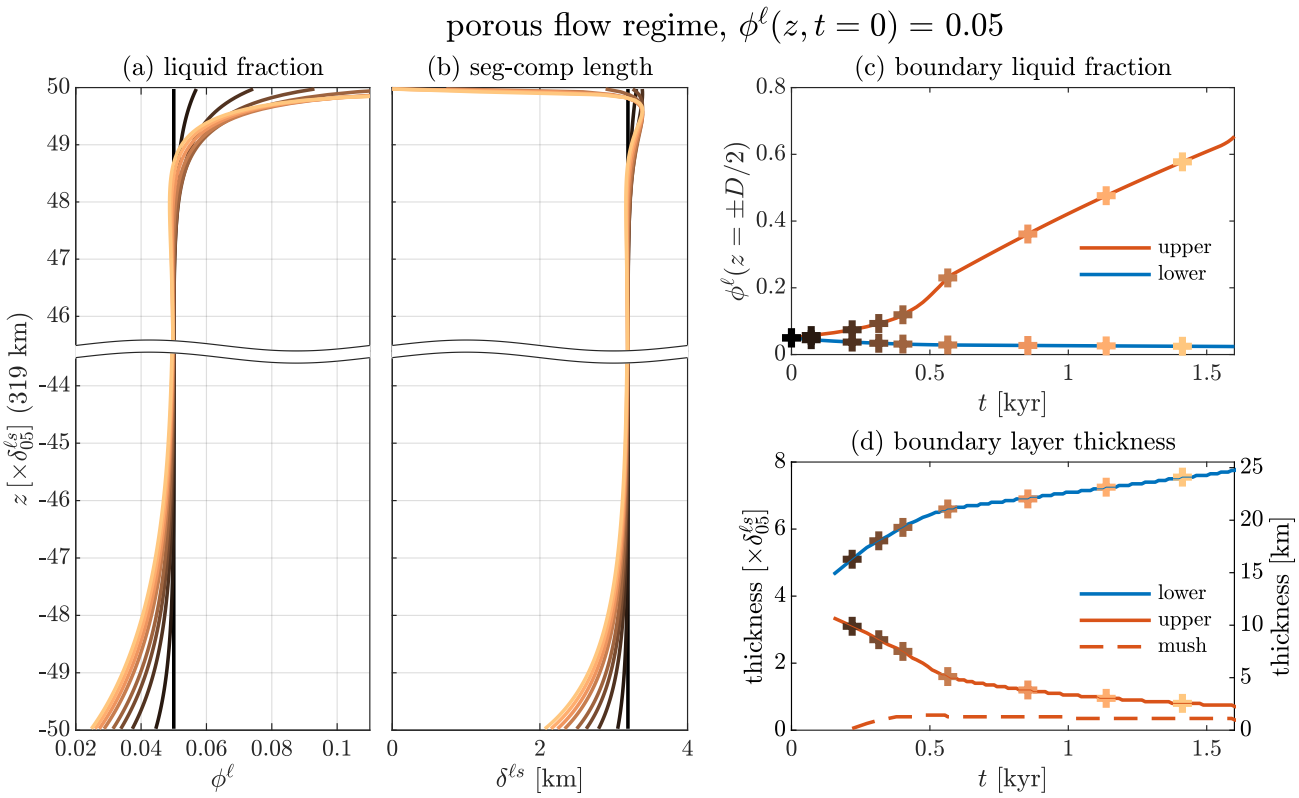

Figure 5. Boundary layer development in the porous flow regime with initial liquid fraction of 0.05. Profiles of (a) liquid fraction and (b) segregation-compaction length in depth normalised to the segregation-compaction length calculated at $\phi^\ell = 0.05$ ($\delta^{\ell s}_{05}$), with lighter colours indicating later times. The total domain size is 319 km. Profile times are indicated by crosses in (c), (d). Note that the vertical axis is broken and the horizontal axis is truncated to focus on the boundary layers. (c) Boundary liquid fraction in time. (d) Boundary and mush layer thickness over time in normalised units on the left axis and in dimensional units on the right axis.

converge along the positive z side of the Gaussian peak, forming a shock, and diverge along the negative z side, forming a rarefaction. The term on the right hand side of (32) is more cryptic. Based on suspension flow experiments and theory, Keller & Suckale (2019) tentatively interpreted this term to be related to the diffusion of phase fractions.

We test our numerical model against this analysis of characteristics using 1D simulations with different solid grain sizes (Figure 4b). The solid grain size affects both C^s_v and K^s_ϕ. In the profiles shown, we remove the constant background flux ν_0 to focus on the evolution of the solid-rich layer. We take snapshots at the same time normalised by the characteristic timescale $\tau_\xi = \Delta z / v^s$ of the background characteristic (i.e. at solid fraction 0.05), where Δz is the grid spacing and is the same for all three simulations. Due to the dependence of C^s_v on the square of the grain size, the characteristic timescale for the 2 mm and 5 mm simulations are 1/4 and 1/25 of the characteristic timescale for the 1 mm simulation respectively.

For each grain size, the solid fraction profile steepens on the upper side of the initial layer and spreads out on the lower side, as expected from particulate suspension theory and the analysis of characteristics. Since the velocity difference $v^s - v^\ell$ (30) is proportional to the square of the grain size through C^s_v, the peak of the largest grain size simulation has advanced the furthest. The numerical simulations suggest the term on the right hand side of (32) effectively acts as diffusion on phase fraction. Larger grain size increases K^s_ϕ, and the corresponding simulation shows a smaller shock amplitude compared to simulations at smaller grain size. We omit the profile for grain size 1 mm at $t/\tau_\xi \approx 250$ because it has oversteepened relative to the grid spacing and is affected by numerical dispersion. The simulations confirm that where the solid fraction is higher than the surroundings, the shock forms on the positive z side of the perturbation, that is, the trailing end of a wave of settling grains. Conversely, for a negative perturbation in solid fraction, we expect a shock to form on the negative z side of the perturbation. As a caveat, the formation of shock-rarefaction waves will be diminished if the background volumetric flux ν_0 is very large and dominates equation (31).

4.2.3 *Boundary layer development*

In confined magmatic systems with a denser solid phase and bounded by impermeable rock, phase segregation will lead to a solid-rich boundary layer forming at the base and a liquid-rich layer forming at the top. The thickness of these boundary layers is related to the segregation-compaction length (McKenzie, 1984; Richter & McKenzie, 1984; Katz, 2022). Since the segregation-compaction length depends on phase fraction, the boundary layer thickness should evolve asymmetrically as phase segregation progresses. We test the development of boundary layers from initially uniform phase fraction for three liquid fractions corresponding to the porous, mush and suspension flow regimes.

We test the porous flow regime at an initial liquid fraction of 0.05. As expected, solid-rich and liquid-rich boundary layers form at the bottom and top of the domain, respectively (Figure 5a). De-

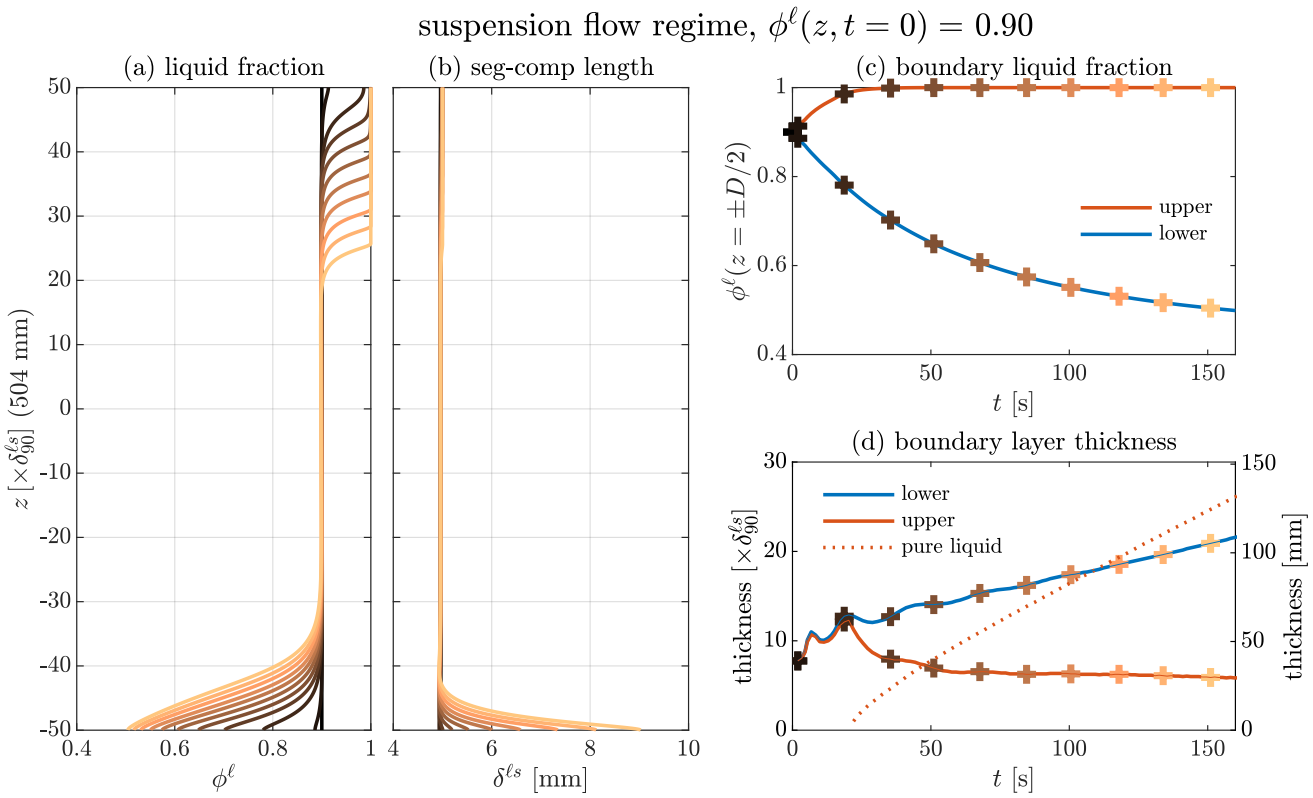

Figure 6. Boundary layer development in the suspension flow regime with initial liquid fraction of 0.90. Profiles of (a) liquid fraction and (b) segregation-compaction length in depth normalised to the segregation-compaction length calculated at $\phi^\ell = 0.90$ ($\delta^{\ell s}_{90}$), with lighter colours indicating later times. The total domain size is 0.5 m. Profile times are indicated by crosses in (c), (d). (c) Boundary liquid fraction in time. (d) Boundary layer and pure liquid layer thickness over time in normalised units on the left axis and in dimensional units on the right axis.

creasing liquid fraction at the bottom of the domain decreases the segregation-compaction length, while increasing liquid fraction at the top of the domain first increases then decreases the segregation-compaction length once the liquid fraction exceeds 0.07 (Figure 5b). Accumulation of the liquid fraction in the upper boundary layer increases slowly at first before increasing in rate then stabilising to an approximately constant rate (Figure 5c). Liquid fraction at the top of the domain reaches the mush transition of 0.07 liquid fraction after 220 years and the mush disaggregation threshold of 0.3 after 742 years, a rather short time in geological terms. As we show later, however, this mush layer remains relatively thin. Eventually, a pure liquid layer should form, but the segregation-compaction length at high liquid fraction becomes so small that it cannot be resolved by the numerical grid, and the simulation becomes numerically unstable before the pure liquid layer forms. The liquid fraction in the lower boundary layer decreases steadily at a slower rate.

To track the evolution of the boundary layer, we define its thickness as the distance over which the difference between the liquid fraction and the background value drops to 1% of the difference at the boundary. At early times, the liquid fraction profiles decay to the background liquid fraction over about 4 segregation-compaction lengths, consistent with the predictions from compaction theory (McKenzie, 1984; Katz, 2022). With time, the lower boundary layer becomes thicker, while the upper boundary layer narrows at the same rate (Figure 5d), even though at both boundaries, the segregation-compaction length should decrease overall. This thickening of the lower boundary despite a decreasing segregation-compaction length is the effect of matrix permeability and mass balance: since permeability increases with liquid fraction, liquid segregation is enhanced moving up the boundary layer, thereby causing it to widen (Richter & McKenzie, 1984). Furthermore, this widening lower layer explains the slower rate of liquid extraction. In contrast, the narrowing upper layer accumulates liquid at an increasing rate to maintain mass balance.

We additionally show the thickness of the mush layer through time to consider how a low liquid fraction system develops a mushy domain (dashed line in Figure 5d). We define the mush layer as the zone where the liquid fraction is above the porous to mush transition of 0.07. The initial progression to a mushy domain is fast, in which a 1 km thick mushy region forms within 320 years. However, the thickness of this region remains approximately constant despite continued liquid segregation because liquid segregation in the mush regime is much faster than in the porous flow regime and depletes liquid from just below the mush layer, which cannot be replaced fast enough by ascending liquid. Therefore the porous to mush transition does not migrate downwards within the time span simulated.

In the suspension and mush simulations, the thickening lower and thinning upper boundary layers are compounded by the substantial changes to segregation-compaction length with further increases in liquid fraction, enhancing the expected asymmetry (Figure 1). In the suspension flow regime, solid-rich and liquid-rich boundary layers again form at the bottom and top of the domain, respectively (Figure 6a). Since the evolving liquid fractions during this simulation remain well within the suspension flow regime,

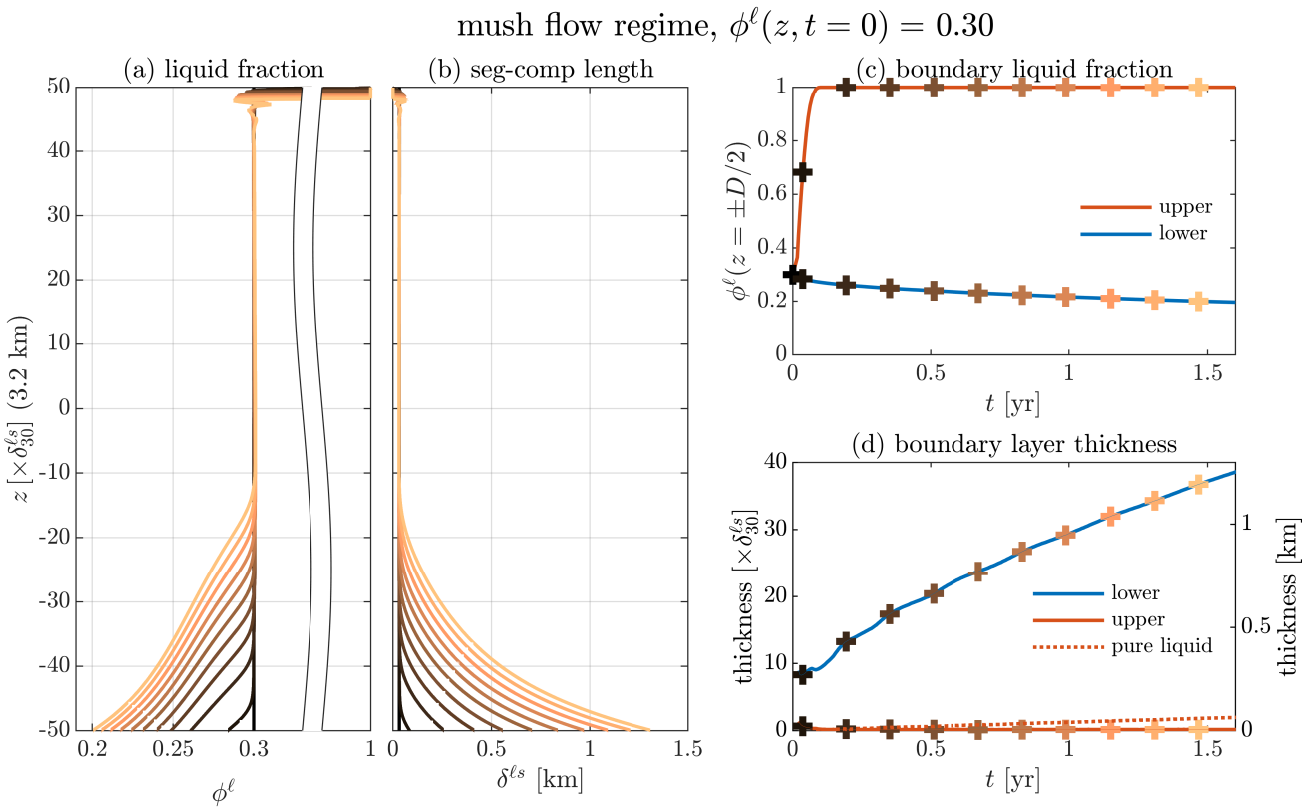

Figure 7. Boundary layer development in the mush flow regime with initial liquid fraction of 0.30. Profiles of (a) liquid fraction and (b) segregation-compaction length in depth normalised to the segregation-compaction length calculated at $\phi^\ell = 0.30$ ($\delta^{\ell s}_{30}$), with lighter colours indicating later times. The total domain size is 3.2 km. Profile times are indicated by crosses in (c), (d). Note that the horizontal axis in (a) is broken to focus on the boundary layers. (c) Boundary liquid fraction in time. (d) Boundary layer and pure liquid layer thickness over time in normalised units on the left axis and in dimensional units on the right axis.

the segregation-compaction length remains close to the grain scale of 5 mm throughout the 1D column (Figure 6b). As more liquid segregates upward, a pure liquid layer forms relatively soon at the top (Figure 6c). The topology of the boundary layer between the pure-liquid and background suspension layers reaches a steady-state with thickness approximately 6 $\delta^{\ell s}_0$ (red solid line Figure 6d) but migrates downward as the pure liquid layer grows in thickness. The lower boundary layer approaches a liquid fraction of 0.5, corresponding to the close packing solid fraction (red dotted line). The lower boundary layer thickens gradually, consistent with increasing segregation-compaction length with lower liquid fraction. In dimensional units, after 165 seconds, the pure liquid layer has grown to 0.14 m, whereas the cumulate pile at the bottom has grown to 0.11 m.

This asymmetry of boundary layer development is most pronounced in the mush regime (Figure 7a). The solid-rich compaction boundary layer shows a substantial increase in segregation-compaction length by over 40 times, from 32 m at the initial liquid fraction of 0.30 to 1.31 km at the minimum liquid fraction of 0.20 in the last time step shown (Figure 7b). At the upper boundary, the segregation-compaction length decreases towards the grain scale, as the liquid fraction progresses towards a pure liquid layer (Figure 7c). The pure liquid layer first forms at 0.08 years (31 days). The boundary between the pure-liquid layer and the background becomes thinner to a steady-state thickness of 0.15 $\delta^{\ell s}_0$, which is the resolution limit of the simulation (Figure 7d). The pure liquid layer grows in thickness as liquid continues to segregate from the mixture. In dimensional units, after 1.6 years, the pure liquid layer has grown to 62 m. Here liquid segregation is much faster than in the region below, causing a reduction of liquid fraction just below the boundary layer which acts as a slight segregation barrier that leads to an accumulation of liquid. This pattern is similar to the formation of rank-ordered porosity waves (Section 4.2.1), and also prevents the pure liquid layer from growing as quickly as in the suspension flow regime because the liquid cannot be supplied to this upper decompaction layer as easily. Meanwhile, the lower boundary layer grows gradually in thickness as its liquid fraction decreases. Therefore, in a confined magmatic mush body, we would expect a thickening crystal-rich cumulate layer to form at the bottom, while a thin liquid-rich layer emerges at the top.

4.3 Flow dynamics in 2D

The 1D simulations are well-suited to studying phase segregation across a vertical cross section of a magmatic system. However, the scaling analysis predicts that at large domain sizes, mixture flow can contribute to or even dominate the system dynamics. Mixture flow involves shearing, a necessarily two-dimensional phenomenon. Therefore, we design 2D simulations to contrast flow patterns arising from the three flow regimes. In each flow regime, we run simulations at two domain sizes to quantify the relative contribution of phase segregation and mixture flow to the overall system dynamics, and observe the differences in flow patterns in different regimes. All simulations are conducted with the same numer-

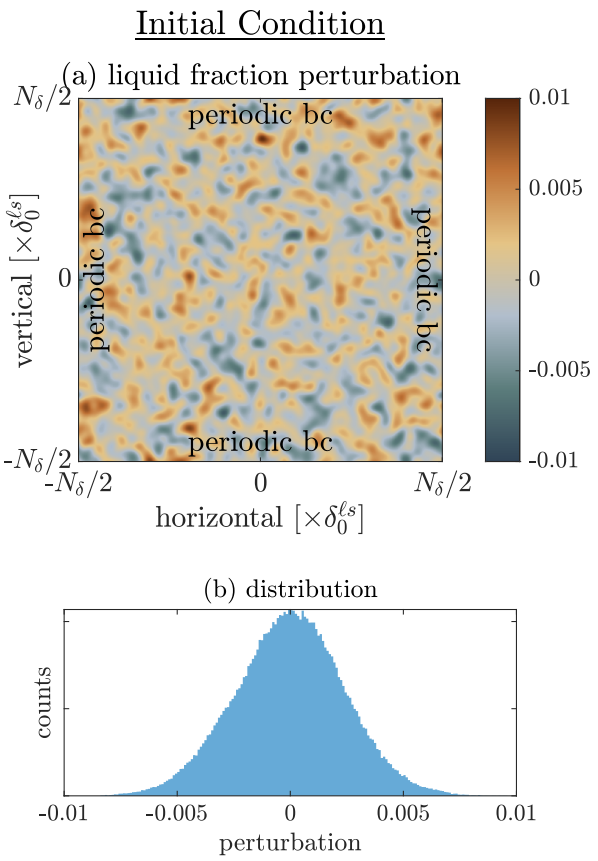

Figure 8. Initial condition for 2D simulations on a square domain. The background phase fraction ϕ_{bg} is perturbed by a normal distribution with maximum value of 0.01, and periodic boundary conditions are applied along all boundaries.

ical model from the previous sections, highlighting that the different flow regimes are natural consequences of the same underlying physics.

We choose the same background liquid fractions corresponding to the porous ($\phi^\ell_{bg} = 0.05$), suspension, ($\phi^\ell_{bg} = 0.90$) and mush ($\phi^\ell_{bg} = 0.30$) regimes as in the boundary layer analysis above. To the initial phase fractions, perturbations with a maximum amplitude of ± 0.01 are added, which approximate a normal distribution with a mean at zero and a standard deviation of 0.0025 (Figure 8). The boundary conditions are periodic on all sides. This implies that the domain represents a subset of a larger magmatic system that contains variations in phase fraction of a wavelength much smaller than the system size. Tests using closed boundary conditions show that boundary layer formation, as shown in Section 4.2.3, dominates dynamics and reduces to pseudo-1D phase segregation. For each liquid fraction, we run two simulations: one at small domain size ($N_\delta = 10$) and one at large domain size ($N_\delta = 100$ for porous and suspension flow regimes, $N_\delta = 50$ for mush regime due to resolution limits). The physical domain size is calculated as N_δ multiples of the segregation-compaction length at the background phase fraction. We run the model forward in time and examine the resulting flow patterns and timescales.

4.3.1 Porous flow regime: liquid percolation and solid compaction

Over a period of 10 kyr, simulations at high solid fraction and small domain size ($D = 10\delta_0^{\ell s}$) show the phases being organised into increasingly concentrated, horizontally layered bands (Figure 9a(i-iii), Supplemental Video S1). The bands do not form continuous layers, however, but show signs of contracting towards more spherical liquid-rich pockets. We interpret this as the emergence of porosity wave trains.

To quantify the relative contribution of phase segregation and mixture flow to overall dynamics, we compare the liquid segregation and mixture fluxes. By definition, the liquid segregation velocity $\mathbf{v}^\ell_\Delta = \phi^\ell(\mathbf{v}^\ell - \mathbf{v}^*)$ represents the volume flux of phase segregation, while the mixture velocity $\bar{\mathbf{v}} = \phi^s\mathbf{v}^s + \phi^\ell\mathbf{v}^\ell$ represents the volume flux of the mixture moving collectively. We normalise the liquid segregation and mixture fluxes by the segregation speed scale u^ℓ_0 (12), then scale the fluxes by a constant so that the segregation flux distribution has a standard deviation of unity. This normalisation enables comparison among all the simulations across flow regimes, since phase segregation fluxes are not affected by domain size but have differently wide distributions depending on phase fraction. The right plots in Figure 9 show the normalised fluxes: background colours of the 2D plot (Fig. 9iv) shows the vertical component of the normalised segregation flux overlain by the vectors of the normalised mixture flux $\bar{\mathbf{v}}$, which is divergence-free. The maximum vector length is given at the bottom left. The histograms to the right (Fig. 9v) show the distributions of segregation and mixture fluxes in comparison. If the distributions show similar widths, mixture flow occurs mainly in local response to phase segregation, which dominates the dynamics. If the width of the mixture distribution is much wider, mixture flow dominates dynamics and hence shows a variability that is decoupled from that of phase segregation.

For the small domain size simulation, the mixture flux vectors show no coherent convective pattern but tend to follow the vertically-oriented segregation fluxes (Figure 9a(iv)). The segregation and mixture fluxes have similar distributions (Figure 9a(v)). The normal distribution of the segregation flux around zero, which corresponds to the characteristic scale u^ℓ_0, further supports that the scaling analysis recovers the correct segregation velocity scale. As stated above, we interpret this as a segregation-dominated expression of the porous flow regime.

At the large domain size of $D = 100\delta_0^{\ell s}$, we observe that the liquid phase does not appear to become localised within a similar time as in the small-domain case, and that mixture convection becomes important (Figure 9b). While a few liquid-rich pockets do form, the extent of liquid localisation is not nearly as pronounced. In fact, after running this simulation to 122 kyr (Supplemental Video S2), we still do not observe a layered structure or the emergence of porosity waves. We note that it is difficult to perceive the convective pattern from the liquid fraction plots because the solid phase is relatively stiff and resists mixture deformation. The coherent convective cell pattern is more clearly represented with the mixture flux vectors (Figure 9b(iv)). The magnitude of mixture flux vectors is far larger than the range of the segregation flux. Convection stirs the phases and overwhelms phase segregation, and this is only possible when the domain is large enough to permit mixture convection cells to form. At > 300 km, the physical domain size of the large-domain test would span most of the upper mantle.

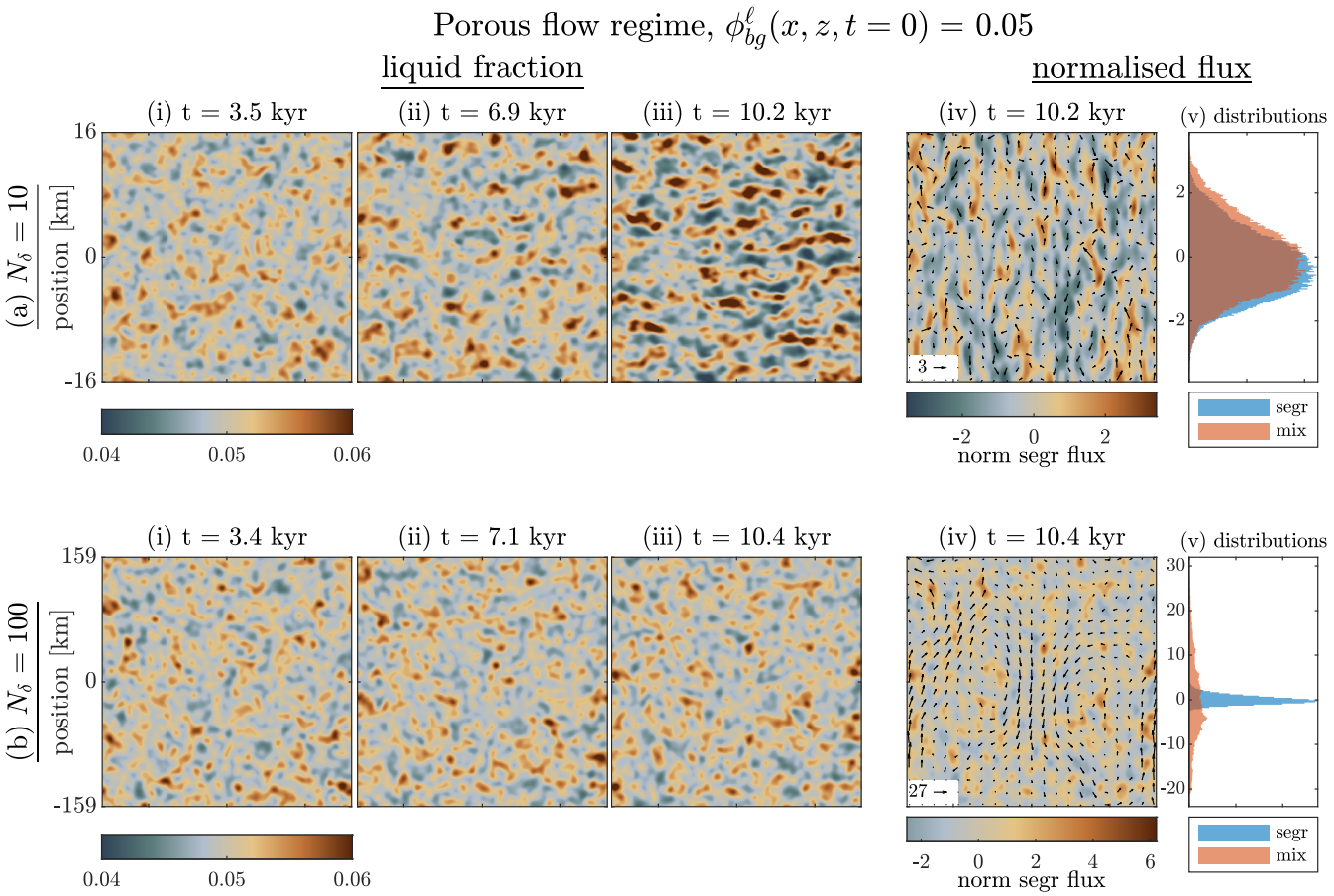

Figure 9. Simulations in the porous flow regime at two domain sizes, at (a) 10 ($N = 400$) and (b) 100 ($N = 500$) times the background segregation-compaction length. In each row, panels (i-iii) show snapshots of liquid fraction at approximately corresponding times. Panel (iv) shows the vertical liquid segregation flux as the background colours and the mixture flux as the vectors, with the maximum vector length indicated in the bottom left for scale. Panel (v) shows the distributions of the vertical components of normalised segregation (blue) and mixture (red) fluxes. All fluxes are normalised so that the standard deviation of the segregation (blue) distribution is 1.

4.3.2 *Suspension flow regime: hindered settling and mixture convection*

Simulations at high liquid fraction and small domain size show hindered settling of the solid phase as the dominant process (Figure 10a(i-iii), Supplemental Video S3). With time, initially liquid-rich regions become further enriched. A steepening phase fraction gradient develops on the lower side of the liquid-rich regions (red colours) and on the upper side of the liquid-poor regions (blue colours). These patterns correspond to emergent shock-rarefaction waves as predicted by the characteristics of the simplified equations in this regime (Section 4.2.2). No coherent convective pattern can be observed in the mixture vectors, although there is some alignment along liquid-rich channels (Figure 10a(iv)), suggesting that the mixture flux is driven by liquid backflow to solid settling. The magnitude and distribution of segregation and mixture fluxes are comparable for the small domain size simulation (Figure 10a(v)).

In contrast, mixture convection dominates system dynamics at large domain size (Figure 10b). Here we directly observe the effects of convection consistent with suspension flow behaviour: the central part of the domain rises in a convective upwelling accommodated by convective downwellings near the sides, causing visible distortion of initial phase perturbations (Supplemental Video S4). The mixture flux vectors form a coherent convective pattern in the 2D plot (Figure 10b(iv)).. The maximum vector magnitude is much larger than the range of segregation fluxes. The flux histograms also show that the mixture flux is decoupled from variations in segregation flux; it clearly dominates the system dynamics as it spans a range that is several times larger than the segregation flux (Figure 10b(v)). Note that the domain size in the suspension flow scenarios is of order centimeters. In natural magmatic systems, liquid-rich lenses may be up to several to hundreds of meters thick. Such systems would be even more strongly dominated by mixture convection.

4.3.3 *Mush flow regime: localisation of liquid into thin lenses*

Simulations in the mush flow regime show similar behaviour to the porous flow regime with some notable differences. In the small domain size simulation, the liquid again localises into near-horizontal layers to near-spherical pockets (Figure 11a(i-iii), Supplemental Video S5). However, the layers are much narrower than in the porous flow regime, because the segregation-compaction length contracts considerably with even small increases in liquid fraction, here typically a few percent at most. Again, the mixture and seg-

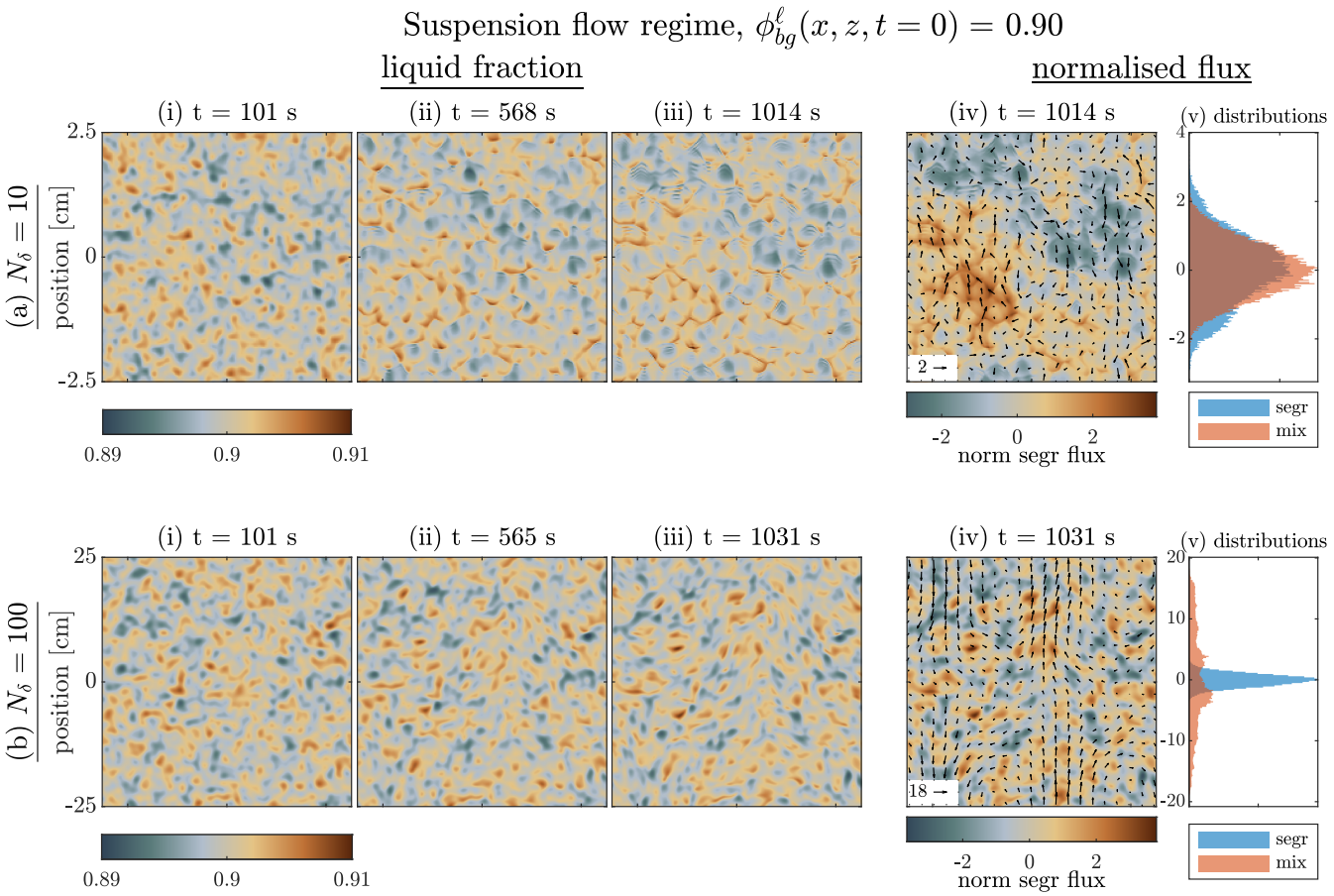

Figure 10. Simulations in the suspension flow regime at two domain sizes, at (a) 10 ($N = 400$) and (b) 100 ($N = 500$) times the background segregation-compaction length. In each row, panels (i-iii) show snapshots of liquid fraction at approximately corresponding times. Panel (iv) shows the vertical liquid segregation flux as the background colours and the mixture flux as the vectors, with the maximum vector length indicated in the bottom left for scale. Panel (v) shows the distributions of the vertical components of normalised segregation (blue) and mixture (red) fluxes. All fluxes are normalised so that the standard deviation of the segregation (blue) distribution is 1.

regation flux distributions are very similar (Figure 11a(iv-v)). The mixture flux vectors show strong alignment with the segregation flux field, because the mixture viscosity is greatly weakened in regions of high liquid fraction. We note that the timescale for the liquid-rich layers to form is on the order of years, very short relative to the expected lifetime of magma mush bodies.

At large domain size, localisation of the liquid phase is held off (Figure 11b(i-iii), Supplemental Video S6). While some liquid-rich pockets do become further enriched, this is not as pronounced as in the small domain simulation, and no liquid-rich layering emerges. This simulation was performed at $50\delta_0^{\ell s}$, smaller than the porous flow and suspension flow simulation pairs because of resolution constraints. Simulations for the mush flow regime, which traverse a larger range of segregation-compaction lengths, require higher numerical resolution to cope with strong localisation phenomena. Even so, this domain size already falls in the regime where mixture flux dominates the dynamics. Coherent convective cells emerge in the vector plot (Figure 11b(iv)). The maximum vector length and distribution range of the mixture flux are larger than the range of the segregation flux, but smaller than in the porous and suspension flow regimes.

4.3.4 Mush flow regime with imposed stress distribution to control orientation of liquid-rich channels

The mush flow regime is characterised by the increasing localisation of liquid into small pockets or bands over time. Previous studies showed that in the case where the matrix strongly weakens with increasing liquid fraction, liquid-rich regions will become more localised, and the orientation of these liquid-rich regions is affected by the principal stress directions in the system (Stevenson, 1989; Katz et al., 2006). Simulations in Section 4.3.3 show some hint of vertically oriented liquid layers, but the random orientations of the initial phase fraction perturbations obscure stress-related patterns in the localisation.

To examine the relationship between solid stress and liquid localisation, we run a simulation with a more conspicuous stress distribution driven by the buoyant rise of a strong liquid-rich perturbation in the domain, of amplitude 0.04 (Figure 12a(i-iii), Supplemental Video S7). Over the span of only 1.5 years, the initially Gaussian-shaped perturbation rises and decomposes into liquid-rich bands that radiate outwards from the upper part of the perturbation. These bands grow more liquid-rich and develop a characteristic spacing. Considering a vertical profile offset from the center of the domain as denoted by the white vertical lines, the liquid-

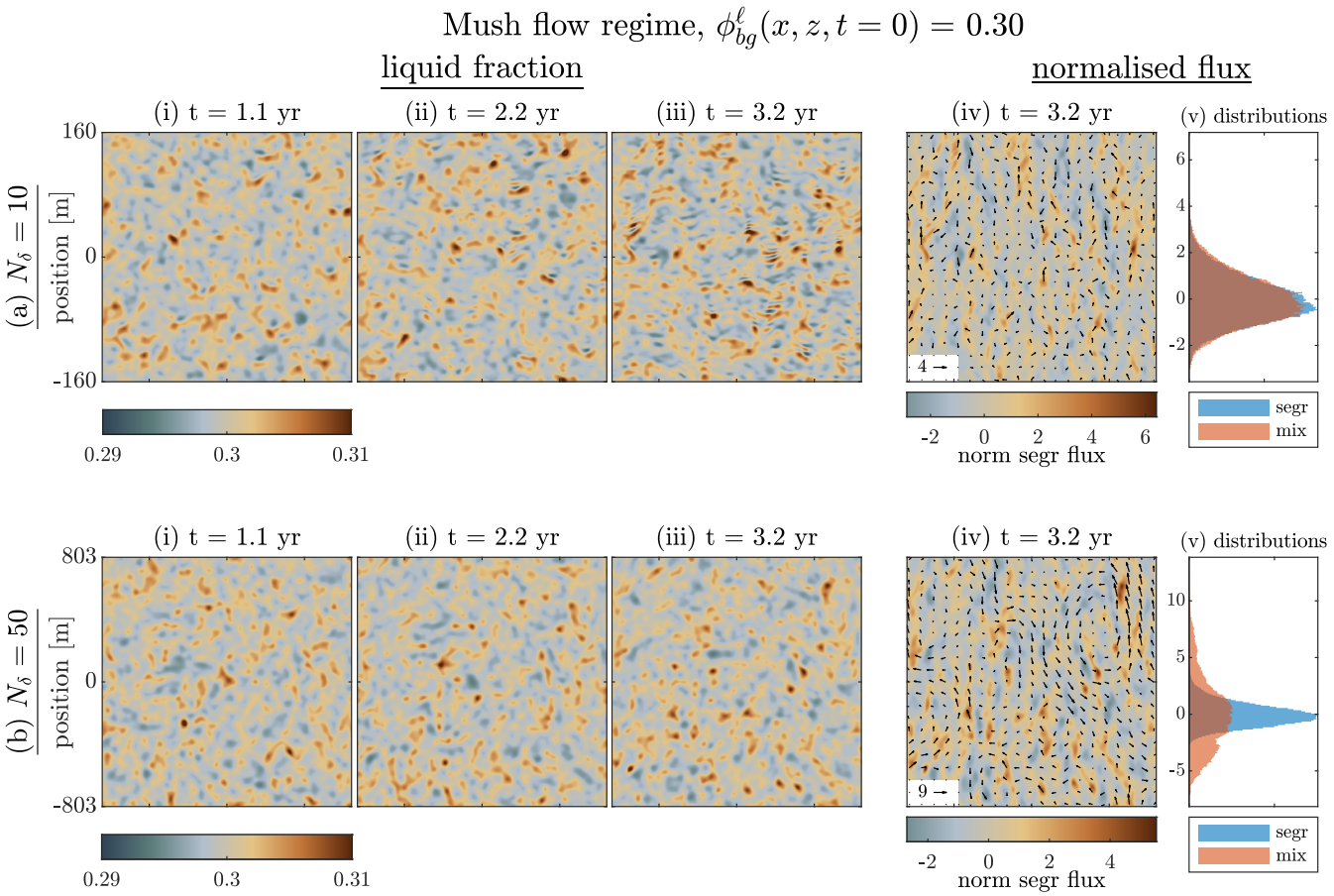

Figure 11. Simulations in the mush flow regime at two domain sizes, at (a) 10 ($N = 400$) and (b) 50 ($N = 600$) times the background segregation-compaction length. In each row, panels (i-iii) show snapshots of liquid fraction at approximately corresponding times. Panel (iv) shows the vertical liquid segregation flux as the background colours and the mixture flux as the vectors, with the maximum vector length indicated in the bottom left for scale. Panel (v) shows the distributions of the vertical components of normalised segregation (blue) and mixture (red) fluxes. All fluxes are normalised so that the standard deviation of the segregation (blue) distribution is 1.

rich bands are separated by 5 segregation-compaction lengths on average (Figure 12a(iv)). This characteristic spacing is consistent with the exponential decay of compaction pressures away from a permeability barrier with the segregation-compaction as the e-fold length (e.g. Katz, 2022, Chapter 6). Within this characteristic spacing, compaction pressures cause liquid to concentrate within the most liquid-rich perturbation at the expense of lesser ones.

The distribution of stress and strain rate of the solid phase should explain the orientation of the liquid-rich bands. Since the matrix is weakened by liquid, we expect the liquid-rich bands to localise where the strain rate magnitude is large, and that the liquid-rich bands orient approximately normal to the least compressive stress direction (Stevenson, 1989; Holtzman et al., 2003; Katz et al., 2006). To test this relationship, we show snapshots of the deviatoric strain rate magnitude and principal stress orientations (Figure 12b). Background colours show the magnitude of deviatoric strain rate, calculated from the square root of the second invariant of the deviatoric strain rate tensor, i.e. $\sqrt{\text{trace}(\underline{\mathbf{D}}^2)/2}$. The stress orientation is represented by two perpendicular lines, where the darker line indicates the direction of the least compressive stress σ_1 while the lighter line indicates the direction of the greatest compressive stress σ_2. The relative line lengths indicate the relative magnitude of the two stresses. All of the dark lines are normalised to 1, while the lighter line length is calculated by $1 + \log_{10}|\sigma_2/\sigma_1|$. Where the two lengths are similar, stress is isotropic; where the darker line is longer, stress is non-isotropic and the matrix is in a tensile stress state; where the darker line is shorter, stress is also non-isotropic but the matrix is in a compressive stress state.

Initially, the deviatoric strain rate magnitude is slightly higher in the liquid-rich perturbation (Figure 12b(i)). The local matrix stress distribution shows isotropic pressurisation of the matrix within the liquid-rich perturbation, but the rest of the domain displays a mostly random stress distribution resulting from the random perturbations in phase fraction. Over time, the rising perturbation induces a coherent stress distribution as a consequence of the developing convective mixture flow (Figure 12b(ii)). In the upper half of the domain, the rising perturbation causes the matrix to be mostly in a compressive stress state (darker lines are shorter), and the least compressive stress direction is oriented concentrically around the perturbation. In the lower half of the domain, the matrix is mostly in a tensile stress state (darker lines are longer), and the least compressive stress is oriented radially outward from the perturbation. In all of the domain, the bands of high deviatoric strain rates appear approximately perpendicular to the least compressive

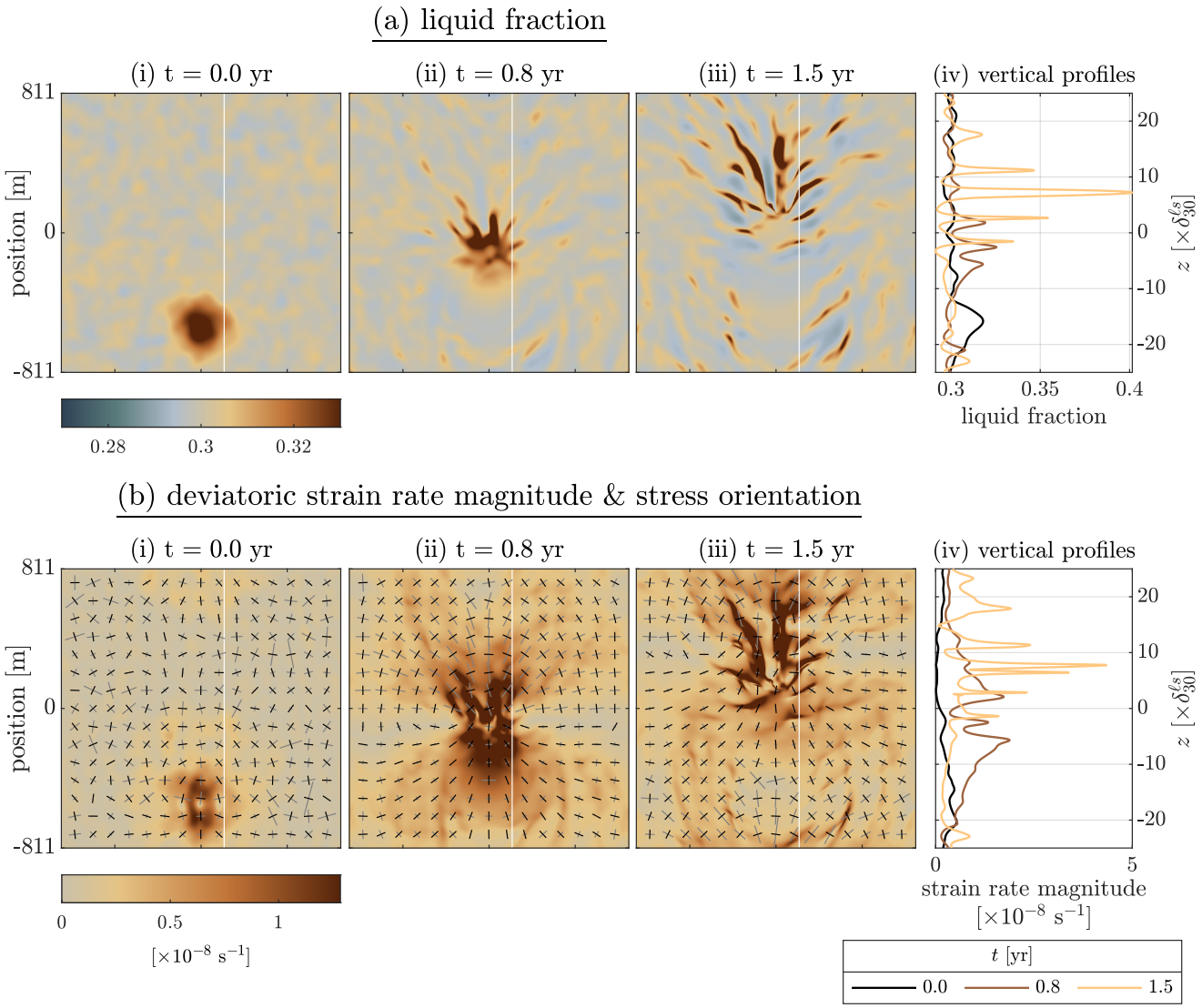

Figure 12. Simulations in the mush flow regime with a strong liquid-rich perturbation at the centre of the domain (amplitude 0.04) and with random perturbations (amplitude 0.01). The domain size is 50 times the background segregation-compaction length, and $N = 600$. (a)(i-iii) Snapshots of liquid fraction through time. The color scale is truncated to visualise the flow patterns; the maximum liquid fraction is each panel is $[0.34, 0.36, 0.43]$. White vertical lines mark the location of the profiles shown in (iv) (at $x = 134$ m), where the vertical axis is normalised to the background segregation-compaction length. (b) Background colours show the deviatoric strain rate magnitude and bars show the stress orientation of the solid phase: black bars show the least compressive stress direction (all normalised to have the same length), gray bars show the relative magnitude and direction of the greatest compressive stress. Again, the color scale is truncated and the white vertical lines mark the location of the profiles shown in (iv) at $x = 134$ m.

stress directions, and also coincide with the pattern of the incipient liquid-rich bands. This pattern persists to the last time step shown (Figure 12b(iii)), which clearly shows the near-normal relationship between localised liquid-shear bands and the least compressive stress direction. In addition, some of the liquid-shear bands start to display an isotropic stress distribution, indicating that over- or under-pressurisation of the liquid phase dominates over deviatoric stresses.

5 DISCUSSION

5.1 Bridging the porous, mush and suspension flow regimes in magmatic systems

Simulations in Section 4.1 and 4.3 demonstrate the importance of system size with respect to the emergent physical length scale of multi-phase flow. In particular, for perturbations in phase fraction to drive convective mixture flow, system size has to be at least several tens of the segregation-compaction length. Comparing the segregation-compaction length to system size can be a useful diagnostic tool for assessing the leading order dynamics expected of natural magmatic systems depending on their melt fraction and hence their classification into the porous, mush and suspension flow regimes.

In the porous flow regime, natural magmatic systems at low

melt fractions ($\phi^\ell < 0.07$) typically range from $\sim$ 10 km thick partially molten crustal regions to the $\sim$ 100 km deep melting region in the upper mantle beneath mid-ocean ridges and continental rifts or above mantle plumes. The lower end of this range is at most a few times the segregation-compaction length, which is of order $1 - 10$ km at these melt fractions; hence, we expect melt percolation accommodated by viscous compaction to dominate dynamics in most natural magmatic expressions of the porous flow regime, as previously recognised in the two-phase compaction model (McKenzie, 1984). Microstructural evidence of grain deformation and fabric development within some cumulates support the role of compaction in the crystal-rich portions of trans-crustal mush bodies (e.g., Philpotts & Philpotts, 2005; Zieg & Marsh, 2012; Bertolett et al., 2019). Only for the largest porous flow systems ($\gg$ 30 km) will mixture convection become significant. Since this scale exceeds typical crustal thicknesses, mixture convection would only be applicable to particularly deep partially molten zones beneath hot spots, which may extend further than 100 km into the upper mantle. We note, however, that thermal buoyancy is expected to be the dominant driver of large-scale mantle flow associated with plume activity, rather than lateral perturbations in partial melt content (Tackley, 2000, and references therein).

In contrast, in the suspension flow regime at high melt fractions ($\phi^\ell > 0.44$), any natural magmatic system larger than cm-scale melt veins will be orders of magnitude larger than the segregation-compaction length, which is on the scale of the mineral grain size (typically $\sim$ 1 mm). Mixture flow can thus be expected to dominate dynamics in $\sim 1-10$ m thick magma sills and dikes to $\sim 10-100$ m thick melt lenses within trans-crustal mush zones. In this limit, we can approximate the segregation-compaction length as zero and cancel terms multiplying R in (22) to recover the simplified ZSCL limit (23). This limit extends quite far into the phase space, down to $\phi^\ell \sim 0.44$ with the present coefficient calibration, meaning that a reduced suspension flow model with negligible compaction pressures applies to a substantial range of phase fractions. For sufficiently large systems ($>$ 100 m in size), the ZSCL limit may even be applied to the melt-rich end of the mush regime where the segregation-compaction length remains below 1 m. Phase segregation by hindered Stokes settling will still proceed in the suspension flow regime but at rates much slower than convective flow and thus would only have appreciable effects at impermeable domain boundaries where the segregation speed drops to zero over a short distance. Even comparatively slow crystal settling will likely lead to formation of a melt-rich layer on top and a crystal-rich cumulate pile at the base of a magma body confined within solid host rock, such as a sill.

The model thus offers a unified perspective on the emergence of melt percolation in compacting rock at low melt fraction and crystal settling from convecting magma at high melt fraction as part of a spectrum of flow dynamics that depends on the ratio R of the inherent segregation-compaction length to the natural system size. In the intervening mush regime ($\phi^\ell = 0.07 - 0.44$), a combination of phase segregation, matrix compaction, and mixture convection should appear. Moreover, we can expect strong flow localization due to the sharply contracting segregation-compaction length around the matrix disaggregation threshold. The slope with which coefficients change across the disaggregation threshold around 0.3 melt fraction is difficult to constrain from experiments. Whether this occurs smoothly across this interval in phase fraction space or more sharply at the disaggregation threshold may affect the detailed expression of non-linear behaviour in that regime. Nevertheless, the general behaviour should be robust: from $\phi^\ell \sim 0.1 - 0.3$, the segregation-compaction length contracts by at least two orders of magnitude, implying strong localisation of melt segregation and matrix shear deformation, as seen in the 2D simulation in Fig. 12.

Within a mush body, melt-rich pockets or bands, which have a locally reduced segregation-compaction length, lower effective viscosity, and lower pressure, attract more melt from the surrounding mush (Stevenson, 1989). This feedback further reduces the segregation-compaction length, allows enhanced shear deformation, and promotes mixture flow within localised pockets or bands. In the surrounding mush, melt is extracted and the segregation-compaction length increases, which stiffens the matrix and dampens both shear deformation and convective flow. Hence, the inside of melt-rich pockets or bands progresses towards the suspension regime whereas the surrounding mush progresses towards the porous regime. Ongoing melt extraction from a mush zone can bring the segregation-compaction length to a value close to or even larger than the system size. For example, in the lower boundary layer of the 1D mush column simulation (Figure 7), the last time step displays a minimum liquid fraction of 0.20 at the base of the cumulate pile. This low melt fraction corresponds to a segregation-compaction length of 1.32 km, just under half of the domain size. Under these conditions, a compacting boundary layer cannot fully develop within the domain. Compaction rates within the boundary layer may become negligible compared to typical cooling rates of crustal magma bodies. The model thus suggests that compacting adcumulates at the base of crustal magma bodies may often freeze before mature textures of compaction by grain packing can develop, and more likely before further compaction by crystal plasticity can set in. The absence of compaction textures was, for example, noted in the Skaegaard intrusion (Holness, 2018) and may indicate that the system comprised mushy cumulates close to the disaggregation threshold where the segregation-compaction length will grow considerably even for a minor decrease in melt fraction by compaction.

5.2 Melt extraction in trans-crustal magma processing systems

Results from this study help to clarify the multi-stage process of melt extraction from the mantle into the crust and to the surface. We first discuss the results as they relate to mafic systems (e.g., mid-ocean ridge, hotspot volcanism) for which our models above were calibrated. These systems are characterised by a relatively low melt viscosity (here 100 Pa s), a low wetting angle between melt and mineral grains, and an equi-dimensional shape of the dominant mineral phase, olivine. These characteristics allow permeability down to very low melt fractions (< 0.1 melt) and causes matrix disaggregation at a relatively moderate degree of melting ($0.2-0.3$ melt fraction). To frame this discussion, we distinguish between the rates of melt segregation, which is the flow of melt relative to the solid matrix at a characteristic rate of u_0^ℓ (units of m s^{-1}), and melt accumulation, which describes the progressive build-up of melt to increase melt fraction, as for example beneath a low-permeability boundary. Melt accumulation is characterised by the rate of change of melt fraction proportional to the divergence of phase segregation flux and hence should scale as $1/t_0 = u_0^\ell/\ell_0$ (20) (units s^{-1}).

At the earliest stage of magma processing, the balance between melt addition by mantle decompression melting and melt migration by porous flow accommodated by viscous matrix compaction buffers melt fractions at low values of order $\phi^\ell \sim 0.01$ (Šrámek et al., 2007; Hewitt & Fowler, 2008). Estimates for the melt segregation rates beneath mid-ocean ridges from Uranium-

series disequilibria fall on a range of 1-1000 m/yr (Elliott & Spiegelman, 2003; Rubin et al., 2005; Stracke et al., 2006; Turner & Costa, 2007; Costa et al., 2010), although a recent review by Katz et al. (2022) argues for a slightly narrower range of $10 - 100$ m/yr while recognising that some form of rheological or reactive channelling of melt percolation must be active to explain the data. Without such channelling instabilities or obstructions by a permeability barrier, melt transport would remain at low melt fractions in the porous flow regime. One important barrier against which melt will accumulate into a decompaction channel (Sparks & Parmentier, 1991) is the impermeable crystallisation front along the thermal lithosphere-asthenosphere boundary (LAB). Assuming $\ell_0 \sim 100$ km for the partially molten upper mantle beneath mid-ocean ridges or hot spots, the melt segregation rates estimated from data constraints correspond to a melt accumulation rate beneath the LAB of $\sim 10^{-4} - 10^{-3}$ yr^{-1}. With this rate, melt accumulation to form a melt-rich decompaction layer of $\phi^\ell > 0.5$ would take $\sim 500 - 5000$ years, a rather short time compared to the characteristic time of mantle flow processes that drive mantle melting.

The model presented here only accounts for diffuse porous flow without any channelling mechanisms at low melt fraction. Thus, melt segregation in the porous flow regime remains relatively slow. Our scaling analysis gives a maximum segregation rate of ~ 0.75 m/yr at $\phi^\ell \sim 0.07$, the highest melt fraction still in the porous flow regime. This is slower than the estimates from Uranium-series disequilibria and corresponds to a melt accumulation time scale of $\sim 10^5$ years for a system of $\ell_0 \sim 100$ km. However, the boundary layer simulation shows that melt accumulation to $\phi^\ell > 0.5$ takes ~ 1200 years (Figure 5), much less than half the estimated time scale from the scaling analysis and within the $\sim 500 - 5000$ year range estimated from Uranium-series disequilibria. This shorter time scale arises due to the thinning of the decompaction layer with melt accumulation. Mass balance requires that the thinning decompaction layer be compensated by melt accumulation, an effect that cannot be directly deduced from the simple scaling analysis. Thus applying the melt segregation rate derived from the scaling analysis at fixed, low melt fraction overestimates the melt accumulation time scale by almost two orders of magnitude. Melt accumulation along the LAB may be slowed by melt loss to crystallisation, a process not considered in our model. On the other hand, continued crystallisation releases latent heat and fertile chemical components, which both act to stabilise melt at lower temperatures and thermally erode the mantle lithosphere. As melt accumulates, lateral variations in melt flux can produce an undulating decompaction channel where melt focuses towards local highs, which can develop into melt-rich funnels extending further into the mantle lithosphere (Katz, 2008; England & Katz, 2010), a process that has potentially been observed by magnetotelluric imaging (Wang et al., 2020; Li et al., 2021).

With sufficient melt accumulation in the lower lithosphere, the magmatic system progresses into the mush flow regime, which is thought to be the state of large portions of crustal magmatic systems. Geophysical imaging of magmatic systems by seismic tomography and magnetotelluric studies suggests that most magma reservoirs have an average melt fraction around $0.1 - 0.4$ (Chu et al., 2010; Bai et al., 2020; Cordell et al., 2020). Due to resolution limits, these measurements represent volumetric averages of the magmatic system over length scales of several kilometers (Lees, 2007). Recent applications of seismic reflection imaging to magmatic systems, however, have detected smaller scale, stacked sill-like features with spacing on the order of hundreds of meters embedded in these kilometer-scale magma bodies, but have yet to resolve their internal melt fractions (Marjanović et al., 2014; Carbotte et al., 2020; Kim et al., 2020; Walker et al., 2021). Geologic sections of oceanic gabbros show steep, almost vertical magma fabrics containing chemical compositions that are out of equilibrium with the surrounding matrix, suggesting rapid melt extraction from the deep magmatic system through the magma mush (Coogan et al., 2000; MacLeod & Yaouancq, 2000; VanTongeren et al., 2015; Johan Lissenberg et al., 2019). Observations therefore suggest that smaller melt-rich layers or channels may emerge within larger magma mush bodies.

Simulations in this study demonstrate strong melt localisation in the mush flow regime, both against an impermeable roof as in the 1D boundary layer case (Figure 7), as well as internally within a mush body as in the 2D simulations (Figures 11, 12). Melt localisation occurs because of mechanical weakening of the solid matrix, which is distinct from the channelling instabilities arising from chemical reactions and lithological heterogeneities identified in the porous flow regime (Katz et al., 2022). Isolated, melt-rich bands appear to be the mechanically preferred organisation of mushy mafic magmatic systems, even without considering repeated cycles of magma injection followed by cooling to grow separate melt-rich regions (Annen et al., 2006; Cashman & Giordano, 2014; Jackson et al., 2018). These thin melt-rich bands develop a characteristic spacing of ~ 5 segregation-compaction lengths, as shown in Figure 12a(iv) and previously identified for localisation by non-linear viscous matrix rheology (Veveakis et al., 2014). To form stacked sills spaced $300 - 450$ m apart as observed beneath Axial Seamount for example (Carbotte et al., 2020), the segregation-compaction length of the system should be $\sim 60 - 90$ m. With the coefficient calibration used in this study, this length range offers a tight constraint on the volumetrically-averaged melt fraction of the system to be ~ 0.28, just below the disaggregation threshold in our calibration.

Melt localisation provides an efficient melt extraction mechanism. From the scaling analysis, given the melt segregation rate of ~ 60 m/yr at the disaggregation threshold ($\phi^\ell \approx 0.3$), a mush body on the order of $1 - 10$ km could produce a melt band with an accumulation rate of $6 \times 10^{-3} - 6 \times 10^{-2}$ yr^{-1}. At this rate, melt accumulation from the initial melt fraction of 0.3 to a melt-dominated decompaction layer of $\phi^\ell \approx 1$ would take $\sim 10 - 100$ years, faster than previous estimates using the compaction model in the porous flow limit. The 1D boundary layer simulation in the mush regime (Figure 7) shows that the early melt accumulation rate against a permeability barrier can be still faster. A pure melt layer emerges at only 0.08 years (31 days) , but it is very thin, because the local segregation-compaction length has decreased by four orders of magnitude from 32 m at $\phi^\ell = 0.3$ to 5 mm (the solid grain size) at $\phi^\ell > 0.58$. Again, this thin melt layer develops due to mass balance between thin decompaction layers compared to much thicker compaction layers. Once a thin, pure melt layer has formed, however, its growth is limited by melt segregation from the region just below, which prevents large melt-rich regions from growing on the extremely short time scale of days to months. The melt layer in our mush column simulation grows by 40 m/yr, close to the melt segregation rate at the background melt fraction. This rate quantifies the growth of pure melt regions and gives a time scale more representative of the growth of sizeable melt layers that is not fully captured by the melt accumulation time scale. This growth rate is almost linear with time, thus we can use this value to estimate the time scale to form pure melt layers of ~ 100 m thick to be ~ 3 years. We note that additional simulations on larger domains show the same growth rate of the melt layer, demonstrating that this growth rate does not depend on domain size as long as the

domain is large enough to span multiple segregation-compaction lengths at the background phase proportions. This size condition is easily satisfied for natural systems in the mush flow regime because segregation-compaction lengths are typically $\sim 1-2$ orders of magnitude less than magmatic mush columns estimated to range from $1-10$ km (e.g. Hildreth & Wilson, 2007; Cashman et al., 2017). Both the time of first emergence of a pure melt layer (order of days to months) and the time scale of segregation-limited growth (order of years to decades) are short compared to the expected life time (10^4 years or more) of a stacked sill complex in a magmatic mush body. Cooling and crystallisation are not likely to greatly slow down melt accumulation, because the cooling time scale is three orders of magnitude less, at ~ 4000 years for a 500 m thick sill with a thermal diffusivity of 5×10^{-7} m^2/s (following Annen, 2011). Furthermore, large, long-lived magmatic systems can establish heated contact aureoles in the crust that reduce heat loss and buffer the temperature of the system. Melt localisation in the mush regime thus provides a robust mechanism to generate ephemeral melt lenses within spatially extensive mush bodies over a short timescale relative to the expected lifetime of a crustal-scale magma body.

Growth of melt-rich bands increases their buoyancy relative to the crystal-rich mush and can potentially trigger convective overturn of the mush or diapiric rise of melt-rich pockets, both of which enhance transport of melt-rich magma towards the roof of an extensive mush column. Diapiric rise of a melt-rich pocket will be governed by Stokes flow and will occur at a rate $\sim \Delta\bar{\rho}_0 g_0 \ell_0^2/\bar{\eta}$. For a melt-rich pocket on the order of $\ell_0 \sim 10-100$ m in a mush at the disaggregation threshold where the effective viscosity is $\bar{\eta} \sim 10^{12}$ Pa s, the ascent rate is $\sim 10-1000$ m/yr which brackets the melt segregation rate of 60 m/yr. At the lower end of this range, smaller melt-rich pockets ascend slower than the melt segregation rate and therefore continue to accumulate melt. However, once they reach a critical size ($\sim$ 18 m for a mush at the disaggregation threshold), the diapiric ascent rate will exceed the melt segregation rate, promoting the rise of the melt-rich pocket without further accumulating melt from the surrounding mush. This competition should select for a critical maximum size of the melt-rich pockets where the crossover from melt accumulation to diapiric ascent occurs. Due to the dependence of melt segregation rate and mush effective viscosity on the background phase proportion, the critical maximum size should also be controlled by the mush phase proportion. As the melt-rich band grows, it can absorb smaller bands within a few segregation-compaction lengths of itself due to viscous compaction, enabling the growth and faster ascent of the largest and fastest growing ones, as observed in Figure 12. The above estimates apply for a mush of volumetrically-averaged melt fraction of 0.3, but a mush with a higher melt fraction can have a still lower effective viscosity by orders of magnitude, further facilitating the rapid ascent of melt-rich pockets at even smaller scales. Rising melt diapirs will stall against the roof of the mush body, potentially enhancing the growth rate of the melt-rich decompaction layer there. Melt accumulation will persist until this melt-rich boundary layer is buoyant enough for diapiric ascent through the stiffer overlying crust, pressurised enough to create fracture pathways for melt extraction (Keller et al., 2013), or the mush body freezes into a plutonic rock complex.

While the above discussion relies on model results calibrated to mafic systems, we expect that the emergent behaviour applies to systems of any composition, with some modification of rate and length scales due to differences in phase rheology and connectivity and consequent shifts in regime transitions across phase space. To address the longstanding question of how silicic mush bodies assemble enough melt for large eruptions within geologically short times, we next consider how our results extend to silicic systems. Extending previous compaction and hindered settling end-member models to the mush regime yields melt accumulation rates that are far too slow to generate melt lenses of $\sim 10-1000$ km^3 on the timescale of years to decades indicated by observations, even after accounting for additional energy inputs to drive melt segregation (Bachmann & Huber, 2019). With our model defined across the mush regime, we can now develop improved estimates of the melt accumulation time scales in silicic mush bodies, although we acknowledge that specialised material calibrations are needed to validate these estimates.

To represent a silicic magma, we consider a mixture comprising mostly plagioclase and dacitic to rhyolitic melt. For these materials, we alter the coefficient calibration in two ways. First, the pure-phase viscosity of the solid phase is reduced to 10^{16} Pa s, while that of the liquid phase is increased to 10^5 Pa s, considering that silicic melts are typically 3–5 orders of magnitude more viscous than basalts (Giordano et al., 2008). Second, the elongate shape of plagioclase crystals would likely shift the disaggregation threshold to higher liquid fractions; hence, we increase the disaggregation threshold from $\phi^\ell = 0.3$ to 0.5 but otherwise retain the same phase connectivity relationships. We do not expect a change in the percolation threshold as olivine-basalt and plagioclase-rhyolite have approximately the same dihedral angles (Holness, 2006). Moreover, a slight shift of the percolation threshold would be immaterial since porous flow at low melt fractions will be very slow due to the high melt viscosity.

The segregation-compaction length and velocity scales resulting from the silicic coefficient calibration show a similar shape to the coefficient model calibrated to the olivine-basalt system, but with different magnitudes and with the mush-to-suspension regime boundary shifted to higher liquid fraction (Figure 13a). Since the same percolation threshold is used, the maximum segregation-compaction length occurs at the same melt fraction of 0.07 but has a much smaller value (51 m in the silicic system vs 3.4 km in the mafic system). This suggests that viscous compaction can become appreciable on a much smaller length scale in the porous flow regime. Furthermore, mixture convection can be initiated on relatively small length scales, on the order of a 100 m, to enhance the ascent of buoyant melt-rich regions, as shown by the generally higher mixture velocity at 100 m compared to liquid segregation velocity (Figure 13b, for a region with 1% higher melt fraction). The liquid segregation velocity is mostly between 2 to 3 orders of magnitude less than the mafic system, thus we expect melt accumulation time scales to be extended.

To facilitate comparison with previous estimates of accumulation time scales from existing compaction and hindered settling end-member models, we apply approximately the same parameters as Bachmann & Bergantz (2004), considering a silicic system with a solid fraction of 0.5. This phase proportion lies just below the mush to suspension flow regime transition in our silicic calibration. We estimate the time scale to assemble 500 km^3 of rhyolitic melt from a system of characteristic horizontal area ~ 1000 km^2 (e.g., a large caldera size), which corresponds to the generation of a 0.5 km thick melt layer. Our scaling analysis gives a melt segregation rate of 1.6 m/yr at a solid fraction of 0.5. From the boundary layer simulation results, we showed that applying this fixed segregation rate to the melt accumulation rate overestimates the time of first emergence of a pure melt layer, because the contracting segregation-compaction length accelerates melt accumulation. However, once

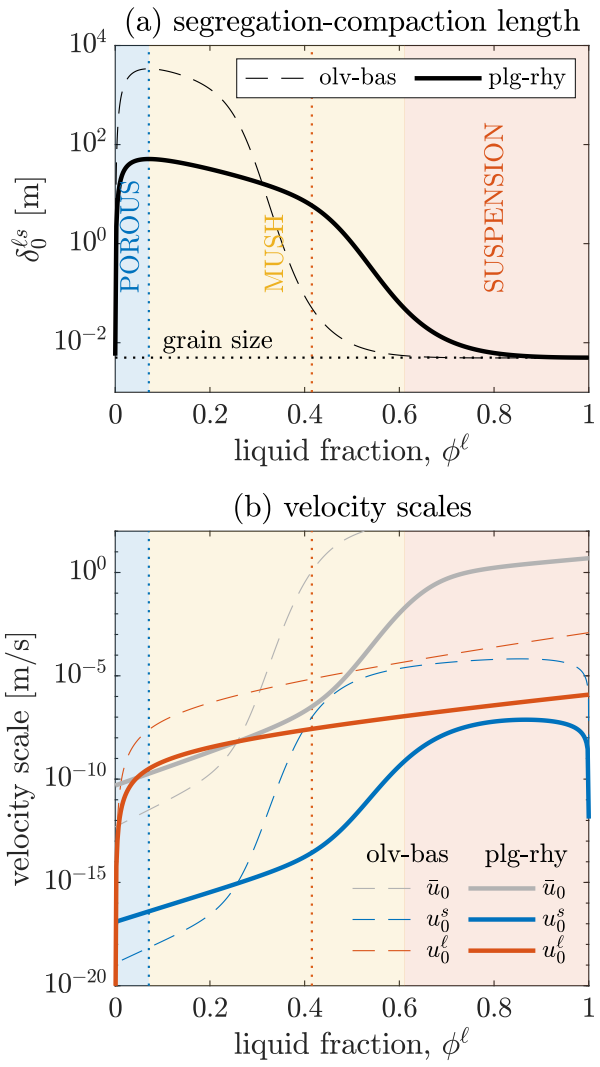

Figure 13. Scales for the silicic plagioclase-rhyolite coefficient calibration (solid lines), compared to the olivine-basalt calibration (dashed lines). (a) Segregation-compaction length $\delta_0^{\ell s}$. Shaded colours show shifted flow regimes for the plagioclase-rhyolite mixture. Vertical dotted lines show the regime boundaries for the olivine-basalt calibration. (b) Scales of the mixture and segregation velocities for both calibrations. The mixture velocity is calculated for a 1% melt perturbation region of a characteristic size of 100 m.

the thin, pure melt layer emerges, subsequent growth to obtain a sizeable pure melt layer is still segregation-limited, therefore we can approximate the melt layer growth rate using the melt segregation rate. Growing a melt layer to 0.5 km requires a time scale of 310 years, much less than the 10^4 to 10^6 years estimated in Bachmann & Bergantz (2004). Mixture convection and diapiric ascent of emergent melt pockets can further enhance melt accumulation. For diapiric ascent rates of melt-rich bands to exceed melt segregation gives a critical melt band size of only 0.72 m, very small compared to the size of a typical melt body. This suggests that diapiric ascent of melt-rich lenses will be an important process once melts accumulate. Upwelling melt-rich regions will stall and accumulate against the roof of the mush body where melt can be assembled. Mush flow dynamics arising from our unified model can therefore explain how large volumes of melt can be assembled to feed large silicic eruptions where previous estimates based on end-member models failed.

5.3 Model limitations

The model results, scaling analysis, and interpretation presented above must be understood in the context of a number of limitations on the underlying model. Model limitations arise both as consequences of omitted physical and chemical complexities, as well as from concessions to numerical and computational restrictions. In the preceding section, we have already addressed the impact of omitting all thermo-chemical processes. Cooling and crystallization is unlikely to have a major effect on estimated rates and time scales because it occurs on an order of magnitude longer time scale. Chemical reactions that change phase proportions and material properties may impact flow dynamics, for example driving the reaction infiltration instability that facilitates channelisation in the porous flow regime. Coupling multi-phase transport to thermo-chemical evolution remains one of the primary challenges in modelling igneous processes (Katz et al., 2022) but promises to predict observable petrological and geochemical signatures diagnostic of the mechanical processes described here.

While we have considered only a two-phase system in this study, the presence of a magmatic volatile phase (MVP) will likely affect melt segregation rates, although the impact of the MVP remains unclear. On one hand, the MVP may enhance melt segregation through the gas-driven filter pressing mechanism: exsolving MVP pressurizes the crystal matrix and expels melt to relieve pressure (Sisson & Bacon, 1999). On the other hand, the MVP may hinder melt segregation: at intermediate crystal fractions of 0.65, the low density and much lower viscosity of the MVP relative to other phases can promote rapid MVP segregation accommodated by the collective compaction of the melt-crystal matrix (Huber & Parmigiani, 2018). Consequently, melt-crystal segregation would only become appreciable after the MVP is segregated from the mixture. The large viscosity contrasts in three-phase magma mixtures make both numerical realisations and experimental investigations highly challenging. The theory in Keller & Suckale (2019) was extended to hypothesise a flow regime diagram for three-phase magmas, but initial tests using the code developed here show some numerical challenges in resolving the gas-liquid segregation-compaction length which can be orders of magnitude smaller than its liquid-solid equivalent at the same phase fractions. Moreover, only a few three-phase experiments exist to calibrate models (e.g., Islam et al., 2014; Oppenheimer et al., 2015), although recent advances in *in-situ* imaging may offer new insights into three-phase connectivity (e.g., Pistone et al., 2015; Dobson et al., 2020; Pistone et al., 2022).

In this study we consider relatively simple material properties, including constant phase densities, linear viscous phase rheologies, and isotropic transport coefficients. In magmatic systems, the liquid and solid phases are well-approximated as incompressible with pressure, but their densities can have small variations with temperature and larger variations with chemical composition. However, since we do not include evolving temperature and composition in the model, there is no internally consistent way to evolve phase densities here. For the same reason, we employ constant phase viscosities and do not include known thermal and compositional effects on silicate rheology, nor any non-Newtonian behaviour. Nevertheless, the linear viscous phase rheology is able to facilitate melt-shear localisation through melt-weakening of effective mixture viscosity following from our phenomenological description of local-scale phase topology. Note that despite some similarity in re-

sulting melt-shear bands (e.g., Katz et al., 2006), our coefficient model does not contain the shear-thinning rheology. In more complex models with non-Newtonian magma viscosity, visco-elastic or brittle-plastic rheology, melt and coinciding shear localisation may become more pronounced, or even transition to melt transport in tensile fractures (Keller et al., 2013). Furthermore, our transport coefficients ($K^i_\phi, K^i_v, C^i_\phi, C^i_v$) are assumed to be scalar functions of pure-phase properties, phase fractions and a phenomenological representation of phase topology. However, phase topology is known to develop anisotropy, for example in crystal-rich systems where the crystallographic axes of grains develop preferred orientations. Previous work found that anisotropy in matrix viscosity promotes melt segregation and further affects the growth rate and orientation angle of melt-rich bands in stress-driven flows (Takei & Katz, 2013; Katz & Takei, 2013; Takei & Katz, 2015). Accounting for anisotropy would require the transport coefficients to be expressed as tensors rather than scalars, a considerable increase in model complexity and rheological model parameters.

With respect to computational aspects, while the model applies across all phase fractions and flow regimes, the time and length scales on which the model can robustly and efficiently operate are limited. First, the numerical model was developed to study dynamics around $R \sim 1$ to understand the interplay between phase segregation and mixture flow. The domain size is consequently chosen relative to the dominant segregation-compaction length at the specified phase fraction, and the resulting numerical time steps are restricted to the ratio of the segregation-compaction length to segregation speed. The model is not well-suited to study flow scenarios outside these length and time scales, for example the suspension flow regime on scales larger than kilometers and longer than centuries, as might arise, for example, in very large igneous intrusions or during the magma ocean stage of planetary formation. For such systems, a simplified model applying the ZSCL limit would be more appropriate as it would not need to resolve the very small segregation-compaction length on the numerical grid.

Second, the wide range of segregation-compaction lengths does not permit a single simulation to cover the porous flow to suspension flow regimes while sufficiently resolving segregation and compaction processes in all regimes. For the coefficient calibration chosen in this study, the segregation-compaction length spans 6 orders of magnitude, from the solid grain size of 5 mm to the maximum of 3.4 km at low liquid fraction. Since at least a few grid cells are required to resolve each segregation-compaction length, it is not practically possible to model the system on a domain spanning the largest inherent length while resolving the smallest length on the numerical grid with (for example, resolving 10 km domain with 1 mm grid step requires 10^7 grid cells). Rather, as we demonstrate in Section 4.1, specific model dimensions should be chosen around the phase fractions of interest. The presented model is useful for exploring the dynamic flow regimes given a system length scale, which in turn informs the formulation of reduced equations valid only for specific flow regimes. The problem of scales is most pronounced in the mush regime, where effective transport properties and segregation-compaction lengths span many orders of magnitude over a small range of phase fractions. In this study, we use means of numerical stabilisation to moderate the relative contrast of the segregation-compaction length across the domain. In natural systems, the rheological weakening across the disaggregation threshold may well be sharper than our model can robustly reproduce. Hence it is possible that localisation of melt-rich bands in natural systems is more pronounced than in our models, perhaps to the point where melt-rich bands contract down to the solid grain scale. Such narrowly localised melt bands may then appear as thin, stress-aligned veins, a type of structure frequently observed in plutonic rocks. These would be distinct from veins resulting from hydro-fracturing in that no brittle failure of mineral grains on their boundaries would be observed.

Third, we recognise that the continuum assumption cannot be applied in the volume-averaging sense in the suspension flow regime. With the segregation-compaction length reduced to the solid grain size and the requirement that each segregation-compaction length be resolved by several grid cells, the discrete grid spacing is required to be below the solid grain size. The governing equations remain valid in this regime if we instead consider the model in terms of ensemble averaging. Instead of requiring that each grid cell correspond to a representative volume element comprising a large number of microscopic phase constituents, the ensemble averaging interpretation understands continuum fields to represent the ensemble average of many realisations of microscopic phase topologies (Drew & Passman, 1999; Oliveira et al., 2018). Hence, the requirement that discrete grid cells correspond to a sufficiently large representative volume element is not a necessary condition on the validity of the continuum approach. The agreement between simulations and existing endmember models (Section 4.2.2) confirms that our new model produces the expected dynamic behavior. Future comparisons with direct numerical simulations that resolve phase interactions at the granular scale (e.g. Qin & Suckale, 2017; Culha et al., 2020) may provide a way to further validate the results in this regime.

6 CONCLUSION

In this study, we have examined the mechanical evolution of a solid-liquid mixture across porous, mush, and suspension flow regimes using a unified numerical modelling approach based on the theory of Keller & Suckale (2019). Scaling analysis of the governing equations reveals an inherent length scale for phase segregation and compaction which is a generalisation of the compaction length derived from porous two-phase flow models, and which can be used to designate flow regime boundaries. By explaining emergent dynamics in relation to the inherent segregation-compaction length, the model connects previously disparate endmember models of porous and suspension flows in two-phase mixtures and elucidates the transitional mush regime for which no dedicated mechanical model had previously been formulated.

Using our numerical model, we recover well-known solutions in solid- and liquid-rich endmember regimes and further characterise the dynamics in both regimes. Rank-ordered porosity waves with a consistent, positive amplitude-speed relationship emerge in the porous flow regime, whereas shock-rarefaction waves emerge in suspension flows. In confined magmatic systems, asymmetric compaction and decompaction layers form at the bottom and top of the domain respectively because of the variation in segregation-compaction length with evolving phase fractions.

The numerical results substantiate our scaling analysis, demonstrating that the derived scales appropriately represent the characteristic flow dynamics. We find that phase segregation dominates dynamics in small systems ($R \approx 1$) while mixture flow dominates dynamics in larger ones ($R \approx 0.1$). In the porous flow regime, phase segregation promotes the formation of approximately horizontal layers of increasing concentration, similar to the formation of 1D porosity wavetrains. In the suspension flow regime, phase segregation promotes the formation of concentration waves with

steepening shock fronts, consistent with the 1D idealised case. The mush flow regime appears similar to the porous flow case, albeit with much thinner melt bands due to the contracting segregation-compaction length with increasing liquid fraction. In all the flow regimes, liquid localisation is less prominent in larger systems due to strong mixture flow.

Further simulations in the mush regime show that melt-rich bands form approximately normal to the least compressive principal stress. These bands may form within few years, which is short relative to the expected lifetime of a magma mush body. This suggests that ephemeral pockets of melt-rich magma may well be a mechanically favourable configuration in crustal mush bodies. Comparing with natural systems shows that the mush regime predicts melt accumulation times that are fast enough to explain observed stacked sill features in mafic systems, as well as the relatively rapid assembly of melt-rich magma for large volume eruptions in silicic systems.

ACKNOWLEDGMENTS

Y.Q. Wong was funded by the European Union's Horizon 2020 research and innovation programme under the Marie Skłodowska-Curie Action grant agreement number 894897 (project acronym DEFORM).

DATA AVAILABILITY

The MATLAB software package to run the multi-phase mechanical model are available and regularly updated at `https://github.com/kellertobs/pantarhei.git`. The specific release accompanying this paper, as well as scripts to run models and produce the figures can be found at `https://doi.org/10.5281/zenodo.6453803`.

References

Aharonov, E., Whitehead, J. A., Kelemen, P. B., & Spiegelman, M., 1995. Channeling instability of upwelling melt in the mantle, *Journal of Geophysical Research: Solid Earth*, **100**(B10), 20433–20450.

Annen, C., 2011. Implications of incremental emplacement of magma bodies for magma differentiation, thermal aureole dimensions and plutonism-volcanism relationships, *Tectonophysics*, **500**(1-4), 3–10.

Annen, C. J., Blundy, J. D., & Sparks, R. S., 2006. The Genesis of Intermediate and Silicic Magmas in Deep Crustal Hot Zones, *Journal of Petrology*, **47**(3), 505–539.

Bachmann, O. & Bergantz, G., 2008. The Magma Reservoirs That Feed Supereruptions, *Elements*, **4**(1), 17–21.

Bachmann, O. & Bergantz, G. W., 2004. On the Origin of Crystal-poor Rhyolites: Extracted from Batholithic Crystal Mushes, *Journal of Petrology*, **45**(8), 1565–1582.

Bachmann, O. & Huber, C., 2019. The Inner Workings of Crustal Distillation Columns; The Physical Mechanisms and Rates Controlling Phase Separation in Silicic Magma Reservoirs, *Journal of Petrology*, **60**(1), 3–18.

Bachmann, O., Dungan, M. A., & Lipman, P. W., 2002. The Fish Canyon Magma Body, San Juan Volcanic Field, Colorado: Rejuvenation and Eruption of an Upper-Crustal Batholith, *Journal of Petrology*, **43**(8), 1469–1503.

Bai, T., Thurber, C., Lanza, F., Singer, B. S., Bennington, N., Keranen, K., & Cardona, C., 2020. Teleseismic Tomography of the Laguna del Maule Volcanic Field in Chile, *Journal of Geophysical Research: Solid Earth*, **125**(8), e2020JB019449.

Barcilon, V. & Richter, F. M., 1986. Nonlinear waves in compacting media, *Journal of Fluid Mechanics*, **164**, 429–448.

Bercovici, D., Ricard, Y., & Schubert, G., 2001. A two-phase model for compaction and damage 1. General Theory, *Journal of Geophysical Research: Solid Earth*, **106**(B5), 8887–8906.

Berlo, K., Blundy, J., Turner, S., & Hawkesworth, C., 2007. Textural and chemical variation in plagioclase phenocrysts from the 1980 eruptions of Mount St. Helens, USA, *Contributions to Mineralogy and Petrology*, **154**(3), 291–308.

Bertolett, E., Prior, D., Gravley, D., Hampton, S., & Kennedy, B., 2019. Compacted cumulates revealed by electron backscatter diffraction analysis of plutonic lithics, *Geology*, **47**(5), 445–448.

Brandeis, G. & Jaupart, C., 1986. On the interaction between convection and crystallization in cooling magma chambers, *Earth and Planetary Science Letters*, **77**(3-4), 345–361.

Brown, S., Wilson, C., Cole, J., & Wooden, J., 1998. The Whakamaru group ignimbrites, Taupo Volcanic Zone, New Zealand: evidence for reverse tapping of a zoned silicic magmatic system, *Journal of Volcanology and Geothermal Research*, **84**(1-2), 1–37.

Carbotte, S. M., Arnulf, A., Spiegelman, M., Lee, M., Harding, A., Kent, G., Canales, J. P., & Nedimović, M., 2020. Stacked sills forming a deep melt-mush feeder conduit beneath Axial Seamount, *Geology*, **48**(7), 693–697.

Cashman, K. & Blundy, J., 2013. Petrological cannibalism: the chemical and textural consequences of incremental magma body growth, *Contributions to Mineralogy and Petrology*, **166**(3), 703–729.

Cashman, K. V. & Giordano, G., 2014. Calderas and magma reservoirs, *Journal of Volcanology and Geothermal Research*, **288**, 28–45.

Cashman, K. V., Sparks, R. S. J., & Blundy, J. D., 2017. Vertically extensive and unstable magmatic systems: A unified view of igneous processes, *Science*, **355**(6331).

Chu, R., Helmberger, D. V., Sun, D., Jackson, J. M., & Zhu, L., 2010. Mushy magma beneath Yellowstone, *Geophysical Research Letters*, **37**(1), n/a–n/a.

Coogan, L. A., Saunders, A. D., Kempton, P. D., & Norry, M. J., 2000. Evidence from oceanic gabbros for porous melt migration within a crystal mush beneath the Mid-Atlantic Ridge, *Geochemistry, Geophysics, Geosystems*, **1**(9), n/a–n/a.

Cooper, K. M. & Kent, A. J. R., 2014. Rapid remobilization of magmatic crystals kept in cold storage, *Nature*, **506**(7489), 480–483.

Cordell, D., Unsworth, M. J., Lee, B., Díaz, D., Bennington, N. L., & Thurber, C. H., 2020. Integrating Magnetotelluric and Seismic Images of Silicic Magma Systems: A Case Study From the Laguna del Maule Volcanic Field, Central Chile, *Journal of Geophysical Research: Solid Earth*, **125**(11), 1–21.

Costa, F., Coogan, L. A., & Chakraborty, S., 2010. The time scales of magma mixing and mingling involving primitive melts and melt–mush interaction at mid-ocean ridges, *Contributions to Mineralogy and Petrology*, **159**(3), 371–387.

Culha, C., Suckale, J., Keller, T., & Qin, Z., 2020. Crystal Fractionation by Crystal-Driven Convection, *Geophysical Research Letters*, **47**(4), 1–9.

Dobson, K. J., Allabar, A., Bretagne, E., Coumans, J., Cassidy, M., Cimarelli, C., Coats, R., Connolley, T., Courtois, L., Ding-

well, D. B., Di Genova, D., Fernando, B., Fife, J. L., Fyfe, F., Gehne, S., Jones, T., Kendrick, J. E., Kinvig, H., Kolzenburg, S., Lavallée, Y., Liu, E., Llewellin, E. W., Madden-Nadeau, A., Madi, K., Marone, F., Morgan, C., Oppenheimer, J., Ploszajski, A., Reid, G., Schauroth, J., Schlepütz, C. M., Sellick, C., Vasseur, J., von Aulock, F. W., Wadsworth, F. B., Wiesmaier, S., & Wanelik, K., 2020. Quantifying Microstructural Evolution in Moving Magma, *Frontiers in Earth Science*, **8**, 287.

Drew, D. A. & Passman, S. L., 1999. *Theory of Multicomponent Fluids*, vol. 135 of **Applied Mathematical Sciences**, Springer New York, New York, NY.

Druitt, T. H., Costa, F., Deloule, E., Dungan, M., & Scaillet, B., 2012. Decadal to monthly timescales of magma transfer and reservoir growth at a caldera volcano, *Nature*, **482**(7383), 77–80.

Dufek, J. & Bachmann, O., 2010. Quantum magmatism: Magmatic compositional gaps generated by melt-crystal dynamics, *Geology*, **38**(8), 687–690.

Edmonds, M., Cashman, K. V., Holness, M., & Jackson, M., 2019. Architecture and dynamics of magma reservoirs, *Philosophical Transactions of the Royal Society A: Mathematical, Physical and Engineering Sciences*, **377**(2139).

Elliott, T. & Spiegelman, M., 2003. Melt Migration in Oceanic Crustal Production: A U-series Perspective, in *Treatise on Geochemistry*, vol. 3-9, pp. 465–510, Elsevier.

England, P. C. & Katz, R. F., 2010. Melting above the anhydrous solidus controls the location of volcanic arcs, *Nature*, **467**(7316), 700–703.

Gerya, T., 2019. *Introduction to Numerical Geodynamic Modelling*, Cambridge University Press, 2nd edn.

Giordano, D., Russell, J. K., & Dingwell, D. B., 2008. Viscosity of magmatic liquids: A model, *Earth and Planetary Science Letters*, **271**(1-4), 123–134.

Hewitt, I. & Fowler, A., 2008. Partial melting in an upwelling mantle column, *Proceedings of the Royal Society A: Mathematical, Physical and Engineering Sciences*, **464**(2097), 2467–2491.

Hildreth, W. & Fierstein, J., 2000. Katmai volcanic cluster and the great eruption of 1912, *Geological Society of America Bulletin*, **112**(10), 1594–1620.

Hildreth, W. & Wilson, C. J. N., 2007. Compositional Zoning of the Bishop Tuff, *Journal of Petrology*, **48**(5), 951–999.

Hirth, G. & Kohlstedt, D. L., 2003. Rheology of the Upper Mantle and the Mantle Wedge: a View From the Experimentalists BT - Geophysical Monograph Series, *Geophysical Monograph Series*, **138**, 83–106.

Holness, M. B., 2006. Melt–Solid Dihedral Angles of Common Minerals in Natural Rocks, *Journal of Petrology*, **47**(4), 791–800.

Holness, M. B., 2018. Melt segregation from silicic crystal mushes: a critical appraisal of possible mechanisms and their microstructural record, *Contributions to Mineralogy and Petrology*, **173**(6), 48.

Holness, M. B., Vukmanovic, Z., & Mariani, E., 2017. Assessing the Role of Compaction in the Formation of Adcumulates: a Microstructural Perspective, *Journal of Petrology*, **58**(4), 643–673.

Holtzman, B. K., Groebner, N. J., Zimmerman, M. E., Ginsberg, S. B., & Kohlstedt, D. L., 2003. Stress-driven melt segregation in partially molten rocks, *Geochemistry, Geophysics, Geosystems*, **4**(5), n/a–n/a.

Huber, C. & Parmigiani, A., 2018. A Physical Model for Three-Phase Compaction in Silicic Magma Reservoirs, *Journal of Geophysical Research: Solid Earth*, **123**(4), 2685–2705.

Huber, C., Bachmann, O., & Manga, M., 2009. Homogenization processes in silicic magma chambers by stirring and mushification (latent heat buffering), *Earth and Planetary Science Letters*, **283**(1), 38–47.

Islam, A., Chevalier, S., Ben Salem, I., Bernabe, Y., Juanes, R., & Sassi, M., 2014. Characterization of the crossover from capillary invasion to viscous fingering to fracturing during drainage in a vertical 2D porous medium, *International Journal of Multiphase Flow*, **58**, 279–291.

Jackson, M. D., Blundy, J., & Sparks, R. S., 2018. Chemical differentiation, cold storage and remobilization of magma in the Earth's crust, *Nature*, **564**(7736), 405–409.

Johan Lissenberg, C., MacLeod, C. J., & Bennett, E. N., 2019. Consequences of a crystal mush-dominated magma plumbing system: A mid-ocean ridge perspective, *Philosophical Transactions of the Royal Society A: Mathematical, Physical and Engineering Sciences*, **377**(2139).

Katz, R. F., 2008. Magma Dynamics with the Enthalpy Method: Benchmark Solutions and Magmatic Focusing at Mid-ocean Ridges, *Journal of Petrology*, **49**(12), 2099–2121.

Katz, R. F., 2022. *The dynamics of partially molten rock*, Princeton University Press.

Katz, R. F. & Takei, Y., 2013. Consequences of viscous anisotropy in a deforming, two-phase aggregate. Part 2. Numerical solutions of the full equations, *Journal of Fluid Mechanics*, **734**, 456–485.

Katz, R. F., Spiegelman, M., & Holtzman, B., 2006. The dynamics of melt and shear localization in partially molten aggregates, *Nature*, **442**(7103), 676–679.

Katz, R. F., Jones, D. W. R., Rudge, J. F., & Keller, T., 2022. Physics of Melt Extraction from the Mantle: Speed and Style, *Annual Review of Earth and Planetary Sciences*, **50**(1).

Kelemen, P. B., Whitehead, J. A., Aharonov, E., & Jordahl, K. A., 1995. Experiments on flow focusing in soluble porous media, with applications to melt extraction from the mantle, *Journal of Geophysical Research: Solid Earth*, **100**(B1), 475–496.

Keller, T. & Katz, R. F., 2016. The role of volatiles in reactive melt transport in the asthenosphere, *Journal of Petrology*, **57**(6), 1073–1108.

Keller, T. & Suckale, J., 2019. A continuum model of multi-phase reactive transport in igneous systems, *Geophysical Journal International*, **219**(1), 185–222.

Keller, T., May, D. A., & Kaus, B. J., 2013. Numerical modelling of magma dynamics coupled to tectonic deformation of lithosphere and crust, *Geophysical Journal International*, **195**(3), 1406–1442.

Kilgour, G., Blundy, J., Cashman, K., & Mader, H. M., 2013. Small volume andesite magmas and melt–mush interactions at Ruapehu, New Zealand: evidence from melt inclusions, *Contributions to Mineralogy and Petrology*, **166**(2), 371–392.

Kim, D., Brown, L. D., Árnason, K., Gudmundsson, , Ágústsson, K., & Flóvenz, G., 2020. Magma "bright spots" mapped beneath Krafla, Iceland, using RVSP imaging of reflected waves from microearthquakes, *Journal of Volcanology and Geothermal Research*, **391**, 106365.

Lees, J. M., 2007. Seismic tomography of magmatic systems, *Journal of Volcanology and Geothermal Research*, **167**(1-4), 37–56.

Li, Y., Weng, A., Xu, W., Zou, Z., Tang, Y., Zhou, Z., Li, S., Zhang, Y., & Ventura, G., 2021. Translithospheric magma plumbing system of intraplate volcanoes as revealed by electrical resistivity imaging, *Geology*, **49**(11), 1337–1342.

Lipman, P., Dungan, M., & Bachmann, O., 1997. Comagmatic

granophyric granite in the Fish Canyon Tuff, Colorado: Implications for magma-chamber processes during a large ash-flow eruption, *Geology*, **25**(10), 915.

Longo, A., Vassalli, M., Papale, P., & Barsanti, M., 2006. Numerical simulation of convection and mixing in magma chambers replenished with CO 2 -rich magma, *Geophysical Research Letters*, **33**(21), L21305.

MacLeod, C. & Yaouancq, G., 2000. A fossil melt lens in the Oman ophiolite: Implications for magma chamber processes at fast spreading ridges, *Earth and Planetary Science Letters*, **176**(3-4), 357–373.

Manga, M., 1996. Waves of bubbles in basaltic magmas and lavas, *Journal of Geophysical Research: Solid Earth*, **101**(B8), 17457–17465.

Marjanović, M., Carbotte, S. M., Carton, H., Nedimović, M. R., Mutter, J. C., & Canales, J. P., 2014. A multi-sill magma plumbing system beneath the axis of the East Pacific Rise, *Nature Geoscience*, **7**(11), 825–829.

Martin, D. & Nokes, R., 1988. Crystal settling in a vigorously convecting magma chamber, *Nature*, **332**(6164), 534–536.

McKenzie, D., 1984. The generation and compaction of partially molten rock, *Journal of Petrology*, **25**(3), 713–765.

Mucha, P. J., Tee, S.-Y., Weitz, D. A., Shraiman, B. I., & Brenner, M. P., 2004. A model for velocity fluctuations in sedimentation, *Journal of Fluid Mechanics*, **501**, 71–104.

Oliveira, B., Afonso, J. C., Zlotnik, S., & Diez, P., 2018. Numerical modelling of multiphase multicomponent reactive transport in the Earth's interior, *Geophysical Journal International*, **212**(1), 345–388.

Oppenheimer, J., Rust, A. C., Cashman, K. V., & Sandnes, B., 2015. Gas migration regimes and outgassing in particle-rich suspensions, *Frontiers in Physics*, **3**(August), 1–13.

Paulatto, M., Moorkamp, M., Hautmann, S., Hooft, E., Morgan, J. V., & Sparks, R. S. J., 2019. Vertically Extensive Magma Reservoir Revealed From Joint Inversion and Quantitative Interpretation of Seismic and Gravity Data, *Journal of Geophysical Research: Solid Earth*, **124**(11), 11170–11191.

Philpotts, A. R. & Philpotts, D. E., 2005. Crystal-mush compaction in the Cohassett flood-basalt flow, Hanford, Washington, *Journal of Volcanology and Geothermal Research*, **145**(3-4), 192–206.

Pistone, M., Arzilli, F., Dobson, K. J., Cordonnier, B., Reusser, E., Ulmer, P., Marone, F., Whittington, A. G., Mancini, L., Fife, J. L., & Blundy, J. D., 2015. Gas-driven filter pressing in magmas: Insights into in-situ melt segregation from crystal mushes, *Geology*, **43**(8), 699–702.

Pistone, M., Formo, E., Whittington, A. G., Herbst, T., & Cottrell, E., 2022. Direct nanoscale observations of degassing-induced crystallisation in felsic magmas, *Contributions to Mineralogy and Petrology*, **177**(3), 38.

Polyak, B., 1964. Some methods of speeding up the convergence of iteration methods, *USSR Computational Mathematics and Mathematical Physics*, **4**(5), 1–17.

Qin, Z. & Suckale, J., 2017. Direct numerical simulations of gas–solid–liquid interactions in dilute fluids, *International Journal of Multiphase Flow*, **96**, 34–47.

Räss, L., Duretz, T., & Podladchikov, Y., 2019. Resolving hydromechanical coupling in two and three dimensions: spontaneous channelling of porous fluids owing to decompaction weakening, *Geophysical Journal International*, **218**(3), 1591–1616.

Rees Jones, D. W., Katz, R. F., Tian, M., & Rudge, J. F., 2018. Thermal impact of magmatism in subduction zones, *Earth and Planetary Science Letters*, **481**, 73–79.

Richter, F. M. & McKenzie, D., 1984. Dynamical Models for Melt Segregation from a Deformable Matrix, *The Journal of Geology*, **92**(6), 729–740.

Roscoe, R., 1952. The viscosity of suspensions of rigid spheres, *British Journal of Applied Physics*, **3**(8), 267–269.

Rubin, K. H., van der Zander, I., Smith, M. C., & Bergmanis, E. C., 2005. Minimum speed limit for ocean ridge magmatism from 210Pb–226Ra–230Th disequilibria, *Nature*, **437**(7058), 534–538.

Rudge, J. F., 2018. The Viscosities of Partially Molten Materials Undergoing Diffusion Creep, *Journal of Geophysical Research: Solid Earth*, **123**(12), 534–10.

Rudge, J. F., Bercovici, D., & Spiegelman, M., 2011. Disequilibrium melting of a two phase multicomponent mantle, *Geophysical Journal International*, **184**(2), 699–718.

Salari, K. & Knupp, P., 2000. Code Verification by the Method of Manufactured Solutions, Tech. rep., Sandia National Laboratories (SNL), Albuquerque, NM, and Livermore, CA.

Schmitt, A. K., Lindsay, J. M., de Silva, S., & Trumbull, R. B., 2003. U–Pb zircon chronostratigraphy of early-Pliocene ignimbrites from La Pacana, north Chile: implications for the formation of stratified magma chambers, *Journal of Volcanology and Geothermal Research*, **120**(1-2), 43–53.

Scott, D. R. & Stevenson, D. J., 1984. Magma solitons, *Geophysical Research Letters*, **11**(11), 1161–1164.

Scott, D. R. & Stevenson, D. J., 1986. Magma ascent by porous flow, *Journal of Geophysical Research*, **91**(B9), 9283.

Segrè, P. N., Liu, F., Umbanhowar, P., & Weitz, D. A., 2001. An effective gravitational temperature for sedimentation, *Nature*, **409**(6820), 594–597.

Simpson, G. & Spiegelman, M., 2011. Solitary Wave Benchmarks in Magma Dynamics, *Journal of Scientific Computing*, **49**(3), 268–290.

Sisson, T. W. & Bacon, C. R., 1999. Gas-driven filter pressing in magmas, *Geology*, **27**(7), 613–616.

Smith, V. C., Blundy, J. D., & Arce, J. L., 2009. A Temporal Record of Magma Accumulation and Evolution beneath Nevado de Toluca, Mexico, Preserved in Plagioclase Phenocrysts, *Journal of Petrology*, **50**(3), 405–426.

Snyder, D., 2000. Thermal effects of the intrusion of basaltic magma into a more silicic magma chamber and implications for eruption triggering, *Earth and Planetary Science Letters*, **175**(3-4), 257–273.

Sparks, D. W. & Parmentier, E., 1991. Melt extraction from the mantle beneath spreading centers, *Earth and Planetary Science Letters*, **105**(4), 368–377.

Sparks, R. S. J., Huppert, H. E., Turner, J. S., Sakuyama, M., & O'Hara, M. J., 1984. The fluid dynamics of evolving magma chambers, *Philosophical Transactions of the Royal Society of London. Series A, Mathematical and Physical Sciences*, **310**(1514), 511–534.

Sparks, R. S. J., Annen, C., Blundy, J. D., Cashman, K. V., Rust, A. C., & Jackson, M. D., 2019. Formation and dynamics of magma reservoirs, *Philosophical Transactions of the Royal Society A: Mathematical, Physical and Engineering Sciences*, **377**(2139).

Spiegelman, M., 1993a. Flow in deformable porous media. Part 1 Simple analysis, *Journal of Fluid Mechanics*, **247**, 17–38.

Spiegelman, M., 1993b. Flow in deformable porous media. Part 2 Numerical analysis – the relationship between shock waves and solitary waves, *Journal of Fluid Mechanics*, **247**, 39–63.

Spiegelman, M., Kelemen, P. B., & Aharonov, E., 2001. Causes and consequences of flow organization during melt transport: The reaction infiltration instability in compactible media, *Journal of Geophysical Research: Solid Earth*, **106**(B2), 2061–2077.

Šrámek, O., Ricard, Y., & Bercovici, D., 2007. Simultaneous melting and compaction in deformable two-phase media, *Geophysical Journal International*, **168**(3), 964–982.

Stevenson, D. J., 1989. Spontaneous small-scale melt segregation in partial melts undergoing deformation, *Geophysical Research Letters*, **16**(9), 1067–1070.

Stevenson, D. J. & Scott, D. R., 1991. Mechanics of Fluid-Rock Systems, *Annual Review of Fluid Mechanics*, **23**(1), 305–339.

Stracke, A., Bourdon, B., & McKenzie, D., 2006. Melt extraction in the Earth's mantle: Constraints from U–Th–Pa–Ra studies in oceanic basalts, *Earth and Planetary Science Letters*, **244**(1-2), 97–112.

Tackley, P. J., 2000. Mantle Convection and Plate Tectonics: Toward an Integrated Physical and Chemical Theory, *Science*, **288**(5473), 2002–2007.

Takei, Y. & Holtzman, B. K., 2009. Viscous constitutive relations of solid-liquid composites in terms of grain boundary contiguity: 2. Compositional model for small melt fractions, *Journal of Geophysical Research*, **114**(B6), 1–18.

Takei, Y. & Katz, R. F., 2013. Consequences of viscous anisotropy in a deforming, two-phase aggregate. Part 1. Governing equations and linearized analysis, *Journal of Fluid Mechanics*, **734**, 424–455.

Takei, Y. & Katz, R. F., 2015. Consequences of viscous anisotropy in a deforming, two-phase aggregate. Why is porosity-band angle lowered by viscous anisotropy?, *Journal of Fluid Mechanics*, **784**, 199–224.

Turner, S. & Costa, F., 2007. Measuring Timescales of Magmatic Evolution, *Elements*, **3**(4), 267–272.

VanTongeren, J., Hirth, G., & Kelemen, P., 2015. Constraints on the accretion of the gabbroic lower oceanic crust from plagioclase lattice preferred orientation in the Samail ophiolite, *Earth and Planetary Science Letters*, **427**, 249–261.

Veveakis, E., Regenauer-Lieb, K., & Weinberg, R., 2014. Ductile compaction of partially molten rocks: the effect of non-linear viscous rheology on instability and segregation, *Geophysical Journal International*, **200**(1), 519–523.

Walker, F., Schofield, N., Millett, J., Jolley, D., Holford, S., Planke, S., Jerram, D. A., & Myklebust, R., 2021. Inside the volcano: Three-dimensional magmatic architecture of a buried shield volcano, *Geology*, **49**(3), 243–247.

Wang, L. H., Yarushina, V. M., Alkhimenkov, Y., & Podladchikov, Y., 2021. Physics-inspired pseudo-transient method and its application in modelling focused fluid flow with geological complexity, *Geophysical Journal International*, **229**(1), 1–20.

Wang, S., Constable, S., Rychert, C. A., & Harmon, N., 2020. A Lithosphere-Asthenosphere Boundary and Partial Melt Estimated Using Marine Magnetotelluric Data at the Central Middle Atlantic Ridge, *Geochemistry, Geophysics, Geosystems*, **21**(9), e2020GC009177.

Weatherley, S. M. & Katz, R. F., 2012. Melting and channelized magmatic flow in chemically heterogeneous, upwelling mantle, *Geochemistry Geophysics Geosystems*, **13**(5), Q0AC18.

Wolff, J., Ellis, B., Ramos, F., Starkel, W., Boroughs, S., Olin, P., & Bachmann, O., 2015. Remelting of cumulates as a process for producing chemical zoning in silicic tuffs: A comparison of cool, wet and hot, dry rhyolitic magma systems, *Lithos*, **236-237**, 275–286.

Wotzlaw, J.-F., Bindeman, I. N., Stern, R. A., D'Abzac, F.-X., & Schaltegger, U., 2015. Rapid heterogeneous assembly of multiple magma reservoirs prior to Yellowstone supereruptions, *Scientific Reports*, **5**(1), 14026.

Zahn, K., Méndez-Alcaraz, J. M., & Maret, G., 1997. Hydrodynamic Interactions May Enhance the Self-Diffusion of Colloidal Particles, *Physical Review Letters*, **79**(1), 175–178.

Zieg, M. J. & Marsh, B. D., 2012. Multiple Reinjections and Crystal-mush Compaction in the Beacon Sill, McMurdo Dry Valleys, Antarctica, *Journal of Petrology*, **53**(12), 2567–2591.

APPENDIX A: FURTHER MODEL DETAILS

A1 Constitutive relations

Keller & Suckale (2019) derived constitutive relations to describe the fluxes, transfers and external sources, based on the thermodynamic constraints of energy conservation and non-negative entropy production. These constitutive relations are substituted into the governing equations of mass and momentum balance. Three assumptions direct the choice of constitutive relations to be (a) decoupled, (b) linear and (c) isotropic. In principle, these assumptions can be relaxed to admit more complex constitutive relations, however in practice this may demand too many unresolved constraints. In the mechanical system with incompressible phases and no inertial effects, entropy is produced by dissipative mass and momentum flux, irreversible mass and momentum transfer, and from interactions of the system with the external momentum source of gravity. Here we simply state the constitutive relations; for the full derivation please refer to Keller & Suckale (2019) Section 4.

A1.1 Transfers

Transfers describe the change in mass or momentum due to an imbalances among the phases, which can be understood as a measure of phase disequilibrium. The system addresses these imbalances by transferring mass or momentum from one phase to another. To describe transfers, we necessarily need to describe the imbalance among phase pairs in the system. Taking differences between all possible phase pairs in an n-phase system will quickly become untenable, hence we introduce a common reference state, from which deviations will drive transfers. For a property $\mathbf{a}$ (representing pressure, velocity, density, etc.), the reference state is $\mathbf{a}^* = \sum_i \omega_a^i \mathbf{a}^i$, where ω_a^i represents how fast phase i can reach the equilibrated state and will be defined below. Transfers are driven by the deviation from the reference state $\Delta\mathbf{a}^{i*} = \mathbf{a}^i - \mathbf{a}^*$. If deviations are zero, the reference state $\mathbf{a}^*$ can be thought of as the equilibrated state of property $\mathbf{a}$.

For the mechanical system, we need the constitutive relations that describe volume transfer Γ_ϕ^i and momentum transfer $\mathbf{\Gamma}_v^i$, derived as

$$\Gamma_\phi^i = \frac{\partial \phi^i}{\partial t} = C_\phi^i \Delta P^{i*} - \mathbf{v}^* \cdot \nabla \phi^i \,, \tag{A.1a}$$

$$\mathbf{\Gamma}_v^i = C_v^i \Delta \mathbf{v}^{i*} - P^* \nabla \phi^i \,. \tag{A.1b}$$

Volume transfer occurs due to deviation of pressure from the reference state ΔP^{i*}, modulated by the volume transfer coefficient C_ϕ^i, and the gradient of phase fraction moving with the reference velocity. Momentum transfer occurs due to the deviation of velocity from the reference state $\Delta \mathbf{v}^{i*}$, modulated by the momentum transfer coefficient C_v^i, and the gradient of phase fraction driven

by the reference pressure field. The first two terms of each transfer relation reveal the conjugate relationships between volume and pressure, and between momentum and velocity.

The transfer coefficients C_ϕ^i, C_v^i are non-negative scalars that describe the relative transfer rates for each phase. Larger C_ϕ^i, C_v^i imply faster equilibration of phase i, therefore it follows that the reference states should be weighted by C_ϕ^i, C_v^i. Finally, to ensure that transfers sum to zero across all phases, we choose the reference state to be the weighted sum of phase states with weights given by the normalised sum of transfer coefficients. Following this logic, the reference pressure and velocity states are

$$P^* = \sum_i \omega^i_{C_\phi} P^i = \sum_i \frac{C_\phi^i}{\sum_k C_\phi^k} P^i \,, \tag{A.2a}$$

$$\mathbf{v}^* = \sum_i \omega^i_{C_v} \mathbf{v}^i = \sum_i \frac{C_v^i}{\sum_k C_v^k} \mathbf{v}^i \,. \tag{A.2b}$$

A1.2 Fluxes

Fluxes describe the transport of mass and momentum due to spatial gradients within each phase. For the mechanical system, volume and momentum flux are driven by the forcing gradients of pressure and velocity respectively,

$$\mathbf{q}_\phi^i = -K_\phi^i \Delta(\nabla P)^{i*} + \phi^i \mathbf{v}^i \,, \tag{A.3a}$$

$$\underline{\mathbf{q}}_v^i = -K_v^i \underline{\mathbf{D}}^i + \phi^i P^i \underline{\mathbf{I}} \,. \tag{A.3b}$$

The first term of each flux is the diffusive part and the second term the advective part. The volume flux is driven by the deviation of pressure gradient from the reference state $\Delta(\nabla P)^{i*} = (\nabla P)^i - (\nabla P)*$ and the advected volume flux $\phi^i \mathbf{v}^i$. The rate of the diffusive process is controlled by the volume flux coefficient K_ϕ^i. Momentum flux is driven by the deviatoric strain $\underline{\mathbf{D}}^i$, modulated by the momentum flux coefficient K_v^i, and phase compaction. Implicit in the momentum flux is that the intrinsic bulk viscosity of compressible phases is negligible compared to phase compaction driven by $\phi^i P^i$ in causing volumetric deformation.

The flux coefficients K_ϕ^i, K_v^i are non-negative scalars that describe the relative fluxes. so that the reference pressure gradient is the weighted sum of phase-wise pressure gradients,

$$(\nabla P)^* = \sum_i \omega^i_{K_\phi^i} (\nabla P)^i = \sum_i \frac{K_\phi^i}{\sum_k K_\phi^k} (\nabla P)^i \,. \tag{A.4}$$

A1.3 Sources

There are no external sources for mass, while gravitational acceleration $\mathbf{g}$ provides an external source for momentum,

$$\mathbf{Q}_v^i = -\phi^i \rho^i \mathbf{g} \,. \tag{A.5}$$

A2 Flux and transfer coefficient closures

We require material closures to describe the flux and transfer coefficients $K_v^i, K_\phi^i, C_v^i, C_\phi^i$. Since local-scale diffusive transport facilitates transfers and fluxes, the model uses closures that depend on phase fraction, the diffusive properties of pure-phase materials, k_a^i, and the local-scale phase topology. The pure-phase momentum diffusion parameter is the dynamic viscosity η_0^i, whose value can be obtained from experiments. The pure-phase volume diffusion parameter is motivated by the hindered Stokes settling speed to be ${d_0^i}^2/\eta_0^i$, which implies that volume diffusion is influenced by the compliance of a liquid of viscosity η_0^i moving around an obstacle of size d_0^i. The local-scale phase topology is parameterised in terms of permission functions $\theta_\phi^i, \theta_v^i$ (defined below) to regulate volume and momentum diffusion based on the connectivity of phase i in the aggregate. Combining pure-phase diffusion parameters and permission functions, the flux and transfer coefficients are

$$K_v^i = \phi^i k_v^i \theta_v^i = \phi^i \eta^i \theta_v^i \,, \tag{A.6a}$$

$$K_\phi^i = \phi^i k_\phi^i \theta_\phi^i = \frac{\phi^i {d^i}^2 \theta_\phi^i}{\eta^i} \,, \tag{A.6b}$$

$$C_v^i = \frac{\phi^i(1-\phi^i) k_v^i \theta_v^i}{{d^i}^2} = \frac{\phi^i(1-\phi^i)\eta^i \theta_v^i}{{d^i}^2} \,, \tag{A.6c}$$

$$C_\phi^i = \frac{\phi^i(1-\phi^i) k_\phi^i \theta_\phi^i}{{d^i}^2} = \frac{\phi^i(1-\phi^i)\theta_\phi^i}{\eta^i} \,. \tag{A.6d}$$

Transfer coefficients are related to flux coefficients by a factor $(1-\phi^i)/{d_0^i}^2$, reflecting that transfers go to zero in the pure-phase limits, and that transfers take place over the length scale of the grain size.

The permission functions θ_a^i are geometric averages of pure-phase diffusive properties weighted by a measure of connectivity within and between phases,

$$\theta_a^i = \prod_k {M_a^{ik}}^{X_\phi^{ik}} \,, \tag{A.7}$$

where $M_a^{ik} = k_a^k / k_a^i$ are the pure-phase diffusive parameter contrasts and X_ϕ^{ik} are weights (range 0 to 1) that describe how local phase connectivity depends on phase fraction, encapsulating information on phase size, shape, compositions, surface energies, and other factors that affect how one phase wets another,

$$X_\phi^{ik} = \left(\sum_k A^{ik} S_\phi^{ik} \right) \phi^i + \left(1 - \sum_k A^{ik} S_\phi^{ik} \right) S_\phi^{ik} \,, \tag{A.8}$$

where S_ϕ^{ik} are smooth step functions in phase space,

$$S_\phi^{ik} = \frac{\left(\frac{\phi^k}{B^{ik}}\right)^{1/C^{ik}}}{\sum_j \left(\frac{\phi^j}{B^{ij}}\right)^{1/C^{ij}}} \,. \tag{A.9}$$

A^{ik}, B^{ik}, C^{ik} are empirical fitting parameters to describe the transition of phase connectivity between pure-phase limits with the slope $0 \le A^{ik} \le 1$ and a smooth step function centreed at critical phase fraction $0 \le B^{ik} \le 1$ with ($\sum_k B^{ik} = 1$), which can be thought of as the disaggregation or percolation threshold, and weights $C^{ik} \ge 0$ setting the relative step width. Ideally, these fitting parameters would be calibrated using existing data.

A2.1 Calibrating transport coefficients for the two-phase system

We model the two-phase igneous system containing solids and liquids after a mixture of olivine crystals and basalt liquid. Keller & Suckale (2019) calibrated the fitting parameters A, B, C of the permission weights using experimental and theoretical constraints on the solid-rich and liquid-rich end members, which we continue to use for this two-phase system. The momentum flux coefficient K_v^i controls the rate at which stress is transmitted through the phase, and can thus be calibrated using experimental data at solid-rich end from Hirth & Kohlstedt (2003), and effective viscosity models in a dilute suspension at the liquid-rich end (Roscoe, 1952). The volume flux coefficient K_ϕ^i is calibrated using hindered-Stokes settling theory and sedimentation experiments on the velocity correlation

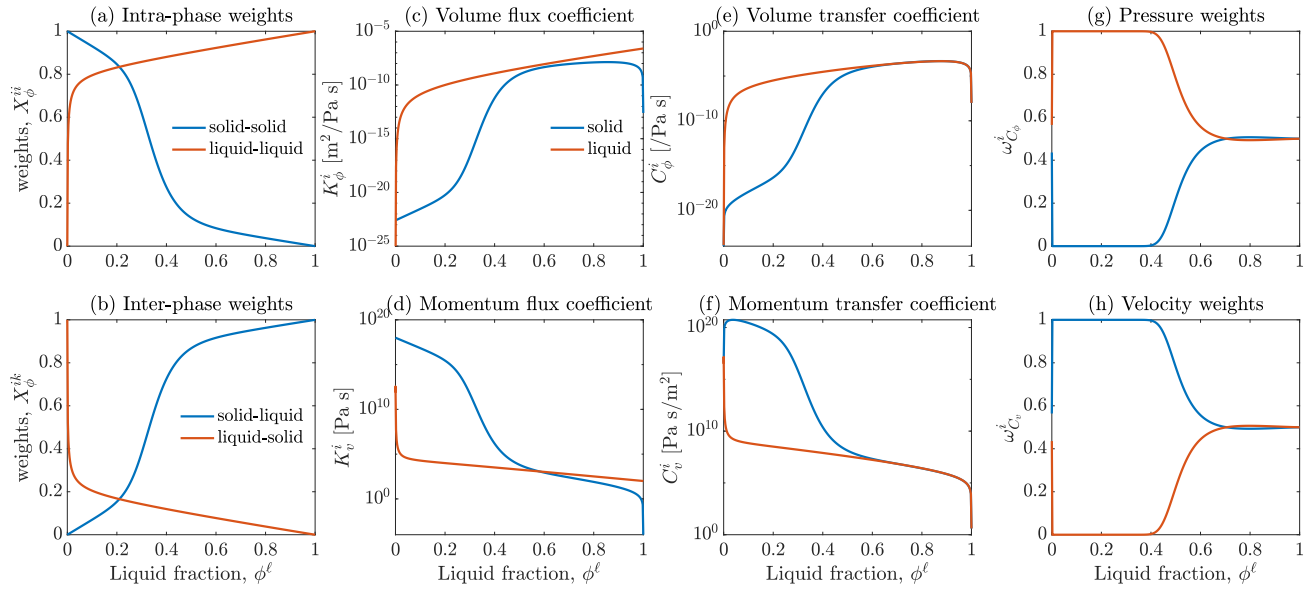

Figure A1. (a,b) Permission weights, (c,d) flux coefficients, (e,f) transfer coefficients, (g) pressure weights and (h) velocity weights as functions of liquid fraction ϕ^ℓ in the two-phase solid-liquid system, calibrated to an olivine-basalt mixture.

Table A1. Properties for material closures.

Property	Symbol	Solid	Liquid
Pure-phase properties			
Viscosity [Pa s]	η^i_0	10^{18}	10^2
Granular scale [mm]	d^i_0	5	5
Calibrated permission weight parameters*			
Slopes	A	[0.6945, 0.1832]	[0.5360, 0.1834]
Thresholds	B	[0.6906, 0.3094]	[0.9993, 0.0007]
Weights (step width)	C	[0.6889, 0.1750]	[0.8154, 1.5642]

* Permission weight fitting parameters A, B, C are given as they relate to [solid,liquid], e.g. the order of slope values is $[A^{ss}, A^{s\ell}]$, $[A^{\ell s}, A^{\ell\ell}]$.

among solid grains (Segrè et al., 2001). Rearranging the equations to yield (5) shows that the combination ϕ^{i^2}/C^i_v corresponds to the Darcy percolation coefficient in the compaction equations (ratio of matrix permeability to liquid viscosity), thus C^i_v is calibrated using the Kozeny-Carman permeability relationship and the viscosity models at the solid-rich end. The combination ϕ^{i^2}/C^i_ϕ is analogous to the compaction viscosity in the compaction equations and is calibrated using theoretical work of Takei & Holtzman (2009) and Rudge (2018). Notably, this calibration procedure showed that one set of connectivity parameters can reasonably match the constraints on all four coefficients, reflecting the common physical basis of connectivity that controls the flux and transfer of mass and momentum.

We apply the same calibrations here (Table A1, Figure A1). The permission weights (panels a,b) are a representation of phase connectivity. With increasing liquid fraction, solid-solid connectivity decreases and is compensated by greater connectivity of the solid to the liquid phase. This change is greatest at the disaggregation threshold where the liquid fraction is 0.3094. Beyond the disaggregation threshold, the solid grains are well connected to the liquid. In contrast, the liquid phase reaches a high level of connectivity with itself from a very low liquid fraction, which we call the percolation threshold, here set as 0.0007. This reflects that the liquid wets the solid much more easily, and is able to reach high levels of connectivity even at low liquid fraction.

We apply the permission weights to the flux (panels c,d) and transfer (panels e,f) coefficients. The large connectivity decrease across the disaggregation threshold is apparent in the solid transport coefficients, while the connectivity increase at the percolation threshold is seen in the liquid transport coefficients. The transfer coefficients acts as weights for the reference pressure and velocity fields (panels g,h). At low liquid fraction, the liquid volume transfer coefficient is much greater than the solid, thus the liquid phase dominates the pressure weights. The solid momentum transfer coefficient is orders of magnitude greater than the liquid, thus the solid phase dominates the velocity weights. As liquid fraction increases, transfer coefficients of both phases approach each other, until both phases contribute to the reference pressure and velocity equally.

APPENDIX B: NUMERICAL STABILISATIONS: LIMITERS ON PERMISSION FUNCTIONS AND COEFFICIENTS

Due to the large viscosity contrast between the solid and liquid phase, we employ two limiters to stabilise the numerical solutions: `thtlim` to limit contrasts within permission functions within each phase across the domain, and `cfflim` to limit contrasts between flux and transfer coefficients between phases. Permission functions $\theta^i_v, \theta^i_\phi$ describe the local-scale phase topology, and are combined with pure-phase diffusive properties and phase fraction to calculate the flux and transfer coefficients (Appendix A2). For each phase, permission functions can take on vastly different values across the domain. After calculating these permission functions, the code calculates a characteristic scale for each phase by taking its geometric

mean over the domain, then adjusts the permission functions by

$$\theta^i_{v,\mathrm{st}} = \left[\frac{1}{\theta^i_v} + \frac{\langle\theta^i_v\rangle}{\texttt{thtlim}^{1/2}}\right]^{-1} + \frac{\langle\theta^i_v\rangle}{\texttt{thtlim}^{1/2}}\,, \tag{B.1a}$$

$$\theta^i_{\phi,\mathrm{st}} = \left[\frac{1}{\theta^i_\phi} + \frac{\langle\theta^i_\phi\rangle}{\texttt{thtlim}^{1/2}}\right]^{-1} + \frac{\langle\theta^i_\phi\rangle}{\texttt{thtlim}^{1/2}}\,, \tag{B.1b}$$

where $\theta^i_v, \theta^i_\phi$ are the original, unstabilised permission functions, $\langle\theta^i_v\rangle, \langle\theta^i_\phi\rangle$ are the characteristic scales from geometric averaging over the domain, and $\theta^i_{v,\mathrm{st}}, \theta^i_{\phi,\mathrm{st}}$ are the numerically stabilised permission functions. If `thtlim` is set to be much larger than the average permissions across the domain, then the limiter will have no effect and the stabilised values will be identical to the original permission functions.

The stabilised permission functions are then used to calculate the flux and transfer coefficients, on which the second limiter `cfflim` applies. The code first calculates a characteristic scale for the coefficients, again using the geometric mean. To control the coefficient contrast between phases, the code updates the coefficients using this characteristic scale and `cfflim`,

$$K^i_{v,\mathrm{st}} = K^i_v + \frac{\max_j\langle K^j_v\rangle}{\texttt{cfflim}}\,, \tag{B.2a}$$

$$K^i_{\phi,\mathrm{st}} = K^i_\phi + \frac{\max_j\langle K^j_\phi\rangle}{\texttt{cfflim}}\,, \tag{B.2b}$$

$$C^i_{v,\mathrm{st}} = \left[\frac{1}{C^i_v} + \frac{\texttt{cfflim}}{\min_j\langle C^j_v\rangle}\right]^{-1}\,, \tag{B.2c}$$

$$C^i_{\phi,\mathrm{st}} = \left[\frac{1}{C^i_\phi} + \frac{\texttt{cfflim}}{\min_j\langle C^j_\phi\rangle}\right]^{-1}\,. \tag{B.2d}$$

A similar notation to the permission functions applies, where the subscript st denotes the numerically stabilised coefficient. Among the phases, the maximum flux coefficient scale is chosen and normalised by `cfflim`, then added to all the flux coefficients. This raises smaller flux coefficients to be within `cfflim` of the maximum while leaving maximum coefficient unchanged, effectively increasing the rate of the slowest process in the system to be within `cfflim` of the fastest process. The reciprocal approach is applied to transfer coefficients using the minimum, such that the larger transfer coefficients are reduced to be within `cfflim` of the minimum transfer coefficients. The reciprocal approach prevents overestimation of the compaction pressures and segregation velocities of the more mobile phase, since the transfer coefficients appear in the denominator of governing equations (5). As with the first limiter, selecting a large value for `cfflim` will nullify its effect.

APPENDIX C: MODEL VERIFICATION USING MANUFACTURED SOLUTIONS

To verify the numerical model, we employ the Method of Manufactured Solutions (e.g. Salari & Knupp, 2000). This verification procedure substitutes an analytical expression (the "manufactured solution") for the solution variables $y^i(x,z,t) = [u^i, w^i, p^i, \phi^i](x,z,t)$ into the governing equations. Since the manufactured solution is not the exact solution to the governing equations, there will be a residual term, which can also be evaluated analytically. This analytical residual term is written into the code as an additional term in the governing equations. The numerical model is then solved together with the analytical residual term, and the resulting numerical solution is compared with the input manufactured solution.

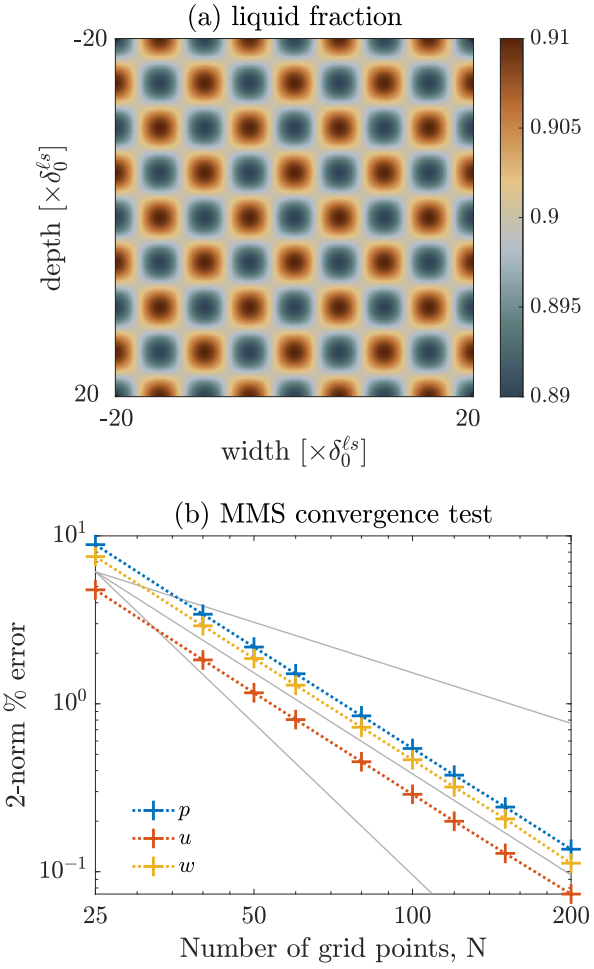

Figure A2. Model verification by the Method of Manufactured Solutions. (a) Liquid fraction distribution applied to the problem for the suspension flow regime. The same sinusoidal pattern is used for the pressure and velocity fields, with different amplitudes. (b) Convergence plot of 2-norm percentage errors comparing the numerical and analytical solutions for pressure p, horizontal velocity u and vertical velocity w at different number of grid points along one direction N. The gray lines are, in increasing order of steepness, the reference lines for 1st, 2nd and 3rd order convergence.

This manufactured solution should be continuous, differentiable to the order required by the problem, and similar in magnitude and spatial pattern to an expected solution to the governing equations, so that the residual term does not dominate the resulting numerical solution. For the system of equations in this study, we chose a sinusoidal variation for the analytical solution fields with periodic boundary conditions (Figure A2a). We show results from the suspension ($\phi^\ell = 0.90$) flow regime and use the scaling analysis to estimate the appropriate amplitude of the sinusoidal variations, set as [10^{-4} m/s, 10^{-4} m/s, 10^{0} Pa, 10^{-2}], as they appear in the vector y^i. These solution fields are then substituted into the governing equations. To solve the numerical model, we follow the same procedure as outlined in Section 3, using the initial condition of phase fractions to solve for consistent velocity-pressure fields, but now with the additional analytical residual term. Both `thtlim` and `cfflim` were set to large values of 10^{16} to render their effect

Table A2. Metrics for numerical model scalability by testing models at different grid resolution.

Grid size	Increase in # cells	β	# Iterations	Solution time [min]	Time per iteration [ms]
$\phi^\ell = 0.90$, fixed β					
50×50	1	0.5	1900	0.24	7.6
100×100	4	0.5	3900	0.50	7.7
200×200	16	0.5	9400	2.63	16.8
400×400	64	0.5	17900	17.10	57.3
$\phi^\ell = 0.90$, variable β					
50×50	1	0.5	1900	0.24	7.6
100×100	4	0.7	2400	0.37	9.3
200×200	16	0.8	3900	1.24	19.1
400×400	64	0.9	3600	3.60	60.0
$\phi^\ell = 0.05$, fixed β					
200×200	1	0.4	10900	3.07	16.7
400×400	4	0.4	17000	16.35	57.7
$\phi^\ell = 0.05$, variable β					
200×200	1	0.4	10900	3.07	16.7
400×400	4	0.6	11400	10.83	57

negligible. We then solve the numerical model at different grid resolutions of a specified domain size of $40\delta_0^{\ell s}$. This domain size is large enough for both phase segregation and mixture flow to be appreciable, while still small enough to test a sufficient variety of grid numbers.

The resulting two-norm errors between the numerical and analytical manufactured solutions for velocity and pressure fields are shown in Figure A2b. The solutions converge with second-order accuracy as expected for the staggered-grid central differencing scheme used to discretise the governing equations.

APPENDIX D: SCALABILITY OF THE NUMERICAL MODEL

We test the numerical model scalability by running simulations at different grid resolutions. We select two phase fractions to represent the suspension and porous flow regimes, while imposing random initial perturbations of amplitude 0.01 and periodic boundary conditions on a domain of size $40\delta_0^{\ell s}$ (similar to the setup for Section 4.3). We set `thtlim` and `cfflim` to 10^{16}. The iterative step size control α was set to 0.95. We run the simulation for one time step, and terminate iterations once the absolute residual to the governing equations goes below 10^{-5}. The simulations were run on a 2020 8-core Macbook Air with an Apple M1 chip and 16GB memory.

Table A2 reports the resulting number of iterations and time to solution per grid resolution. For each phase proportion, we run two sets of simulations: one with fixed β for iteration convergence, another with the maximum β permitted at a given grid resolution, where β is the damping parameter in the iterative scheme. With fixed β, the pseudo-transient iterative solver demonstrates a favourable scaling: as the resolution quadruples, the number of iterations needed increases by less than four times, as discussed in Section 3.3. However, for finer grids, each iteration requires more time because of the much larger number of matrix multiplication operations to calculate the constitutive relations, hence the time to solution increases by greater than four times. On the other hand, allowing β to vary makes better use of the pseudo-transient method. In this case, we first run the simulation with large β. If the iterations diverge, we reduce β by 0.1 and rerun the solution, repeating this process until we find a β with converging iterations. We find that although the time per iteration is the same at the same grid resolution, finer grids permit larger β, enabling convergence with fewer iterations and overall shorter time compared to the simulations with fixed β.